Gradient plasticity with interfacial effects and experimental confirmation through nano-indentation

Aifantis, Katerina Elias

RIJKSUNIVERSITEIT GRONINGEN

GRADIENT PLASTICITY WITH INTERFACIAL EFFECTS AND EXPERIMENTAL CONFIRMATION THROUGH NANO-INDENTATION

PROEFSCHRIFT

ter verkrijging van het doctoraat in de
Wiskunde en Natuurwetenschappen
aan de Rijksuniversiteit Groningen
op gezag van de
Rector Magnificus, dr. F. Zwarts,
in het openbaar te verdedigen op
maandag 18 april 2005
om 14.45 uur

door

Katerina Elias Aifantis

geboren op 1 mei 1983
te
Minneapolis, MN, USA

PROMOTORES : PROF. DR. J.T.M. DE HOSSON
PROF. DR. J.R. WILLIS

Beoordelingscommissie : Prof.dr. H.A. De Raedt
Prof.dr. P. Rudolf
Prof.dr. L. Kok

The work described in this thesis has been made possible by financial support from the US National Science Foundation, under its Graduate Research Fellowship Program.

CONTENTS

CHAPTER 1

OBJECTIVES

The present thesis proposes a new method for assessing the influence of microstructural scale on the yield strength of composites and polycrystals, by allowing certain features of the deformation field to vary discontinuously across pre-existing internal surfaces, such as interfaces in metal-metal composites and grain or interphase boundaries in polycrystals. The jumps associated with such discontinuities are accommodated by an excess interfacial energy-like term (interfacial penalty), which is introduced to model the micro/nano scopic deformation mechanisms that take place at these surfaces of discontinuity, for the plastic strain gradient.

In particular, the material response is characterized through strain-gradient plasticity and the "interfacial energy", which depends solely on the plastic strain at the interface, is admitted in the overall energy functional of the system. The physical motivation for this is that interfaces present an obstruction to dislocation motion, and hence plastic flow. As a result, during plastic deformation dislocation pileups occur at internal surfaces. These pileups correspond to gradients in the plastic strain and, as a result, the strain-gradient, and corresponding higher-order traction, are taken to suffer a jump across interfaces. It is important to emphasize the need to admit strain-gradient plasticity as the material response of the system since it is the gradient of the

plastic strain (which is not accounted for in conventional plasticity) that permits for the jump condition in higher-order stress, and allows interfaces to have their own yield behavior and be treated as surfaces of discontinuity. Although discontinuities have been a subject of substantial research activity in mechanics [1], interfaces have never been modeled through this type of consideration. Two classical examples that have been studied extensively within the theory of elasticity are dislocations and cracks, where the displacement field is assumed to be discontinuous in a mathematical sense. This hypothesis led to the development of dislocation and fracture mechanics. Within the theory of plasticity Luders bands and shear bands are also often considered as surfaces across which the plastic strain is discontinuous. In the present work, the plastic strain will be assumed to be continuous across the interface but the plastic strain gradient will be allowed to suffer a discontinuity there. This can be done by generalizing classical plasticity theory to allow for the effect of plastic strain gradients to enter into the constitutive equations. This generalization is commonly known as gradient plasticity. Gradient plasticity is therefore intended to make allowance, at least qualitatively, for the influence on hardening of the long-range stresses produced by "geometrically-necessary" as opposed to "statistically stored" lattice dislocations.

Strain-gradient theories gained considerable attention since the first gradient plasticity theory developed by Aifantis in 1984 [2] was able to resolve certain deficiencies that classical plasticity could not describe, such as obtaining widths and spacings of shear bands and dispensing with the mesh-dependence of finite element calculations in the material softening regime. Since then, strain-gradient plasticity has been used extensively to examine the development and persistence of dislocation patterns, and the occurrence of size effects (e.g. in nano-identation), in addition to the above phenomena. Among the gradient theories that have been developed during the past decade one distinguishes the works of Fleck-Hutchinson and co-workers [3,4] who developed a Cosserat type

strain-gradient plasticity with asymmetric stress and applied it for interpreting plasticity at the micron-scale, including size-effects. More recently, Fleck and Hutchinson [5] revised their previous theory to remove certain deficiencies related to the elasto-plastic coupling within their higher order gradient setting and incorporated in it the advantages of the Aifantis formulation [2,6] in order to render their theory more efficient computationally. An even more appealing formulation of a deformation type gradient plasticity theory was recently provided by Fleck and Willis [7] who endowed it with appropriate boundary and continuity (across interfaces) conditions and applied it to derive effective properties of composites.

Several other significant contributions have been made including, among others, those by Gao and co-workers [8,9], Gurtin and co-workers [10,11] and Gudmundson [12]. With the exception of the latter work, however, no theory has been developed to consider the occurrence of jump conditions across interfaces. But even this latter work does not provide a detailed analysis of the microscopic deformation mechanisms that take place along an interface, or their implications on the form of the interfacial energy assumed. Moreover, it does not consider the effect of interfaces in the overall mechanical response; for example, by deducing macroscopic or effective stress-strain relationships. In fact, no theory, which considers interfaces, from those developed through various approaches (such as continuum elasticity and atomistics [13,14,15,16,17,18] and gradient plasticity [6,12]) has been successfully applied to model the effect of interfaces in the overall stress-strain response during plastic deformation, even though interfacial effects are of great significance and interest, especially in the emerging fields of nanomechanics and nanotechnology, in which the volume fraction of the grain boundary to grain interior is relatively high.

All gradient theories have associated with them a characteristic (internal) length, and the influence of the gradient term becomes apparent as soon as some dimension of the specimen is reduced to some small multiple of this

characteristic length. Mathematically speaking, the internal length relates to the gradient coefficient (characterizing the corresponding gradient term) and its presence is required for dimensional consistency; it is desirable, moreover, to keep it fixed in fitting data from different experimental setups. This is to be expected when the internal length is the same for different experimental configurations and may be viewed as a material property rather than a parameter depending on the geometry of deformation.

An additional, feature which has so far not yielded to precise physical interpretation is associated with the fact that introduction of the gradient term requires the introduction of an additional boundary condition, together with an additional jump or continuity condition across any internal surface. The mathematical structure shows what quantity needs to be specified but provision of the actual value can only follow from a clear recognition of the physics that the strain-gradient theory is supposed to represent. It can therefore be seen that even though extensive research is being performed that focuses on developing or choosing an effective (yet simple) theory, which will be able to model a large amount of tests pertaining to different experimental configurations, there still remain several open issues related to the physical interpretation of the internal length and the appropriate boundary conditions associated with the gradient terms. It, thus, follows that existing strain-gradient theories, which model reasonably well experimental data, may not be adopted universally unless the respective internal length parameters are clearly interpreted in terms of the underlying plastic flow mechanisms and related measurements.

Qualitatively, several theories may show the right trend, but differences of detail (obtained by fixing parameters relative to one experimental setup and then predicting outcomes for different experiments) can provide evidence for one theory relative to another, but will not definitively identify one theory as "correct". Another approach is to compare predictions made by use of a strain-gradient theory with corresponding predictions obtained from a simulation

which employs discrete dislocations. A drawback here is that the discrete dislocation simulation inevitably employs an idealized version of the underlying physics, in particular because one may be obliged to treat a 3D dislocation problem in a 2D approximation. It is also true that more than one strain-gradient theory has shown good compatibility with discrete dislocation simulations [19,20,21,22,23,24].

Another method that can be used to check the validity of these gradient theories is to compare each other in relation to benchmark problems that can be unambiguously defined. For example, the formation and evolution of "shear bands" in the post-localization deformation regime, the development of "boundary layers" during the constrained plastic flow between parallel plates, and the interpretation of size effects in polycrystals and composites may be considered as such benchmark cases.

A particular class of problems that can be used for calibrating strain-gradient theories is that involving interfaces. The relevant question then is to decide which quantities may be assumed continuous across the interface and which cannot. In addition to the obvious requirement of balancing forces across interfaces, one should decide on the amount of detail and the determination of the spatial characteristics desired by the analysis. If it is desired, for example, to obtain an estimate for the "thickness" of the interfacial region, the strain-gradients should be taken continuous across internal surfaces, and an appropriate constitutive equation for the local stress should be assumed there. This is the approach adopted, for example, by Aifantis [25] who described a method for treating interfaces within the structure of his earlier developed theory of gradient plasticity [2,6]. If, however, one is concerned with many interfaces, as in the case of a polycrystal or a metal-metal composite, such a detailed analysis is not necessary for characterizing the overall material response. In this case the interfaces may be treated as surfaces of discontinuity, for the plastic strain gradient, and no detailed constitutive assumption for the local stress in terms of

atomistic considerations is explicitly needed. It is required, however, to envision the relevant plastic flow mechanism in order to deduce which quantities may be viewed as varying continuously across the interface, which may not, and what extra assumptions for the interfacial energy should be introduced in order to accommodate the aforementioned discontinuities. This approach is introduced in the present thesis.

The gradient theory employed is a re-formulation of a deformation version of gradient plasticity, which was recently advanced by Fleck and Willis [7]. These authors considered interfaces implicitly and adopted methods [26,27,28,29] for calculating the effective response of nonlinear composites whose constituents conformed to a deformation-theory version of strain-gradient plasticity, closely related to the strain-gradient theory advanced in [5]. A similar study had been performed earlier in [30,31] recognizing that strain-gradient plasticity also produced a scale effect on the yield behavior of a composite or a polycrystal: the macroscopic stress and strain fields could vary smoothly and yet be associated with intense microscopic fluctuations whose exact form would depend on the scale of the microstructure in comparison with the intrinsic length scale associated with the gradient theory.

Fleck and Willis [7] also demonstrated the occurrence of a scale effect of the microstructure on the effective flow stress of a composite which, for very fine microstructure however, had a definite upper limit equal to the "Voigt upper bound" of classical elasticity. This is because plastic strain gradients were obliged to tend to zero as the scale of the microstructure reduced, giving (in the limit) the Voigt "uniform plastic strain" approximation. In the chapters to follow it is shown that this rather undesirable feature is not intrinsic to the specific gradient theory, but resulted from the "natural" mathematical assumption that both the plastic strain and plastic strain gradient were continuous across interfaces (and thus interfacial effects were not explicitly considered). This need not be so, however, if one considers that a dislocation crossing an interface will leave a

ledge on the interface and therefore add to its energy. Qualitatively, this relates to the admission of dislocation pileups near boundaries leading to the classical Hall-Petch mechanism [32,33] for grain-refinement strengthening (dislocation pileups correspond to local gradients in plastic strain). As it will be shown below, the assumption of continuity of plastic strain across interfaces is retained but the build-up (accumulation) of plastic strain at internal surfaces is penalized through the introduction of an "interfacial energy" term, which depends on the plastic strain there. In the context of strain-gradient theory, it induces a relation between the jump in higher-order traction and the interfacial plastic strain, and hence allows for the development of an "interfacial" yield-like condition.

It is appropriate here to emphasize that dislocation pileups and dislocation transference across interfaces have been observed experimentally with the aid of conventional and in-situ transmission electron microscopy (TEM) nano-indentation. It has been observed, for example, that plastic deformation is transmitted to grains adjacent to the indented grain through dislocation motion across grain boundaries [34]. Similar pre-dated observations have led the mechanics community to treat interfaces solely as obstacles to plastic flow, since they emit dislocations to adjacent grains, which have not yielded, only once the force exerted on them (by the leading dislocations) reaches a critical value. Alternatively, macroscopic yielding can be induced when the stress concentration that is produced by dislocation pile-ups is sufficient to activate slip in undeformed grains [35]. In this connection, it should be noted that consideration of interfaces through continuum lattice considerations provides corresponding expressions for the stress and displacement fields which, in turn, allow for the determination of the energy difference required to move a dislocation as a function of distance from the interface; the force exerted on dislocations across interfaces; and the interfacial energy as a function of misfit. It is more common, however, to express the interfacial energy as a function of interatomic potentials and distances; this is accomplished by examination of

interatomic interactions across interfaces (such as bond strength), within an atomistic approach [13a]. Finally, it should be noted that internal surfaces have been extensively modeled through materials science arguments, which consider interfaces within the framework of thermodynamics and hence an interfacial energy, which accounts for the excess free energy that arises from the presence of interfacial material is deduced. According to this approach internal surfaces are taken to be arrays of dislocations, i.e. screw or edge in single phase media, and misfit in two phase; while the interfacial energy is a function of internal surface orientation. It should be emphasized that in the present study the "interfacial energy" is viewed in a different manner since it is induced by plastic deformation and is therefore taken to be a function of the plastic strain on the interfaces. This form might be rather simple, but for the purposes of the proposed formulation it is perhaps the most efficient since it allows internal surfaces to follow their own yield behavior and the plastic strain gradient to suffer a jump across them. This jump depends on the constitutive response of the system, as well as on the ratio of the internal length over the specimen size; hence size effects not limited by an upper bound, as in [7], are obtained.

The subsequent development is organized as follows: Chapter 2 elaborates on the underlying physics on which the gradient formulation that will follow is based. A physical overview is given for the types of interfaces that are common in metallic systems, such as grain boundaries (interfaces between same phases) and interphase boundaries (interfaces between different phases). Since grain boundaries are simpler, much more is understood about their structure and how they interact with dislocations; therefore a brief description on the topic is developed, in particular on the formation of grain boundary ledges which is the main motivation for the present work. Experimental evidence is also provided, concerning interface-dislocation interactions and the existence of dislocation pileups.

In Chapter 3 the "interfacial energy" penalty is introduced in the overall energy functional of the domain under consideration; first within the framework of classical plasticity (for comparison purposes), and then for a composite whose microstructure conforms to gradient plasticity. After prescribing the displacement on the outer boundary and allowing for continuous total and plastic strains across interfaces, the overall energy functional is minimized, providing thus the equilibrium, boundary and across internal surfaces conditions. The presence of the "interfacial energy" term induces a jump in the higher order traction. In the sequel, homogenization methods, which account for the presence of internal boundaries, are formulated and hence the effective response for very fine microstructure is deduced. In particular, a refined upper bounding technique is developed based on the "linear comparison method", first introduced in the simpler context of physically-nonlinear elasticity, or classical deformation-theory plasticity [29]. This method allows for the effective response of nonlinear media to be bounded, by comparison with a medium with the same microgeometry, but linear response; it is therefore required to first obtain an exact solution or approximation for the linear medium. It should be noted that the upper bounds obtained in this chapter are scale independent, due to the presence the "interfacial energy" term.

In Chapter 4 the new features of the previously developed formulation are illustrated by considering one dimensional, heterogeneous and homogeneous, examples in which interfaces are distributed periodically. These examples are chosen such that the constitutive differential equations developed in Chapter 3 can be solved exactly. The response for the interfaces is first taken to be linear, but then a more physical nonlinear model, corresponding to the formation of dislocation pileups across interfaces, is developed. The distinctive feature of this model is that it allows for the determination of the stress required in order for the plastic strain to differ from zero on the interface; in the present study this stress is termed "interfacial yield" stress. In particular for the heterogeneous media, the

simple form assumed for the gradient dependent plastic potential allows analytical solutions to be obtained for the average stress-strain response. For the homogeneous material, however, this plastic potential, which corresponds to that employed in [7] is highly nonlinear and therefore only numerical solutions can be produced. An additional highly nonlinear potential is introduced for comparison purposes. All examples exhibit significant scale effects, which indicate a Hall-Petch type of behavior since the response of the material stiffens as its size is reduced.

If one considers slightly more complicated problems, such as a random interface distribution, exact solutions cannot be obtained, and that is where the homogenization techniques of Chapter 3 come into play. In Chapter 5, therefore, the linear comparison method is illustrated for the aforementioned highly nonlinear homogenous media; it is shown that the approximate solutions that result from this technique coincide with the exact solutions that were obtained in Chapter 4. This method therefore is proven to be rather accurate, at least for the one-dimensional examples at hand, and is applied to find the response for the same highly nonlinear material, but for the case where interfaces are distributed randomly, according to a Poisson process. For this random case, an exact solution does not exist even for the linear comparison medium, whose solution is required in order to perform the comparison method. Therefore, two- and three-point statistics are used to obtain lower and upper bounds, respectively, for the nonlinear material response, which are then used to derive approximations for the stress-mean plastic strain curves. Surprisingly, the effective response is almost the same for both types of interface distributions. It should be noted that again all examples considered show significant size effects of Hall-Petch type, and are attributed to the presence of the interfacial energy-like term; in particular, these homogeneous examples would exhibit no scale effects whatsoever, in the absence of this term.

Chapter 6 is concerned with more interesting types of interfaces that are present between different phase materials, such as those present in metal-metal nanocomposites. Therefore the comparison method is applied to one-dimensional heterogeneous media in which the interfaces that inhibit plastic flow are distributed either periodically or randomly. Again to obtain the solution for the random linear comparison medium, statistics taking into account two points at a time are considered. Unlike, in the homogeneous examples, the effective response for the periodic and random media does not exhibit close numerical proximity for all specimen sizes considered. This may be attributed to a greater extent to the randomness of the phases, instead of the random interface distribution.

To better examine the effect of interfaces between different materials, in particular for the case of metal-fiber/metal-matrix composites, a three-dimensional axially symmetric configuration, which is strained in tension, under generalized plain strain conditions, is modeled in Chapter 7. First, the variational principle of Chapter 3 is slightly modified so as to account for complete incompressibility and then solutions are obtained when both fiber and matrix have a linear gradient plastic response, along with a linear or nonlinear interfacial response. The main purpose of this chapter is to illustrate the features of the proposed formulation in higher dimensions; a highly nonlinear gradient potential is therefore not considered.

In Chapter 8, finally, the existence of an "interfacial yield" stress is demonstrated through nano-indentation experiments on a Fe-14%Si bicrystal. It is shown that as the distance of the indenter tip to the grain boundary decreases the stress required for dislocation transference is increased. Since this is analogous to the Hall-Petch trend observed in the previous chapters, the experimental data are fitted to the theoretical expression for the "interfacial yield" stress (that was obtained in Chapter 4) and therefore estimates for the coefficients that come into play within this continuum formulation, such as the

internal length and interfacial energy-like term, are derived. This thesis, therefore, illustrates new aspects in both theory and experiment: It presents a new theoretical approach for the treatment of internal surfaces, and demonstrates the novel features resulting from this formulation through nano-indentation experiments.

CHAPTER 2

GRAIN-BOUNDARIES AND INTERFACES: A PHYSICAL DESCRIPTION

The gradient plasticity theory developed in this thesis is the first continuum plasticity model to take explicitly into account the presence of grain boundaries and interfaces, their interaction with lattice dislocations and their effect on the overall material deformation and plastic flow. This is done by properly introducing an excess "interfacial energy" term into an overall energy functional and assuming that plastic strain gradients and their conjugate higher-order stresses are discontinuous across interfaces, while displacements and plastic strains remain continuous throughout the whole domain under consideration. The physics behind this mathematical model are dictated by the structure of grain boundaries/interfaces and their interaction with the bulk as this is determined through the motion and reaction of dislocations. These interaction processes may include the formation and destabilization of dislocation pileups in front of interfaces, the absorption and production of dislocations by grain boundaries, as well as the production/ annihilation of boundary ledges leading,

among other things, to discontinuities of plastic deformation gradients across interfaces.

As this is the first time to attempt incorporating into a continuum plasticity theory such details of dislocation-interface interactions, only the dominant physical mechanisms are considered in the corresponding mathematical formulation for the sake of simplicity and effectiveness of the model proposed. These physical mechanisms are briefly discussed in this chapter which also provides a review of the structure of interfaces and their interactions with dislocations. Emphasis is given to grain boundaries as these planar defects are among the most common and well-understood internal boundaries and their central role in plastic flow is well-documented. Their crystallography is briefly reviewed in Section 2.1, while a related structural unit model is presented in Section 2.2 for high-angle grain boundaries in terms of a corresponding dislocation network which is also used to derive an expression for the grain boundary energy. In this connection, interfaces other than grain boundaries, as those occurring in multilayer films, superalloys, and metal-metal nanocomposites are discussed in Section 2.3. Finally, in Section 2.4 and Section 2.5 dislocation-boundary interactions, which motivate the gradient development of Chapter 3 are examined. The purpose of this chapter, as well as that of Chapter 8, is to pave the way for obtaining microscopic expressions for the phenomenological coefficients of the continuum theory developed and evaluated in Chapters 3-6, design appropriate tests for the experimental determination of these coefficients, and provide sufficient physical and experimental background for future improvements of the theory.

2.1 CRYSTALLOGRAPHIC DESCRIPTION

Grain boundaries, constituting the boundary between two single crystals of the same phase with different orientation, are the most common interfaces present in

polycrystalline materials. A grain boundary has 8 degrees of freedom: the misorientation axis and angle, the boundary plane normal and the relative translation of the two grains with respect to each other. For ordered alloys the position of the boundary plane in the direction of its normal, corresponding to different chemical compositions of the boundary plane, is an extra degree of freedom. Grain boundaries may be of the *tilt* type (the rotation axis is in the grain boundary plane) or of the *twist* type (the rotation axis is perpendicular to the grain boundary plane) (Fig. 2.1).

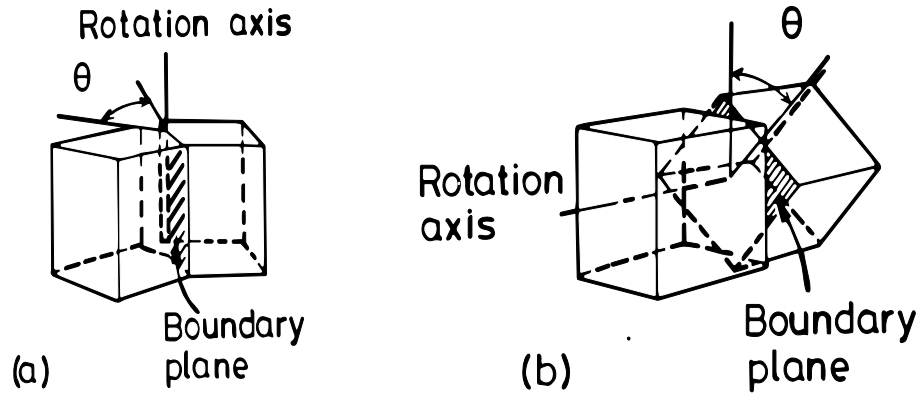

Fig. 2.1: Grain boundary types. (a) Tilt boundary. The misorientation axis lies in the boundary plane. (b) Twist boundary. The rotation axis is perpendicular to the boundary plane

A general grain boundary can be of tilt, twist, or mixed tilt and twist character. Several models have been proposed to describe the structure of grain boundaries. For example l*ow angle grain boundaries* (i.e. low misorientation angle) can very well be described by means of a dislocation network (Fig.2.2). The dislocation spacing *d* for a simple case like the symmetric tilt grain boundary then follows from:

$$d = \frac{b}{2\sin(\theta/2)} \approx \frac{b}{\theta}, \qquad (2.1)$$

where θ and b are the misorientation angle, and the magnitude of the Burgers vector. For misorientation angles higher than about 10^o the dislocation spacing decreases so much that individual dislocations cannot be discriminated any more and the model has less physical meaning. A more general low-angle grain boundary procedure for finding the dislocation structure was devised by Frank [36], a brief description in given in Appendix 1.

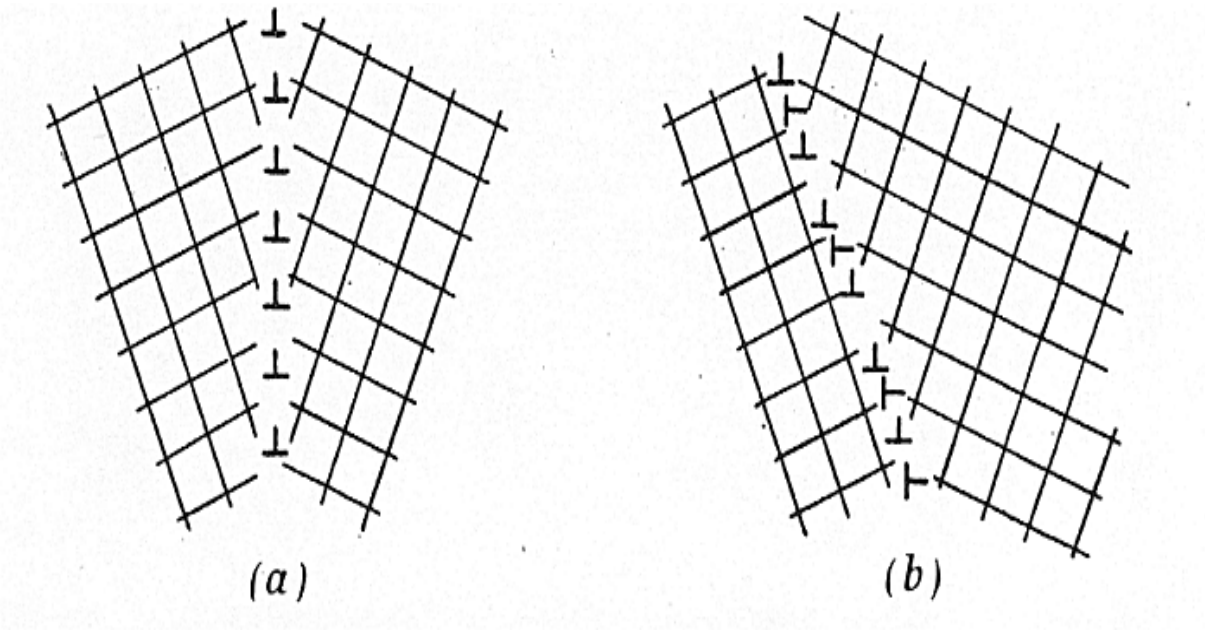

Fig. 2.2: a) symmetric tilt grain boundary; b) antisymetric tilt grain boundary

A model that is not restricted to low misorientation angles is the *Coincidence Site Lattice* (CSL) model [37,38]. This model uses the *dichromatic pattern* which is created by hypothetically allowing the lattices of the two grains to interpenetrate. The lattice sites belonging to grain 1 are considered white whereas those of grain 2 are black. For certain misorientations a new CSL (super) lattice of coincident lattice sites of the white and the black lattice exists (Fig. 2.3a). The parameter Σ is defined as the ratio between the volume of the CSL unit cell and the primitive unit cell. The density of coincident lattice sites in space equals $1/\Sigma$. A grain boundary is constructed by inserting a plane in the dichromatic pattern and

letting the atoms occupy the white sites on one side of the plane and the black sites on the other side of the plane. The location of the plane can be chosen such that it intersects coincidence points (Fig. 2.3b).

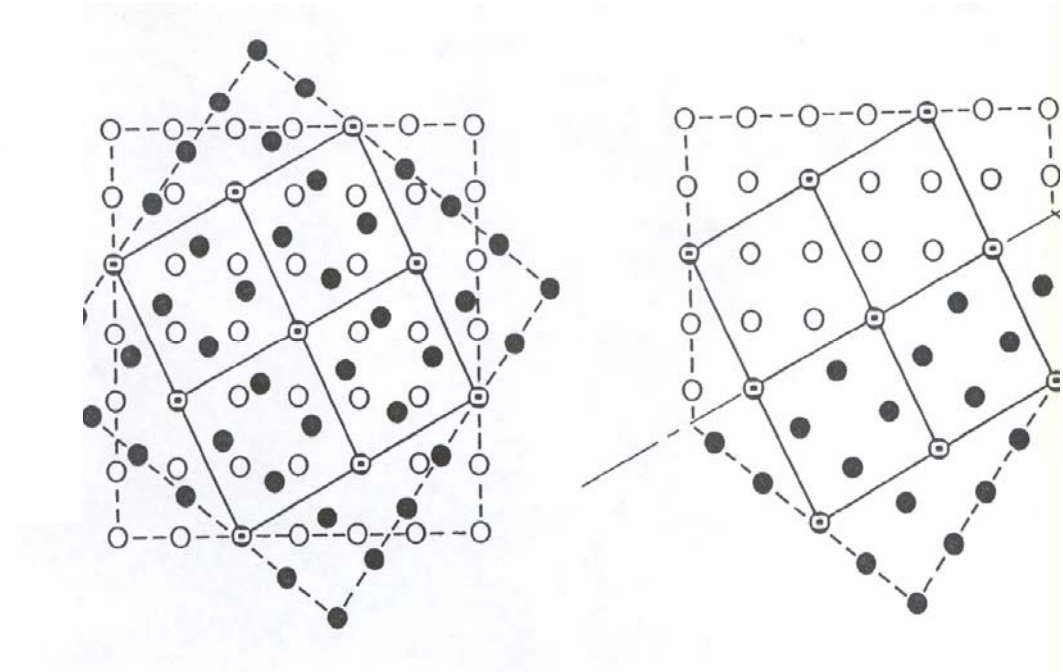

Fig. 2.3: (a) The dichromatic pattern of a $\Sigma 5$ boundary in a simple cubic structure. Projection along the [1 0 0] direction. Coincidence of black and white sites is indicated by black sites containing a white circle. The solid lines connecting the coincident sites indicate the Coincidence Site Lattice (CSL). The CSL periodicity in the [1 0 0] direction out of the plane of the paper is equal to the lattice periodicity.b) Grain boundary constructed on the basis of the dirchromatic pattern of (a). The broken line indicates grain boundary plane.

In the early stages of the development of this model, it was reasoned that a high density of coincidence sites in the boundary plane would mean a low grain boundary energy. Nowadays, it is considered that this relation is not so simple [39], but for some low (and thus high density of coincidence sites) boundaries indeed lower energies are found; this is shown in Fig. 2.4, which illistrates the cusps in the measured grain-boundary energy as a function of misorientation for a symmetric [110] tilt boundary in NiO. It can be seen that there is no cusp at the $\Sigma 9$ misorientation with boundary planes $\{114\}$ at 141^{o} despite the low value of Σ [46].

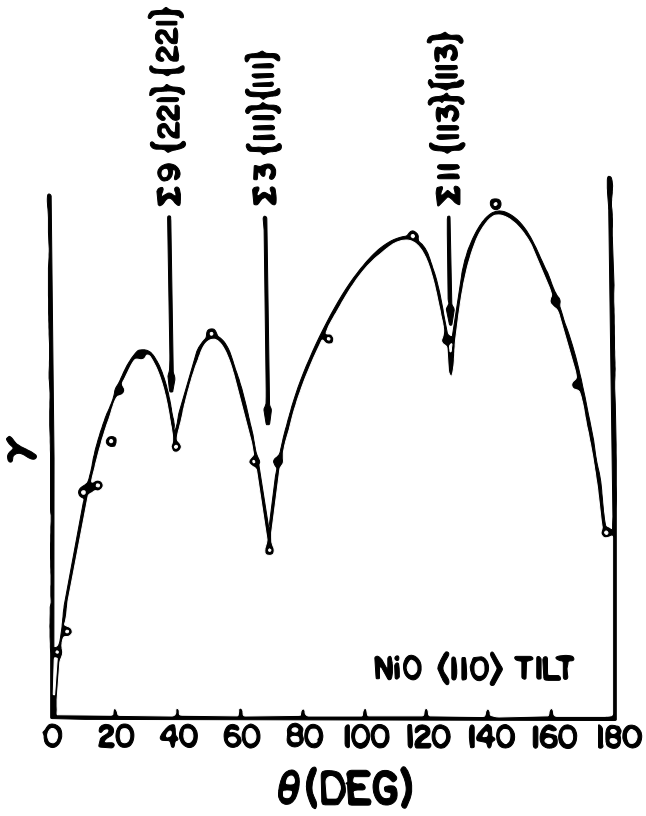

Fig.2.4: Cusps in the measured grain-boundary energy as a function of misorientation of a symmetric [1 1 0] tilt boundary in NiO

Also it has been established that there may exist a relative translation away from exact coincidence for the equilibrium structure of a low boundary and the individual atoms at the grain boundary plane may have been displaced. It has to be noted that the CSL is a mathematical model: an infinitesimal rotation or translation of one grain with respect to the other destroys the whole CSL. Nevertheless, a grain boundary with the same misorientation but translated away from coincidence is still regarded as being a boundary of the same special coincidence and as having the same value. The translational symmetry of such a boundary is the same as that of the boundary in exact coincidence.

The *Displacement-Shift-Complete* (DSC) lattice [38,41] of a bicrystal in CSL orientation is the lattice of the displacement vectors of one grain with respect to the other that keep the dichromatic pattern (black and white sites) unchanged

except for a translation. In other words, if the black lattice is displaced over a vector belonging to the DSC lattice, the black atoms that were in coincidence with the white atoms may have lost their coincidence, but somewhere else black and white atoms will now be in coincidence and the dichromatic pattern (and the CSL) will have the same shape as before (see Fig. 2.5). The DSC lattice is the coarsest lattice that contains both crystal lattices of the two grains as sublattices. It has smaller unit vectors than the unit vectors of perfect lattice. Note that each CSL has a specific DSC lattice associated with it. The fact that the dichromatic pattern is unchanged for a displacement over a DSC vector of one grain with respect to the other has consequences for the types of Burgers vectors that are allowed for dislocations in the grain boundary plane. A perfect dislocation must have a Burgers vector that is a translation vector of the material in which it exists. Now, if we have a grain boundary, we have just seen above that a displacement over a vector that belongs to the DSC lattice leaves the dichromatic pattern unchanged except for a translation. Thus, in a grain boundary, *grain boundary dislocations* (also called *DSC dislocations*) with Burgers vectors belonging to the DSC lattice can exist. The displacement over a DSC vector may cause a shift in the dichromatic pattern, over a vector, called the *step vector* (Fig. 2.5).

The dislocation is then associated with a step in the grain boundary plane, located at the core of the dislocation [42,43]. The height of the step in the grain boundary plane can conveniently be expressed in terms of *interplanar spacings*, i.e. the distance between crystallographic planes parallel to the boundary plane. Dislocations in a grain boundary having a Burgers vector that belongs to the DSC lattice and that is not a lattice translation vector of either grain can only exist in the grain boundary and the movement of these dislocations is constricted to the grain boundary plane. As the DSC lattice is specific to a CSL orientation, each grain boundary has specific allowed Burgers vectors for grain boundary dislocations.

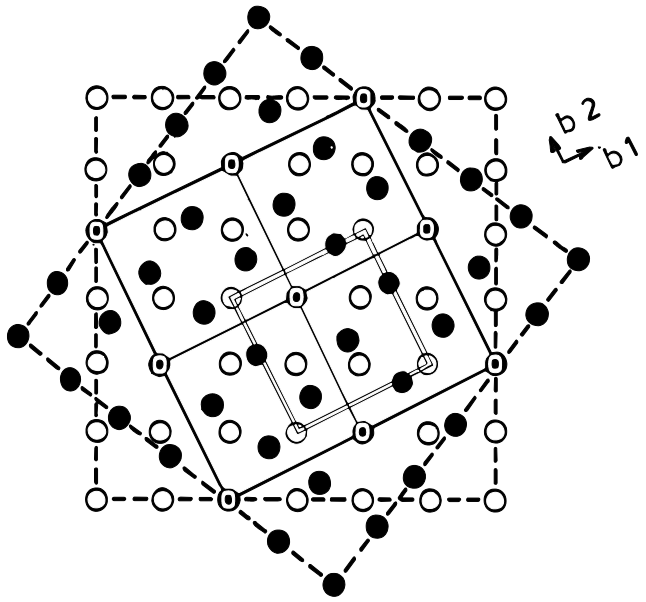

Fig. 2.5: Same boundary as Fig. 2.3. The basis vectors b_1 and b_2 of the DSC-lattice belonging to this boundary are indicated. b_3 points out of the plane of the paper. The double lines indicate the new location of a CSL unit cell if the black lattice is translated with respect to the white lattice over b_1. The vector connecting the original and the new position of the CSL unit cell is called the step vector associated with the b_1 DSC vector.

2.2 STRUCTURAL UNIT MODEL

A model for the structure of high angle grain boundaries was proposed in [39,44,45]. Periodic boundaries with a low index rotation axis (rotation axis [h k l], with h, k, l small) but not having a high degree of coincidence are described in terms of boundaries with a high degree of coincidence and the same rotation axis. When the misorientation changes, the structure of a high coincidence boundary is thought to be preserved as much as possible, with periodic localized disturbances in the boundary plane, called "structural units", which are characteristic of the high coincidence boundary that is next in misorientation. This model can also be described in terms of dislocations. A high coincidence boundary is described as a very evenly and very closely spaced dislocation network, called the primary network (as stated before, this network has little physical meaning). A low coincidence boundary is considered to be established

on the basis of a high coincidence boundary with nearby misorientation. This high coincidence boundary is thought to contain, in addition to the primary network, a widely spaced dislocation network to accommodate the misorientation difference. This dislocation network is termed secondary dislocation network and the spacing of this network is of course much larger, as it describes the smaller misorientation *difference* between the low and the high coincidence boundary. This model was confirmed by observations of dislocation networks in near coincidence twist and tilt boundaries in gold [46,47]. The spacing of the dislocations in the networks could be related to the difference between the measured misorientation and the exact misorientation of the high coincidence boundary.

Based on the model mentioned above and on computer simulations of grain boundaries in fcc metals, a so-called *structural unit model* has been developed [48,49]. In the structural unit model, certain boundaries are found to be the constituting elements of other boundaries in the same misorientation range. The boundaries that consist of only one element are called *favored boundaries*. Boundaries that are not favored consist of elements (or building blocks), called *structural units* of favored boundaries in the nearby misorientation range. It was found that favored boundaries were not always associated with lowest Σ values. An example of the application of the structural unit model from computer simulations is given in Appendix 1.

As an illustration of the physical description of grain-boundaries we take {111} twist boundaries in fcc materials. The most important symmetry element governing structural features of (111) twist boundaries is the [111] threefold screw axis of the cubic lattice, which any dislocation (111) twist grain boundaries in f.c.c. metals network present in these boundaries must possess. Such networks have either triangular or hexagonal symmetry. In general, such a network consists of three different types of dislocations with Burgers vectors $\vec{b}_i$ (i = 1, 2, 3) for which

$$\sum_i \vec{b}_i = 0\,. \tag{2.2}$$

The average separation, d, of dislocations in each set, is determined by Frank's formula [36]. This condition can be expressed most conveniently by introducing the vectors [54]

$$\vec{N}_i = N_i(\vec{n} \times \xi_i)\,, \tag{2.3}$$

where $\vec{n}$ is the unit vector in the direction of the boundary normal and ξ_i is the unit vector in the direction of the dislocations of type i. Furthermore,

$$N_i = 2d_i \sin\left(\frac{\Delta\theta}{2}\right)^{-1}, \tag{2.4}$$

where $\Delta\theta$ is the misorientation across the boundary away from a reference state and d_i the average separation of dislocations of the set i. Owing to the threefold symmetry

$$\sum \vec{N}_i = 0\,, \tag{2.5}$$

and the magnitudes of all three vectors $\vec{N}_i$ are the same. Hence all the average separations d_i are also the same and in the following they are marked d. Noting that the rotation axis is in this case parallel to the boundary normal, Frank's formula reads

$$\vec{V} \times \vec{n} = \sum_i \vec{b}_i(\vec{N} \times \vec{V})\,, \tag{2.6}$$

where $\vec{V}$ is an arbitrary vector in the boundary plane. Using conditions (2.2) and (2.5), (2.6) can be written as

$$\vec{V} \times \vec{n} = (2\vec{b}_1 + \vec{b}_2)(\vec{N}_1 \times \vec{V}) + (\vec{b}_1 + 2\vec{b}_2)(\vec{N}_2 \times \vec{V})\,, \tag{2.7}$$

and since it has to be satisfied for any vector $\vec{V}$ it represents six linear equations for the components of the vectors $\vec{N}_1$ and $\vec{N}_2$. In the coordinate system for which

the x-axis is parallel to the boundary normal, $\vec{n}$, and the y-axis is parallel to the projection of the Burgers vector $\vec{b}_1$ in the boundary plane; the solution is $\vec{N}_1 = 1/b[0,-2/3,0]$ and $\vec{N}_2 = 1/b[0,-1/3,1/\sqrt{3}]$, where b is the magnitude of the projection of the Burgers vectors of the dislocations to the boundary plane (owing to the threefold symmetry b is the same for all three types of dislocations). The Burgers vectors of these dislocations may have components perpendicular to the boundary but it follows from (2.2) and (2.7) that these components have to satisfy the conditions $b_{2\perp} = b_{3\perp} = -b_{1\perp}/2$.

When the vectors $\vec{N}_1$ and $\vec{N}_2$ are known the average separation of the dislocations of the network can be found using (2.4). In the present case this gives [55]

$$d = \frac{3b}{4\sin(\Delta\theta/2)}. \tag{2.8}$$

In the case of regular triangular networks d is directly the separation of the dislocations forming the sides of the triangles. In regular hexagonal networks dislocations forming a given set of parallel sides of the hexagons are effectively broken into segments, the total length of which is equal to the one third of the length these dislocations would have if they were not segmented. Hence the separation of the dislocations forming a given set of the sides of the hexagons is equal to $d/3$.

When well-localized dislocations can be identified in grain boundaries a significant elastic energy is associated with such a network. This was first recognized by Read and Shockley [56], who evaluated this energy as a function of $\Delta\theta$ for pure tilt boundaries and showed that it is responsible for the existence of cusps on a plot of the energy against misorientation dependence for misorientations corresponding to certain special boundaries which serve as reference structures for other grain boundaries. An exact evaluation of the elastic energy of a tilt boundary as the strain energy of a wall of edge dislocations is

presented in [54] for the case of isotropic elasticity. For a small angle tilt boundary the energy per unit of area of the boundary becomes

$$\gamma^{tilt} \cong \gamma_0 + A\Delta\theta(B - \ln\Delta\theta), \tag{2.9}$$

where

$$A = \frac{\mu b}{4\pi(1-\nu)}, \tag{2.10}$$

and

$$B = \frac{4\pi(1-\nu)E_c}{\mu b^2} - \ln\alpha\,. \tag{2.11}$$

The core-radius of the grain-boundary dislocation is expressed as $r_c = \alpha b$, while E_c refers to the core energy per unit length, μ and ν are the shear modulus and Poisson's ratio, respectively, and γ_0 is the energy of the corresponding reference state.

The calculation of a screw dislocation network representing a twist grain boundary is more complicated. Using the same method, the elastic energy of a rectangular network of screw dislocations, applicable to (001) twist boundaries, has been derived in [57]. A similar calculation is presented in the sequel for a network composed of three sets of screw dislocations, which is a good approximation for dislocation networks found in (111) twist boundaries.

To evaluate the elastic energy of a network of screw dislocations, we consider in a similar fashion to [54, p.740], a pair of such networks of opposite sign in an infinite crystal. The specific energy of formation of such a pair, when well separated, is then twice the energy per unit area of the network. The average separation of the dislocations in this network given by Frank's formula (2.8), is d, and owing to the threefold symmetry the average length of the dislocations separated by d is $l = 2d/\sqrt{3}$. The zy plane is taken to be the plane of the boundary, and one set of dislocations is parallel to the z-axis. The force in the x

direction (perpendicular to the boundary) per unit length of a dislocation of opposite sign which lies parallel to the *z*-axis is $-\sigma_{23}b$, where again b is the magnitude of its Burgers vector and σ_{23} the corresponding component of the stress field associated with the network in the *zy* plane. The energy per length l per dislocation in one boundary can then be calculated as one half of the interaction energy of this dislocation with the dislocation network and is equal to

$$W = \frac{1}{2}\int_0^l \int_{r_0}^{\infty} \sigma_{23} b dx dz , \tag{2.12}$$

where r_0 is the core radius of the dislocation. The elastic energy per unit area of the boundary is then

$$\gamma_{el} = \frac{W}{S} = \frac{3}{4}\sqrt{3}\frac{1}{d^2}\int_0^l \int_{r_0}^{\infty} \sigma_{23} b dx dz , \tag{2.13}$$

where $S = l^2/2\sqrt{3} = 2d^2/3\sqrt{3}$ is the area per dislocation segment of length l . In the framework of linear isotropic elasticity the stress field associated with the dislocation network can be evaluated as a sum of the stresses of individual dislocations. Following the same procedure as employed in the case of the wall of edge dislocations [54, p.731], it is obtained that for the network of three screw dislocations related by a threefold axis symmetry operation

$$\sigma_{23} = \frac{\mu b}{2d}\left[\frac{2\sinh\left(\frac{2\pi x}{d}\right)}{\cosh\left(\frac{2\pi x}{d}\right)-\cos\left(\frac{2\pi y}{d}\right)} - \frac{\sinh\left(\frac{2\pi x}{d}\right)}{\cosh\left(\frac{2\pi x}{d}\right)-\cos\left(\frac{\pi(z\sqrt{3}+y}{d}\right)} + \frac{\sinh\left(\frac{2\pi x}{d}\right)}{\cosh\left(\frac{2\pi x}{d}\right)-\cos\left(\frac{\pi(z\sqrt{3}-y}{d}\right)}\right] , \tag{2.14}$$

where μ is the shear modulus. After inserting (2.14) into (2.12) and (2.13) (for y=0) and carrying out the integration it is found that

$$\gamma_{el} = \frac{\mu b^2}{4\pi d}\left\{\ln\left[\cosh\alpha + \sqrt{\cosh\alpha^2 - 1}\right] - \ln(\cosh\alpha - 1) - \ln 2\right\}, \qquad (2.15)$$

where $\alpha = 2\pi r_0 / d$. For small misorientations, i.e. $\Delta\theta \ll 1, d \approx 3b/2\Delta\theta \gg r_0$ and $\alpha \ll 1$, $\cosh\alpha$ can be written as $\cosh\alpha \approx 1 + \alpha^2/2$. It thus follows that neglecting all the terms of order higher than α in (2.15) allows γ_{el} to be expressed as

$$\gamma_{el} = \frac{\mu b^2}{2\pi d}\left[\frac{\pi r_0}{d} - \ln\left(\frac{2\pi r_0}{d}\right)\right]. \qquad (2.16)$$

Furthermore, using the above relation for d it is concluded that

$$\gamma_{el} = \frac{\mu b}{3\pi}\left[\frac{2\pi r_0}{3b}\Delta\theta + \ln\left(\frac{3b}{4\pi r_0}\right) - \ln\Delta\theta\right]\Delta\theta. \qquad (2.17)$$

This formula is very similar to that obtained for a square grid of screw dislocations. It should be noted that the term $(2\pi r_0/3b)\Delta\theta$ inside the square brackets in (2.17) cannot be neglected with respect to other terms, particularly when $b \ll r_0$ since this is often the case for grain boundary dislocations whose Burgers vectors are usually smaller than the spacing of nearest neighbors, which is a lower limit for r_0. No such term exist in the same approximation when evaluating the energy of a wall of edge dislocations. The energy of the grain boundary is then

$$\gamma^{twist} = \gamma_0 + \gamma_{el}, \qquad (2.18)$$

where γ_0 is the energy of the corresponding reference state. This leads to the energy against misorientation dependence, with cusps at $\Delta\theta = 0$. Qualitatively this dependece is similar to that observed in Fig. 2.4.

2.3 OTHER TYPES OF INTERFACES

The mathematical theory to be developed in Chapter 3 is not restricted to boundaries in homogeneous media, i.e. grain boundaries, but is also applicable to more general situations such as interfaces in metal-metal nanocomposites and superalloys, as well as multilayer films. Although less is understood for such boundaries, in particular since metal-metal nanocomposites are in an experimental stage, it is essential to give a brief overview of types of interfaces present in chemically heterogeneous systems. These interphase interfaces are classified as *coherent , semicoherent* or *incoherent* depending on the mismatch of the adjacent lattices at the interphase plane.

Coherent boundaries are present when the lattices of the two crystals match perfectly; an interfacial energy, however, is still present since at the interface there is a change in composition and each atom is bonded to the wrong neighbor. The relatively small atomic mismatch that may be present is accommodated by coherency strains. Since these strains increase the interface free energy, it follows that for significant atomic misfit, i.e when the atomic separation is very different in the two adjoining phases, it becomes energetically favorable to release the coherent strains by misfit dislocations, hence producing *semicoherent* interfaces. The energy of such interfaces is higher than the coherent ones since in addition to the energy term that results from the difference in chemical composition across them (and is equal to the energy of a fully coherent interface), the lattice misfit δ (which determines the dislocation spacing) gives rise to a structural energy term. When δ>0.25 the dislocation cores begin to overlap and the interface becomes completely *incoherent*. *Incoherent* interfaces are therefore present between crystals that have very different compositions, and structures at the interface plane, or they may be formed by joining two randomly oriented crystals across an interface plane. They are characterized by a very high energy, which is not

dependent on orientation, but very little is known about them; they are believed to behave like high-angle grain boundaries.

It is interesting to note that coherent interfaces have low energies, which range up to 200mJ/m^2, in particular it has been estimated that for certain boundaries in Cu-Si alloys these energies reach a low value of 1mJ/m^2; semicoherent interfaces have an energy range between 200-500mJ/m^2; while incoherent interfacial energies vary within the values 500-1000mJ/m^2.

The aforementioned interfacial energies values, have been determined experimentally, and account for the density of the interfacial "free energy" term Γ that arises from the presence of interfacial material, and determines the total free energy of the system through the equation

$$G = G_o + A\Gamma, \tag{2.19}$$

where G is the total free energy, G_o is the free energy of the bulk material (with no interfaces) and A is the interfacial area. It should therefore be emphasized that these "classical" interfacial energies are substantially different from the interfacial term that is proposed in the subsequent novel formulation. In particular, the "interfacial energy" that will be introduced in Chapter 3 is induced by plastic deformation, and provides a measure of the resistance of interfaces to dislocation motion. It is additional to Γ and is dissipative in character. Non-equilibrium kinetics and dislocation considerations (e.g. misfit or threading dislocations) can be considered to model the interaction of adjacent phases, and hence the interfacial strength, which in connection with physical input can provide estimates for the phenomenological coefficients used in the continuum gradient plasticity model developed in Chapter 3. The most reliable way, however, to obtain estimates for these new coefficients is to design and perform experiments, which give information about dislocation motion during plastic deformation. This will be shown in Chapter 8.

2.4 DISLOCATION-BOUNDARY INTERACTIONS

The degree to which grain boundaries hinder the motion of dislocations is crucial for the occurrence of failure. Because of the hindrance of dislocation movement, stress concentrations develop that eventually may lead to intergranular fracture along the grain boundaries. If the grain boundary contains a secondary, widely spaced dislocation network (Section 2.2), or if there are already extrinsic grain boundary dislocations present in the grain boundary plane, there may be elastic interaction with a long range character between the dislocations in the grain boundary and the lattice dislocations. After entering the boundary, the dislocation will almost always alter the plane on which it propagates and the resolved shear stress on this plane, resulting from the externally applied stress, will change. It is known from crystallography that the dislocation may be absorbed in the grain boundary plane, reducing its elastic energy by dissociating into grain boundary dislocations.

Lattice dislocations will experience different forces when they approach interfaces. In particular, the force ($\vec{F}$) on a dislocation is due to the sum of applied stress ($\overline{\tau}_A$), compatibility stress ($\overline{\tau}_C$), intrinsic stress ($\overline{\tau}_I$) and extrinsic stresses ($\overline{\tau}_E$) due to other lattice dislocations. The force is therefore given by

$$\vec{F} = \vec{t} \times \hat{\xi}; \quad \vec{t} = \overline{\tau}\,\vec{b} \left(or\ t_i = \overline{\tau}_{ij} b_j \right), \quad \overline{\tau} = \overline{\tau}_A + \overline{\tau}_C + \overline{\tau}_I + \overline{\tau}_E , \tag{2.20a}$$

where $\overline{\tau}$ is the total stress tensor, $\vec{b}$ denotes the Burgers vector and $\hat{\xi}$ denotes the tangent unit vector along the dislocation line. In addition, because of the difference in elastic constants across a heterophase interface, image forces are exerted on the lattice dislocation. The image force for a screw dislocation parallel to the interface in medium 1 at a distance d feels an image force that is given by

$$\vec{F}_{image} = \frac{\mu_1(\mu_2 - \mu_1)b^2}{4\pi(\mu_1 + \mu_2)} \frac{1}{d} \hat{x} . \tag{2.20b}$$

When medium 1 is harder than medium 2 the dislocation is repelled from the interface in the positive $\hat{x}$ direction and vice versa. The situation for edge dislocations is somewhat more complicated and solutions have been discussed in [13] whereas interface dislocations are treated in more complex situations in [14,16,58,59]. It turns out that in a general case, taking into account anisotropy effects, the image force on a lattice dislocation can be formulated as

$$\left|F_{image}\right| = \left|E_{i,dis} - E_{\infty}\right| \frac{1}{d}, \tag{2.21}$$

where $E_{i,dis}$ is the energy of the dislocation right at the interface and E_{∞} the energy of the same dislocation in an infinite anisotropic crystal [60]. Simple calculations show that $\left|F_{image}\right|$ can easily reach a value of $10^{-3}\mu b$ for a lattice dislocation at a distance of $10b$ from the interface.

The compatibility stress in (2.20a), which is due to the difference between plastic strains in the two media having a boundary in-between, is related to the difference in strain components in medium 1 and medium 2

$$\tau_C \propto \mu \Delta \varepsilon_{ij}^{1,2}, \tag{2.22}$$

where the strain fields in terms of the slip direction $\hat{p}$ and slip plane normal $\hat{q}$ are

$$\varepsilon_{ij}^{1,2} = \frac{1}{2}\sum_n \left(p_i^n q_j^n + p_j^n q_i^n \right). \tag{2.23}$$

Depending on the anisotropy of the system the compatibility stress can be of the same order of magnitude as the applied stress.

Under an applied stress a number of interaction processes between lattice dislocations and grain boundaries may be discriminated, as seen in Fig. 2.6.:

(i) A dislocation may move into the grain boundary, while another lattice dislocation emerges from the grain boundary into the other grain. As the other grain has a different orientation, the outgoing dislocation may have a Burgers vector that differs from the incoming dislocation. A residual dislocation remains

in the boundary plane with a Burgers vector that is equal to the difference of the Burgers vector of the incoming and outgoing dislocation. The residual dislocation is always a DSC dislocation. This mechanism is referred to as transmission.

(ii) The incoming lattice dislocation can dissociate into grain boundary dislocations or DSC dislocations. In this way the elastic energy of the dislocation can be reduced. This mechanism is referred to as absorption. Between the grain boundary dislocations, a step (ledge) in the grain boundary plane may be created. Certain atoms, which belonged to the lower grain before the lattice dislocation was absorbed, end up in the upper grain after absorption and hence have to adapt their positions to the lattice of the upper grain. If the step in the grain boundary plane is larger than one interplanar spacing, the adaptation cannot be achieved by means of a simple rigid-body translation, and a less ordered relocation, called *shuffling*, of the atoms takes place. Analogous to lattice dislocations, grain boundary dislocations may dissociate in the grain boundary plane into partial grain boundary dislocations, creating a fault in the grain boundary plane between them.

(iii) In addition there are more complex mechanisms, like absorption and re-emission of a lattice dislocation at another site in the boundary.

The grain boundary dislocations that stem from an absorbed lattice dislocation or that are the residual dislocations after transmission of a lattice dislocation are called extrinsic grain boundary dislocations, as opposed to intrinsic grain boundary dislocations, which form the secondary dislocation network in a grain boundary. Besides these mechanisms describing the interaction between lattice dislocations and grain boundaries, dislocations may be nucleated at the grain boundary. A grain boundary can act as a source of dislocations that can be generated under the influence of a stress field. The dislocations can be generated in either grain and in the boundary plane. For the case of transmission of a lattice dislocation into the other grain, a number of

criteria for the selection of the slip system in the other grain have been proposed. Criteria have also been proposed based on post-deformation observations and in-situ deformation experiments using Transmission Electron Microscopy [65].

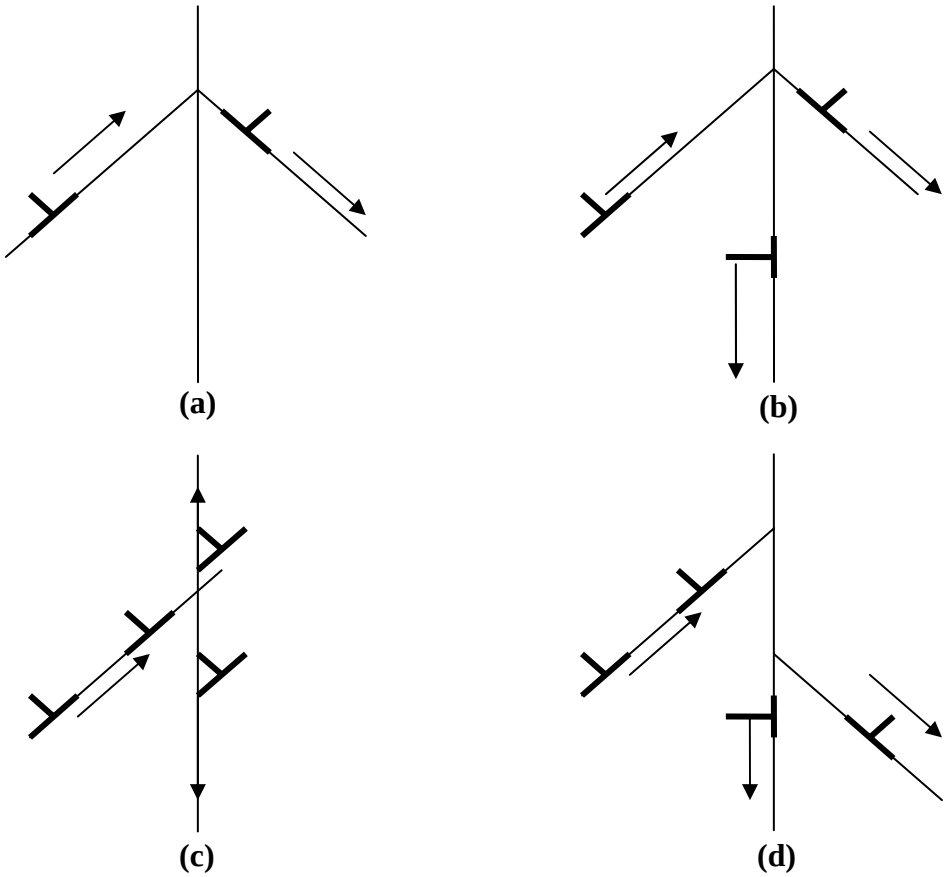

Fig. 2.6: Interaction mechanisms between lattice dislocations and grain boundaries. Conservation of the Burgers vector requires:

$$\sum_i \vec{b}_i^{(IN)} = \sum_j \vec{b}_j^{(OUT)} + \sum_k \vec{b}_k^{(GB)}$$

a: direct transmission by cross-slip of screw dislocations. Both slip systems intersect along a common line in the boundary and the Burgers vector does not change; b: transmission with the creation of a residual dislocation along the boundary. Both slip systems intersect along a common line in the boundary but upon crossing the Burgers vector changes; c: absorption: the lattice dislocation dissociates in the grain boundary plane into DSC (or grain boundary-) dislocations and a step in the grain boundary plane is created between the DSC dislocations. No transmission in the other grain; d: No common line of intersection of the slip systems. Glissile GB dislocations are produced and pile up in front of a step that acts as an obstacle. The pile-up produces high enough stresses to generate outgoing dislocations. A residual dislocation is left behind at the grain boundary.

In fact, in-situ deformation in a TEM is one of the very few techniques by which the development of the interaction between lattice dislocations and interfaces can be studied and which at the same time allows one to analyze the configuration. By this technique, samples which have not yet been deformed are strained inside a TEM in a special straining holder. In practice there are a number of complexities. The dislocations may have high velocities and therefore they may be difficult to observe when moving. As the strains are usually very small in in-situ experiments, the deformation is not homogeneous and therefore it may take place in a different part of the sample; e.g. in the region that is not transparent for electrons or in a part of the electron transparent region that is not in contrast at that moment. In addition, it is always possible that there is a substantial influence of the fact that the interaction is studied in a very thin foil, while we are interested in bulk properties; since the electron transparent region may have a complicated geometry because of the thinning and therefore the stresses in the thin region may be different from the bulk stress state. Further, an oxide layer on the surfaces may hinder the motion of dislocations. Therefore, care must be taken to study the interactions in the thicker regions of the foil. Nevertheless, in many cases, the in-situ TEM technique is a promising tool for investigations of dislocation-grain boundary interactions [13b]. As the state prior to deformation is known, the changes that have been introduced because of the deformation can be deduced even if the interaction has not been observed directly. Analogous to the slip lines at the surface of a bulk sample, each dislocation that moves may leave behind an atomic step in the surfaces of the thin foil. Under the right imaging conditions, these atomic steps give rise to a diffraction contrast and, therefore, even if a dislocation has not actually been seen to move, it may be possible to deduce the motion of a dislocation by the slip traces that it has left. Often cracks (some of which were already present before the deformation started) are observed during in-situ transmission electron microscopy straining experiments that have initiated at the edge of the thin foil,

propagating along planes. Dislocations are often seen to be emitted from the crack tip, in the plane of the crack and sometimes also on inclined planes. Quite frequently, the propagation of the crack occurred in a jerky type of motion and then, it is impossible to observe any dislocation motion. The schematics of Fig.2.6 illustrate what occurs during two in-situ TEM experiments in ordered alloys. In many of $L1_2$ ordered compounds, e.g. Ni_3Al, often coherent twin boundaries ($\Sigma 3$, 109.47^o around [110] with boundary plane), can be found in the electron transparent region (see Fig. 2.7). By tilting to an edge-on position, the boundary plane has been determined to be $(\bar{1}11)$, which is equal to $(\bar{1}1\bar{1})_{II}$. The index II indicates the co-ordinate system of the grain containing the dislocations. The plane of the crack that arose during an in-situ straining experiment was determined to be close to $(1\bar{1}1)$ and the slip plane of the dislocations was determined to be $(1\bar{1}\bar{1})_{II}$. By the $\vec{g}.\vec{b}$ invisibility criterion, the Burgers vector of the dislocations was determined to be parallel to $[1\ 1\ 0]_{II}$; this is the [1 1 0] direction that is common to both grains. The line direction was determined to be $[2\ 3\ 0]_{II} \pm 13^o$, which is close to the $[1\ 1\ 0]_{II}$ screw direction. As the [1 1 0] direction is common to both grains, the Burgers vector could remain the same in both grains and no residue is left in the boundary. The line vector is parallel to the intersection of crack plane and outgoing slip plane and thus, transmission could occur without rotation of the dislocation line in the boundary plane. So, this reflects the situation as shown in Fig.2.6(a), but because of the special crystallography this surely is a very special case. The large number of dislocations in Fig.2.7 indicates that there was a large force on the leading dislocation of a pile-up in front of the boundary, necessary to cause transmission of the dislocations to the other grain. Grain boundary sources of course cannot be ruled out as origin of the observed dislocations. However, very often, if operation of grain boundary sources is observed, there is generation of

dislocations on many different slip planes, while here, all the dislocations are on one single slip plane.

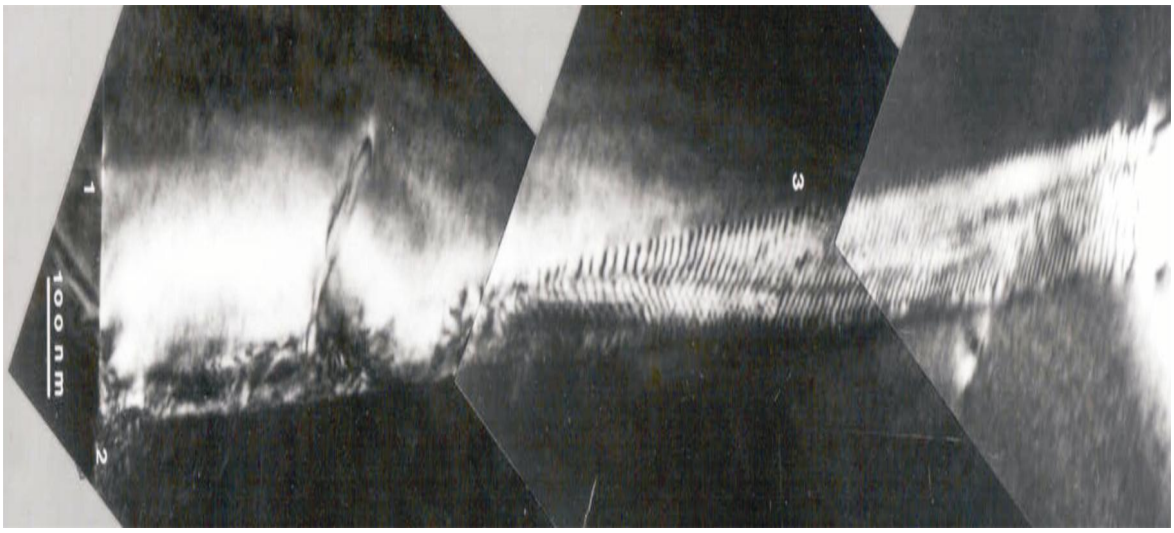

Fig. 2.7: The dislocation configuration attached to the slip lines.
1: crack, 2: boundary plane, 3: dislocation array [13b][64b,64c]

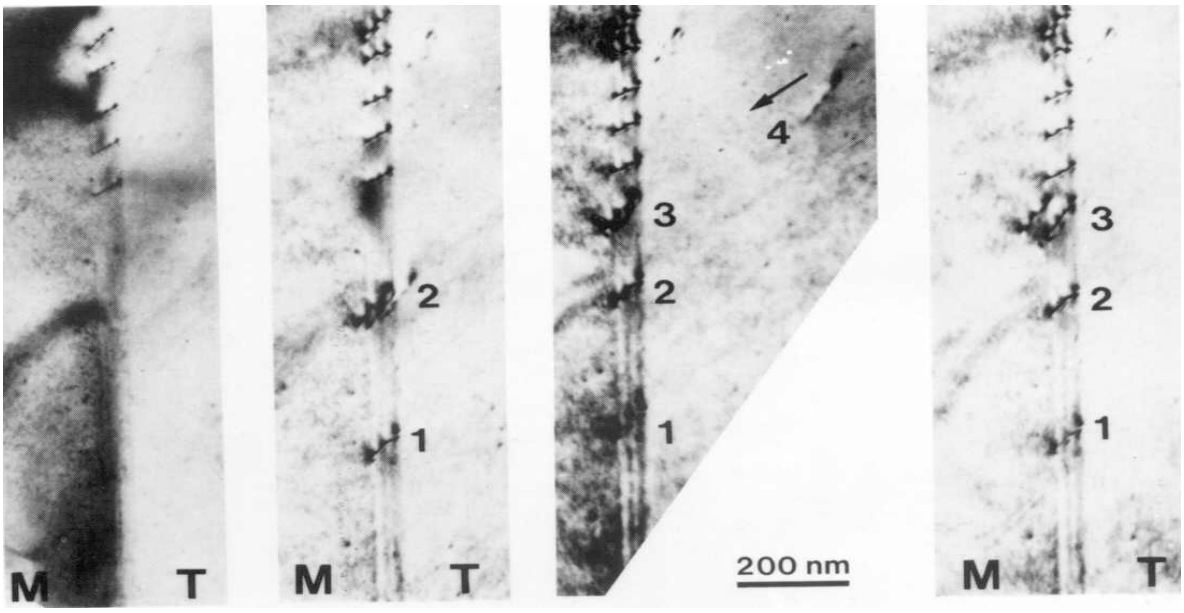

Fig. 2.8: In-situ TEM observations. Upon increasing strain (left to right) super lattice dislocations arrive at the boundary. Most of the super lattice dislocations are absorbed in the boundary. In the picture on the right, one super lattice dislocation is pushed out from the boundary into grain M upon increasing deformation [13b][64d].

In another example it can be concluded that most of the super lattice dislocations moving in an $L1_2$ alloy, i.e. in grain T in Fig. 2.8, were absorbed into the boundary plane. Also transmission was observed into grain M leaving slip traces in a direction parallel to the slip plane, but not at the same spot upon arrival. Upon increasing deformation, dislocations were seen to move slowly into grain M. Here the situation as schematically shown in Fig. 2.6(d) is common practice.

For the prediction of the slip plane, a geometrical criterion is used. The angle between the intersection line of the incoming slip plane and the grain boundary plane $\vec{I}_{in}$ and the outgoing slip plane and grain boundary plane $\vec{I}_{out}$ should be as small as possible. Transmission of dislocations through the grain boundary requires rotation of the dislocation line over this angle. This motion usually will require climb, which is a diffusion limited process, and this hinders dislocation transmission. In addition, the angle between the slip direction (i.e. the direction of the Burgers vector) of the incoming ($\vec{g}_{in}$) and outgoing ($\vec{g}_{out}$) slip systems should be minimized. This criterion can be expressed as follows:

$$\vec{M} = (\vec{I}_{in} \times \vec{I}_{out}) \times (\vec{g}_{in} \times \vec{g}_{out}), \tag{2.24}$$

where $\vec{M}$ should be maximized. The Burgers vector of the dislocation on the outgoing slip plane is calculated as the one with the maximum force from the incoming dislocations acting on it.

A set of criteria were also proposed in [62] which are similar to those in [63] based on in-situ TEM observations:

(i) The outgoing slip plane is determined by minimizing the angle between the intersections of incoming ($\vec{I}_{in}$) and outgoing ($\vec{I}_{out}$) slip planes. Expressed mathematically:

$$\vec{M}' = \vec{I}_{in} \times \vec{I}_{out}\ , \tag{2.25}$$

where $\vec{M}'$ should be maximized.

(ii) The magnitude of the Burgers vector of the residual dislocation left in the grain boundary should be a minimum.

(iii) The outgoing slip system should have the maximum resolved shear stress from the piled up dislocations.

Criteria (ii) and (iii) may be contradictory with respect to the prediction of the Burgers vector of the outgoing dislocations. Based on microscopy observations criterion (ii) seems to dominate [62].

2.5 PILEUPS AND LEDGES

Physical observations, such as those discussed in the previous section, have stimulated the study of dislocation pileups, which along with grain boundary ledges, motivated the development of a gradient plasticity theory with an interfacial penalty (Chapters 3-7), as well as its experimental confirmation through nano-indentation tests (Chapter 8). Both of these features, i.e. pileups and ledges, are important for understanding: grain size strengthening and, in particular, for substantiating the Hall-Petch relation; the need of an interfacial energy-like term; and the assumption of discontinuous plastic gradients across interfaces, which are the physical mechanisms underlying the formulation of Chapter 3.

2.5.1 Dislocation pileups

The significance of interfaces within a mechanical behavior framework is most easily attested from strong experimental evidence showing that in polycrystalline bulk materials and multilayer films the strength increases when the grain boundary or interlayer spacing decreases, resulting in grain boundary and interface strengthening, respectively. This phenomenon is described by the celebrated Hall-Petch relationship, which can be written in the form [65]

$$\sigma = \sigma_i + K_{H-P} d^{-1/2}, \tag{2.26}$$

where σ is actually the yield stress, σ_i is the lattice friction stress resisting dislocation motion in the lattice, K_{H-P} is the Hall-Petch coefficient and d represents the grain size or interlayer spacing. Various microscopic expressions can be deduced for K_{H-P} depending on the prevailing lattice-interface interaction that is taking place through dislocation motion and production. In fact, it may even be possible for K_{H-P} to formally attain negative values when the grain size is reduced down to nanometer dimensions (inverse Hall-Petch relation, [66]).

A most commonly acceptable strength increasing mechanism results from the fact that all internal boundaries are obstacles to dislocation movement, since once they come upon a boundary they do not have the correct Burgers vector or slip plane to glide into the next crystal, as a result dislocations pileup there. The degree to which interfaces hinder the motion of the dislocations could be crucial for the occurrence of localized heterogeneous plastic flow, often leading to failure, since stress concentrations will develop that will eventually lead to intergranular fracture along the boundaries.

The occurence of pileups is shown in Fig. 2.9.

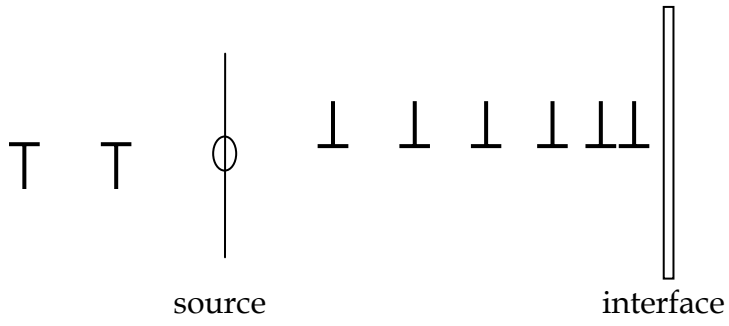

Fig. 2.9: Dislocation pile up

Since dislocations are carriers of plastic strain it can be seen that dislocation pileups may induce gradients in the plastic strain, which in conjunction with the

formation of boundary ledges may result in plastic strain gradient discontinuities across such barriers. In general, dislocations that form near internal surfaces and obstacles, where the strain is not compatible, are termed "geometrically necessary dislocations" [67], therefore the gradient of the plastic strain may be viewed as a measure of the density of such dislocations. In this connection it is pointed out that certain gradient plasticity theories [3,8] are directly based on the additivity of the densities of usual dislocations distributed in the grain interior (commonly termed "forest" or "statistical" dislocations) and the aforementioned "geometrically necessary" dislocations that are accumulated near interfaces to relax strain incompatibilties. In the sequel the dislocations that form in the grain interior will be called lattice dislocations, to distinguish them from those present in interfaces (as was done in the previous sub-section).

More details on dislocation pileups and their interaction with a grain boundary is provided in Chapter 8. In particular, the stess at which the dislocations cross the interface is computed through nano-indentation experiments; this allows for the physical substantiation and experimental verification of the model proposed in Chapter 3.

2.5.2 Grain Boundary Ledges

In connection with the assumed discontinuity of plastic strain gradient across interfaces (which is a basic premise in the model development of Chapter 3), reference is made to the formation of grain boundary ledges as shown in Fig. 2.10 [68]. Fig. 2.10(a) shows the movement of GBDs along the grain boundary plane in the direction of the arrow, while Figure 2.10(b) shows their coalescence to form a grain boundary ledge. Another way of ledge formation is shown in Figs. 2.10(c) and (d) where lattice dislocations move from grain A to grain B through the grain boundary plane; thus resulting in heterogeneous shear of the boundary, forming a ledge.

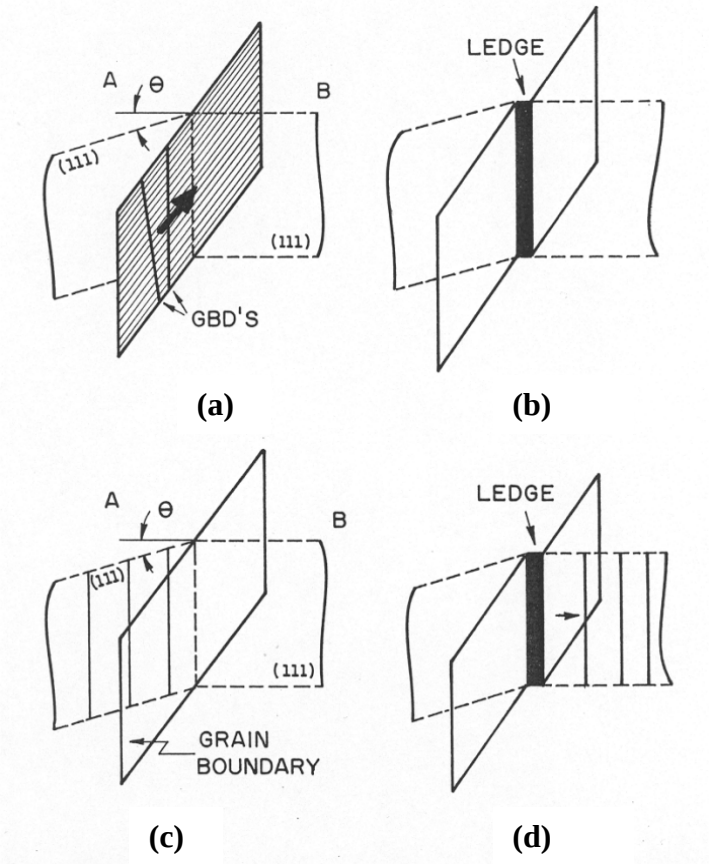

Fig. 2.10: Grain boundary ledge formation

Grain boundary ledges are an important characteristic of high angle boundaries, their density increases with the degree of misorientation and they act as very efficient dislocation sources, having an important role in inhomogeneous plastic deformation seen in Figure 2.11 [65].

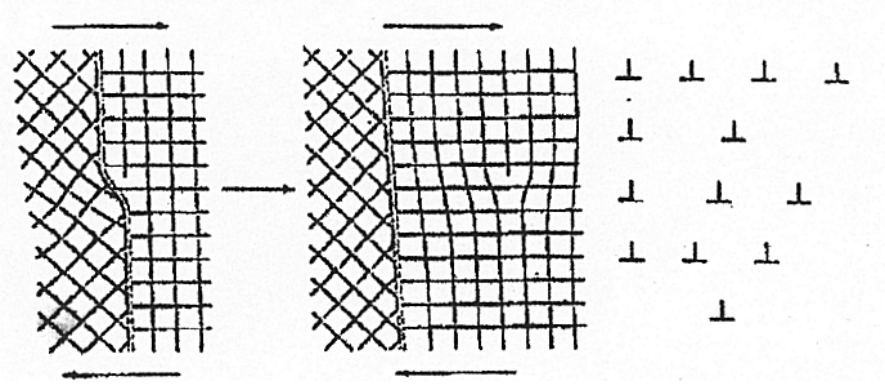

Fig. 2.11: Grain boundary ledge dislocation lodge

CHAPTER 3

GRADIENT PLASTICITY WITH AN INTERFACIAL PENALTY

The formulation that will be developed in this chapter is based on the physical arguments presented in Chapter 2. Gradient plasticity is employed in order to account for the gradients in the plastic strain, and dislocation pileups are considered by the admittance of an interfacial energy-like term (interfacial penalty). It should be emphasized that this interfacial term is substantially different from that introduced in Chapter 2, since it is induced by plastic deformation, and does not arise only from the structural differences present at internal boundaries.

3.1 DEFORMATION THEORY VERSION OF CLASSICAL PLASTICITY

The mathematical structure that is employed throughout this work is first placed in context by displaying the corresponding formulation for the deformation theory version of "classical" plasticity, with no allowance for strain-gradients. Throughout the whole of Chapter 3, the presentation is kept as simple as possible by assuming that displacements are prescribed on the boundary $\partial\Omega$ of the body, which occupies the domain Ω.

Within the deformation theory framework of classical plasticity, an energy-like functional for the domain Ω under consideration can be defined as

$$\Psi(\varepsilon_{ij}, \varepsilon_{ij}^{p}) = \int_{\Omega} U(\varepsilon_{ij}, \varepsilon_{ij}^{p}) \; d\Omega, \tag{3.1}$$

where

$$U(\varepsilon_{ij}, \varepsilon_{ij}^{p}) \equiv \frac{1}{2} L_{ijkl}(\varepsilon_{ij} - \varepsilon_{ij}^{p})(\varepsilon_{kl} - \varepsilon_{kl}^{p}) + V(\varepsilon_{ij}^{p}). \tag{3.2}$$

The quantities (ε_{ij}, ε_{ij}^{P}) denote the total strain and plastic strain, respectively; L_{ijkl} is the elastic stiffness tensor; the first term of the right hand side of (3.2) is the elastic strain energy; and the second term, involving $V(\varepsilon_{ij}^{P})$, is a "dissipation function", dual to the "plastic potential". In the present context of deformation theory, the distinction between dissipated and recoverable energy is blurred. In the sequel, it is convenient to refer to V simply as a "potential".

The problem posed then is to find the fields ($\varepsilon_{ij}, \varepsilon_{ij}^{P}$) that minimize (3.1). It should be noted that both displacement and plastic strain are continuous across interfaces and the total strain tensor ε_{ij} is related to the displacement vector u_i by the usual relationship

$$\varepsilon_{ij} = \frac{1}{2}(u_{i,j} + u_{j,i}). \tag{3.3}$$

For convenience, the following conjugate variables to the elastic and plastic strain are introduced

$$\sigma_{ij} = \frac{\partial U}{\partial \varepsilon_{ij}} = L_{ijkl}\left(\varepsilon_{kl} - \varepsilon_{kl}^{P}\right), \tag{3.4a}$$

$$s_{ij} = \frac{\partial U}{\partial \varepsilon_{ij}^{P}} = -L_{ijkl}(\varepsilon_{kl} - \varepsilon_{kl}^{P}) + \frac{\partial V}{\partial \varepsilon_{ij}^{P}} = -\sigma_{ij} + \frac{\partial V}{\partial \varepsilon_{ij}^{P}}. \tag{3.4b}$$

The quantity σ_{ij} is the usual Cauchy stress tensor and s_{ij} may be viewed as a type of "back stress". Now by setting the first variation of (3.1) equal to zero, $\delta\Psi=0$, we

obtain a degenerate form of the principle of virtual work; subsequent integration by parts gives

$$\int_{\Omega}\left[\sigma_{ij}\delta\varepsilon_{ij}+s_{ij}\delta\varepsilon_{ij}^{P}\right]\,d\Omega=0\Rightarrow\int_{\Omega}\left[-\sigma_{ij,j}\,\delta u_i+s_{ij}\,\delta\varepsilon_{ij}^{P}\right]d\Omega+\int_{S_T}\left[\sigma_{ij}n_j\,\delta u_i\right]dS=0\,, \quad (3.5)$$

which should hold true for all independent variations $\delta u_i\,,\delta\varepsilon_{ij}^{P}$. As a result, the following field equations are obtained

$$\left.\begin{aligned}\sigma_{ij,j}&=0\\ s_{ij}=0\Rightarrow\sigma_{ij}&=\frac{\partial V}{\partial\varepsilon_{ij}^{P}}\end{aligned}\right\}\ \text{in}\ \Omega\backslash\partial\Omega\,, \quad (3.6)$$

along with the boundary condition

$$u_i=u_i^{o}\ \text{on}\ \partial\Omega. \quad (3.7)$$

It should be noted that instead of prescribing the displacement, the traction could be imposed. This would require the presence of an additional surface integral in the variational functional and (3.7) would be replaced by $\sigma_{ij}n_j=t_{ij}$.

The second of equations (3.6) shows that the potential *V* provides a stress-plastic strain relation, from which plastic strain can be eliminated to yield, in conjunction with (3.4*a*), the conventional stress-total strain relation of deformation theory. The use of plastic strain as an intermediate (or internal) variable will, however, be essential for the developments to follow. It is perhaps worth noting that no requirement of continuity is made for the plastic strain. Imposition of such a requirement would compromise the existence of a plastic strain field which would minimize Ψ. It would be necessary instead to seek the infimum, which would be approached by use of sequences of continuous plastic strain fields whose limit would be the solution of (3.6) and (3.7).

3.2 VARIATIONAL FORMULATION WITH ALLOWANCE FOR STRAIN GRADIENTS

As was mentioned in the introduction the main feature of the present work is that the form of the potential "energy" functional $\Psi(\varepsilon_{ij},\varepsilon_{ij}^{P})$ is generalized to

consider the effect of internal boundaries, which are collectively denoted by Γ, and the associated with them interfacial energy-like term $\phi(\varepsilon_{ij}^{P})$. Therefore, in this section, the existence of internal boundaries, such as grain and interphase boundaries, is explicitly considered within the strain-gradient plasticity framework: an interfacial energy-like term is assigned to them and the associated jump conditions across them are provided. It is emphasized again that no calculations to date employing strain-gradient plasticity theory have incorporated in detail, within an appealing mathematical setting, jump conditions across interfaces and, hence, treated them as "surfaces of discontinuity".

This generalised expression for $\Psi(\varepsilon_{ij}, \varepsilon_{ij}^{P})$ reads

$$\Psi(\varepsilon_{ij}, \varepsilon_{ij}^{P}) = \int_{\Omega} U(\varepsilon_{ij}, \varepsilon_{ij}^{P}, \varepsilon_{ij,k}^{P})\, d\Omega + \int_{\Gamma} \phi(\varepsilon_{ij}^{P})\, d\Gamma\,; \tag{3.8}$$

again Ω and ∂Ω denote the composite domain under consideration, and its outer boundary respectively. The displacement and plastic strain, which are the primary kinematic variables of the system, are taken to be continuous throughout the whole domain Ω (even across the internal surfaces Γ) and are related through (3.3). The elastoplastic potential $U(\varepsilon_{ij}, \varepsilon_{ij}^{P}, \varepsilon_{ij,k}^{P})$ is defined similarly as in Fleck-Willis [7]

$$U(\varepsilon_{ij}, \varepsilon_{ij}^{P}, \varepsilon_{ij,k}^{P}) \equiv \frac{1}{2} L_{ijkl}(\varepsilon_{ij} - \varepsilon_{ij}^{P})(\varepsilon_{kl} - \varepsilon_{kl}^{P}) + V(\varepsilon_{ij}^{P}, \varepsilon_{ij,k}^{P})\,. \tag{3.9}$$

It can be seen that the strain-gradient comes in the plastic potential *V*. Moreover, it should be noted that both L_{ijkl} and V vary with position x. Upon plastic deformation, the fields within the composite are taken to be those which minimize the overall energy functional (3.8) over continuous plastic strain fields, and continuous total strain fields that satisfy expression (3.3); since the displacement is prescribed it follows that $u_i = u_i^{o}$ on ∂Ω. The problem then posed is to find the fields ε_{ij} (or u_i) and ε_{ij}^{p} that yield the infimum value

$$\Xi = \inf_{\varepsilon_{ij},\varepsilon_{ij}^{p}} \Psi(\varepsilon_{ij}, \varepsilon_{ij}^{p}) . \tag{3.10}$$

As in the classical case, the following conjugate variables, which express the Euler-Lagrange equations associated with the infimum problem (3.10) are defined:

$$\sigma_{ij} = \frac{\partial U}{\partial \varepsilon_{ij}} = L_{ijkl}\left(\varepsilon_{kl} - \varepsilon_{kl}^{p}\right), \tag{3.11a}$$

$$s_{ij} = \frac{\partial U}{\partial \varepsilon_{ij}^{p}} = -L_{ijkl}\left(\varepsilon_{kl} - \varepsilon_{kl}^{p}\right) + \frac{\partial V}{\partial \varepsilon_{ij}^{p}} = -\sigma_{ij} + \frac{\partial V}{\partial \varepsilon_{ij}^{p}}, \tag{3.11b}$$

$$\tau_{ijk} = \frac{\partial U}{\partial \varepsilon_{ij,k}^{p}} = \frac{\partial V}{\partial \varepsilon_{ij,k}^{p}} . \tag{3.11c}$$

It should be noted that the two first conjugate variable relations are the same as those used in the classical case, but use of the gradient of ε_{ij}^{p} as an additional independent variable results in the definition (3.11*c*) of the higher-order stress (or hyperstress) τ_{ijk}. The requirement that the functional Ψ is minimized implies the principle of virtual work, that the first variation of (3.8) has to be zero for all allowed variations $\delta\varepsilon_{ij}$ and $\delta\varepsilon_{ij}^{p}$; hence

$$\int_{\Omega} (\sigma_{ij}\delta\varepsilon_{ij} + s_{ij}\delta\varepsilon_{ij}^{P} + \tau_{ijk}\delta\varepsilon_{ij,k}^{P})\, d\Omega + \int_{\Gamma} \phi'(\varepsilon_{ij}^{P})\, d\Gamma = 0 . \tag{3.12}$$

It follows that integrating by parts, allowing for admissible discontinuities across interfaces gives

$$\begin{aligned} \int_{\Omega} \left\{ -\sigma_{ij,j}\delta u_i + (s_{ij} - \tau_{ijk,k})\,\delta\varepsilon_{ij}^{P} \right\} d\Omega + \int_{\partial\Omega} \left\{ \sigma_{ij} n_j \delta u_i + \tau_{ijk} n_k \delta\varepsilon_{ij}^{P} \right\} dS \\ + \int_{\partial\Gamma} \left\{ -[\sigma_{ij} n_j]\delta u_i + (\phi'(\varepsilon_{ij}^{P}) - [\tau_{ijk} n_k])\delta\varepsilon_{ij}^{P} \right\} d\Gamma = 0, \end{aligned} \tag{3.13}$$

for all allowed variations δu_i and $\delta\varepsilon_{ij}^{p}$. This implies the field equations

$$\left.\begin{aligned} \sigma_{ij,j} &= 0 \\ s_{ij} - \tau_{ijk,k} &= 0 \end{aligned}\right\} \text{ in } \Omega\backslash\Gamma, \tag{3.14}$$

the "natural" boundary condition

$$\tau_{ijk,k} n_k = 0 \text{ on } \partial\Omega\,, \tag{3.15}$$

and the jump across interfaces conditions

$$\left.\begin{aligned} [\sigma_{ij} n_j] &= 0 \\ [\tau_{ijk} n_k] &= \phi(\varepsilon_{ij}^p) \end{aligned}\right\} \text{across } \Gamma. \tag{3.16}$$

It can be seen that the jump condition in the hyperstress is solely due to the admission of the interfacial energy term in the overall energy functional; the usual Cauchy stress on the other hand suffers no discontinuity across internal surfaces. In (3.13), (3.16) and equations to follow, [f] denotes the jump f_2-f_1 across a surface Γ, where the normal n_i points in the direction from "side 2" to "side 1". If the plastic strain, instead of the displacement was prescribed the higher-order stress in (3.15), would be replaced by the usual stress. Imposing other boundary conditions on the external surface, such as the nominal stress, would require the addition of surface integrals, over $\partial\Omega$, in the overall energy functional Ψ (see [7]). Finally, it should be noted that setting ϕ=0, or simply disregarding its existence, results in the original Fleck-Willis [7] formulation, and the second condition in (3.16) reduces to the requirement of continuity of higher-order tractions.

3.3 EFFECTIVE RESPONSE

Taking the displacement, which is prescribed on the outer boundary to vary smoothly (relative to the macroscale) as the scale of the microstructure reduces, allow (3.10) to be asymptotically replaced by the homogenized problem

$$\Xi = \inf_{\bar{\varepsilon}_{ij}, \bar{\varepsilon}_{ij}^P} \int_\Omega U^{eff}(\bar{\varepsilon}_{ij}, \bar{\varepsilon}_{ij}^P)\, dx\,, \tag{3.17}$$

where U^{eff} is a local average defined over a "representative volume element" D, the interfaces in which are denoted as Γ_D; hence

$$U^{eff}(\bar{\varepsilon}_{ij},\bar{\varepsilon}_{ij}^{p}) \equiv \inf_{\bar{\varepsilon}_{ij},\bar{\varepsilon}_{ij}^{p}} \left\{ \frac{1}{|D|}\left[\int_D U(\varepsilon_{ij},\varepsilon_{ij}^{p},\varepsilon_{ij,k}^{p})\,dx + \int_{\Gamma_D} \phi(\varepsilon_{ij}^{p})\,d\Gamma \right] \right\}$$

$$= \inf_{\bar{\varepsilon}_{ij},\bar{\varepsilon}_{ij}^{p}} \left\{ \frac{1}{|D|}\left[\int_D \left(\frac{1}{2} L_{ijkl}(\varepsilon_{ij}-\varepsilon_{ij}^{p})(\varepsilon_{kl}-\varepsilon_{kl}^{p}) + V(\varepsilon_{ij}^{p},\varepsilon_{ij,k}^{p}) \right) dx + \int_{\Gamma_D} \phi(\varepsilon_{ij}^{p})\,d\Gamma \right] \right\}. \quad (3.18)$$

It should be noted that the displacement is not prescribed on ∂D. Instead it is now required to impose conditions on the average total and plastic strain (in addition to (3.3)), over which the infimum is computed, the following relations are therefore defined

$$\left\langle \varepsilon_{ij} \right\rangle \equiv \frac{1}{|D|}\int_D \varepsilon_{ij}\,dx = \bar{\varepsilon}_{ij}\,, \quad (3.19)$$

$$\left\langle \varepsilon_{ij}^{p} \right\rangle \equiv \frac{1}{|D|}\int_D \varepsilon_{ij}^{p}\,dx = \bar{\varepsilon}_{ij}^{p}\,. \quad (3.20)$$

Working out the infimum of (3.17) results in an expression similar to (3.13), which however contains the additional constants s_{ij}^{*} and $\bar{\sigma}_{ij}$ that play the role of Lagrange multipliers, and result from the fact that the solution now must be compatible with the constraints imposed by (3.19) and (3.20); in other words the following equation is deduced:

$$\int_\Omega \left\{ -\sigma_{ij,j}\delta u_i + (s_{ij}+s_{ij}^{*}-\tau_{ijk,k})\,\delta\varepsilon_{ij}^{P} \right\} d\Omega + \int_{\partial\Omega} \left\{ (\sigma_{ij}-\bar{\sigma}_{ij})n_j\delta u_i + \tau_{ijk}n_k\delta\varepsilon_{ij}^{P} \right\} dS$$
$$+ \int_\Gamma \left\{ -[\sigma_{ij}n_j]\delta u_i + (\phi'(\varepsilon_{ij}^{P}) - [\tau_{ijk}n_k])\delta\varepsilon_{ij}^{P} \right\} d\Gamma = 0, \quad (3.21)$$

which provides the conditions

$$\left.\begin{aligned} \sigma_{ij,j} &= 0 \\ s_{ij} - \tau_{ijk,k} &= s_{ij}^{*} \end{aligned}\right\} \text{in } D\backslash\Gamma, \quad (3.22)$$

$$\left.\begin{aligned} (\sigma_{ij}-\bar{\sigma}_{ij})n_j &= 0 \\ \tau_{ijk,k}n_k &= 0 \text{ on } \partial\Omega \end{aligned}\right\} \text{on } \partial D, \quad (3.23)$$

$$\left.\begin{aligned} [\sigma_{ij}n_j] &= 0 \\ [\tau_{ijk}n_k] &= \phi(\varepsilon_{ij}^{p}) \end{aligned}\right\} \text{across } \Gamma_D. \quad (3.24)$$

Consideration of the conditions $(3.22)_1$, $(3.22)_2$, and $(3.22)_3$, which contain σ_{ij} concludes that the Lagrange multiplier $\bar{\sigma}_{ij}$ is the mean stress over D. Similarly s^*_{ij} can be viewed as a mean "back stress"; the infimum of (3.17) with respect to $\bar{\varepsilon}^p_{ij}$ is achieved when $s^*_{ij} = 0$. In particular, consideration of the variation of U^{eff} with respect to small changes in $\bar{\varepsilon}_{ij}$ and $\bar{\varepsilon}^p_{ij}$ gives the effective constitutive relations

$$\bar{\sigma}_{ij} = \frac{\partial U^{eff}}{\partial \bar{\varepsilon}_{ij}}, \tag{3.25}$$

$$s^*_{ij} = \frac{\partial U^{eff}}{\partial \bar{\varepsilon}^p_{ij}}. \tag{3.26}$$

3.4 BOUNDS

In order to simplify the bounding formulation, all composite constituents are taken to have the same elastic tensor; hence L_{ijkl} describes the elastic response of the whole system under consideration. Expression (3.18), can therefore be written as

$$U^{eff}(\bar{\varepsilon}_{ij}, \bar{\varepsilon}^P_{ij}) \equiv \frac{1}{2} L_{ijkl}(\bar{\varepsilon}_{ij} - \bar{\varepsilon}^P_{ij})(\bar{\varepsilon}_{kl} - \bar{\varepsilon}^P_{kl}) + V^{eff}(\bar{\varepsilon}^P_{ij}). \tag{3.27}$$

Since $\bar{\varepsilon}^p_{ij}$ is a constant, it follows that its gradient is zero and hence (3.27) can also be used to describe the effective response of a composite that conforms to classical plasticity, such as that in Section 3.1. Since expression (3.27) defines the effective plastic potential as a function of the mean plastic strain, it should be proven that V is in fact independent of mean total strain. First, a minimization on the first term of (3.18), over ε_{ij} is performed, with fixed ε^p_{ij} to give

$$\inf_{\varepsilon_{ij}} \frac{1}{|D|} \int_D \frac{1}{2} L_{ijkl}(\varepsilon_{ij} - \varepsilon^p_{ij})(\varepsilon_{kl} - \varepsilon^p_{kl})\, dx = \inf_{\varepsilon^1_{ij}} \frac{1}{|D|} \int_D \frac{1}{2} L_{ijkl}(\bar{\varepsilon}_{ij} + \varepsilon^1_{ij} - \varepsilon^P_{ij})(\bar{\varepsilon}_{kl} + \varepsilon^1_{kl} - \varepsilon^P_{kl})\, dx, \tag{3.28}$$

where ε_{ij}^{1} is any strain field with mean value zero, over *D*; exploiting this fact allows the right hand side of (3.28) to be expanded as

$$\inf_{\varepsilon_{ij}^{1}} \frac{1}{|D|}\int_D \frac{1}{2} L_{ijkl}[(\bar{\varepsilon}_{ij}-\bar{\varepsilon}_{ij}^{P})+(\varepsilon_{ij}^{1}+\bar{\varepsilon}_{ij}^{P}-\varepsilon_{ij}^{P})][(\bar{\varepsilon}_{kl}-\bar{\varepsilon}_{kl}^{P})+(\varepsilon_{kl}^{1}+\bar{\varepsilon}_{kl}^{P}-\varepsilon_{kl}^{P})]dx$$

$$=\frac{1}{2}L_{ijkl}(\bar{\varepsilon}_{ij}-\bar{\varepsilon}_{ij}^{P})(\bar{\varepsilon}_{kl}-\bar{\varepsilon}_{kl}^{P})+\inf_{\varepsilon_{ij}^{1}}\frac{1}{|D|}\int_D \frac{1}{2}L_{ijkl}(\varepsilon_{ij}^{1}+\bar{\varepsilon}_{ij}^{P}-\varepsilon_{ij}^{P})(\varepsilon_{kl}^{1}+\bar{\varepsilon}_{ij}^{P}-\varepsilon_{kl}^{P})\,dx. \quad (3.29)$$

Combination of (3.29) with (3.27) provides

$$V^{eff}(\bar{\varepsilon}_{ij}^{P})=\inf_{\varepsilon_{ij}^{1},\varepsilon_{ij}^{P}}\left\{\frac{1}{|D|}\left[\int_D\left(\frac{1}{2}L_{ijkl}(\varepsilon_{ij}^{1}+\bar{\varepsilon}_{ij}^{P}-\varepsilon_{ij}^{P})(\varepsilon_{kl}^{1}+\bar{\varepsilon}_{kl}^{P}-\varepsilon_{kl}^{P})+V(\varepsilon_{ij}^{P},\varepsilon_{ij,k}^{P})\right)dx+\int_\Gamma \phi(\varepsilon_{ij}^{P})\right]\right\}. \quad (3.30)$$

It follows that the infimum over ε_{ij}^{1} in (3.30) makes a contribution to V^{eff}, which depends on $\bar{\varepsilon}_{ij}^{p}$, but not on $\bar{\varepsilon}_{ij}$.

3.4.1 Elementary upper and lower bounds

Expression (3.18) can be manipulated into giving an upper bound by allowing the admissible fields ε_{ij} and ε_{ij}^{p} of the right hand side to be defined as $\bar{\varepsilon}_{ij}$ and $\bar{\varepsilon}_{ij}^{p}$. Hence,

$$U^{eff}(\bar{\varepsilon}_{ij},\bar{\varepsilon}_{ij}^{P})\le\frac{1}{|D|}\left\{\int_D U(\bar{\varepsilon}_{ij},\bar{\varepsilon}_{ij}^{P},0)\,dx+\int_{\Gamma_D}\phi(\bar{\varepsilon}_{ij}^{P})\,d\Gamma\right\}. \quad (3.31)$$

It follows that the corresponding bound for V^{eff}, when the elastic constants are the same everywhere is

$$V^{eff}(\bar{\varepsilon}_{ij}^{P})\le V_V(\bar{\varepsilon}_{ij}^{P})\equiv\frac{1}{|D|}\left\{\int_D V(\bar{\varepsilon}_{ij}^{P},0)\,dx+\int_{\Gamma_D}\phi(\bar{\varepsilon}_{ij}^{P})\,d\Gamma\right\}. \quad (3.32)$$

It can be seen that in the absence of the interface term, the aforementioned bound is scale independent. Hence, if interfaces are not accounted for explicitly, through an energy penalty ϕ, a definite upper limit, which is independent of the scale of the microstructure is obtained [7,30,31]. According to the present formulation, however, the upper bound for the plastic response increases

linearly with the ratio of surface area to volume, and therefore the resulting size effects will not bounded. It should be noted that (3.32) is analogous to the Voigt upper bound of classical elasticity.

A lower bound, of Reuss type can also be formulated, by considering (3.27) in combination with the Fenchel inequality

$$U^*(\sigma_{ij}, s_{ij}, \tau_{ijk}) \geq \sigma_{ij}\varepsilon_{ij} + s_{ij}\varepsilon_{ij}^p + \tau_{ijk}\varepsilon_{ij.k}^p - U(\varepsilon_{ij}, \varepsilon_{ij}^P, \varepsilon_{ij,k}^P), \qquad (3.33)$$

where U^* is the convex dual of U.

Allowing L_{ijkl} to be constant and setting the stress and "back stress" equal to their mean values, in addition to letting the higher-order stress be zero provides

$$U^{eff}(\overline{\varepsilon}_{ij}, \overline{\varepsilon}_{ij}^p) \geq \inf_{\overline{\varepsilon}_{ij}^p} \left\{ \overline{\sigma}_{ij}\overline{\varepsilon}_{ij} + \overline{s}_{ij}\overline{\varepsilon}_{ij}^p - \frac{1}{2L_{ijkl}}\overline{\sigma}_{ij}\overline{\sigma}_{kl} - \frac{1}{|D|}\left[\int_D V^*(\overline{\sigma}_{ij} + \overline{s}_{ij}, 0)\, dx - \int_{\Gamma_D} \phi(\varepsilon_{ij}^P)\, d\Gamma \right] \right\}, \qquad (3.34)$$

for any $\overline{\sigma}_{ij}$ and $\overline{s}_{ij}$; V^* is the convex dual of V. The infimum in (3.34) is evaluated over fields that satisfy $\varepsilon_{ij}^p \equiv \overline{\varepsilon}_{ij}^p$, hence the only thing that needs calculating is the interfacial penalty term. Assuming that $\phi(\varepsilon_{ij}^p) \geq \phi(0) = 0$, provides that $\inf_{\varepsilon_{ij}^p} \int_{\Gamma_D} \phi(\varepsilon_{ij}^P)\, d\Gamma = 0$. Furthermore optimizing (3.34) with respect to $\overline{\sigma}_{ij}$ and $\overline{s}_{ij}$ provides

$$V^{eff}(\overline{\varepsilon}_{ij}^p) \geq V_R(\overline{\varepsilon}_{ij}^p) \equiv \sup_{\overline{s}_{ij}} \left\{ \overline{s}_{ij}\overline{\varepsilon}_{ij}^p - \frac{1}{|D|}\int_D V^*(\overline{s}_{ij}, 0)\, dx \right\}. \qquad (3.35)$$

As it can be seen this lower bound is scale independent; the same result would have been obtained if the interfacial penalty was neglected.

3.4.2 Refined upper bound

In this section a more flexible method for obtaining an upper bound for the effective response of the composite under consideration is developed. According

to this technique the effective properties of a medium which is characterized by a nonlinear response (i.e. its potentials V and ϕ are nonlinear) are bounded through comparison with a medium whose response is linear, but has the same microgeometry and elastic stiffness tensor as the actual composite. This linear medium is referred to as "comparison medium", and its potentials V_c and ϕ_c are taken to be simple quadratic functions so that an exact or good approximation of its effective response can be computed; it follows that this comparison composite need not have direct physical meaning.

Performing mathematical manipulations on definition (3.27) the upper bound for U^{eff} is formulated as follows:

$$\begin{aligned} U^{eff}(\bar{\varepsilon}_{ij},\bar{\varepsilon}^P_{ij}) = \inf_{\bar{\varepsilon}_{ij},\bar{\varepsilon}^P_{ij}} \Bigg\{ \frac{1}{|D|}\Bigg[\int_D \Bigg(\frac{1}{2} L_{ijkl}(\varepsilon_{ij}-\varepsilon^P_{ij})(\varepsilon_{kl}-\varepsilon^P_{kl}) + V_c^{eff}(\varepsilon^P_{ij}) \Bigg) dx \\ + \int_D [V(\varepsilon^P_{ij},\varepsilon^P_{ij,k}) - V_c(\varepsilon^P_{ij},\varepsilon^P_{ij,k})]\, dx \\ + \int_{\Gamma_D} \phi_c(\varepsilon^P_{ij})\, d\Gamma + \int_{\Gamma_D} [\phi(\varepsilon^P_{ij}) - \phi_c(\varepsilon^P_{ij})]\, d\Gamma \Bigg] \Bigg\} \\ \le U_c^{eff}(\bar{\varepsilon}_{ij},\bar{\varepsilon}^P_{ij}) + \frac{1}{|D|}\Bigg[\int_D \max(V - V_c)\, dx + \int_{\Gamma_D} \max(\phi - \phi_c)\, d\Gamma \Bigg], \end{aligned} \quad (3.36)$$

where U_c^{eff} is defined by (3.27), but with V^{eff} replaced by V_c^{eff}. It should be mentioned that the maxima in (3.36) are finite when the arguments of V_c and ϕ_c grow no faster than quadratically. It follows that the corresponding upper bound for the plastic potential is

$$V^{eff}(\bar{\varepsilon}^P_{ij}) \le V_c^{eff}(\bar{\varepsilon}^P_{ij}) + \frac{1}{|D|}\Bigg[\int_D \max(V - V_c)\, dx + \int_{\Gamma_D} \max(\phi - \phi_c)\, d\Gamma \Bigg]. \quad (3.37)$$

To obtain the best possible upper bound, (3.36) and (3.37) are minimized with respect to the material parameters that come into play in the comparison potentials, for given $\bar{\varepsilon}^p_{ij}$; hence a bound of the type first introduced by Ponte Castaneda [28] is generated.

3.4.3 Specialization to 1 Dimension

Chapters 4 and 5 are concerned with one-dimensional examples, such as a bar under tension or compression, or a laminate under simple shear. In either case, there is just one relevant component of stress, displacement, total strain, plastic strain, and higher-order stress. It is appropriate therefore to drop all suffixes, and let x denote the coordinate in which there is variation. The partial differential equations of Section 3.2 reduce to ordinary differential equations, derivable from the one-dimensional realization of the variational principle (3.10). Likewise, the variational characterization (3.18) of U^{eff} becomes, explicitly,

$$U^{eff}(\overline{\varepsilon}_{ij},\overline{\varepsilon}^{P}_{ij}) \equiv \inf_{\varepsilon,\varepsilon^{p}} \left\{ \frac{1}{|D|}\int_{D}\left(\frac{1}{2}L(\varepsilon-\varepsilon^{p})^{2}+V(\varepsilon^{P},\varepsilon^{P}_{,x})\right)dx+\sum_{x\in\Gamma_{D}}\phi(\varepsilon^{p})\right\}. \quad (3.38)$$

The infimum with respect to the total strain is obtained when $L(\varepsilon-\varepsilon^{p})=\overline{\sigma}=\text{constant} \Rightarrow \varepsilon-\varepsilon^{p}=L^{-1}\overline{\sigma}$; averaging over x provides

$$\overline{\varepsilon}-\overline{\varepsilon}^{p}=\left(\frac{1}{|D|}\int_{D}L^{-1}dx\right)^{-1}\overline{\sigma};\left(\frac{1}{|D|}\int_{D}L^{-1}dx\right)^{-1}\equiv L_{R}, \quad (3.39)$$

where L_R is known as the Reuss average. Hence, the one dimensional counterpart of (3.27) is

$$U^{eff}(\overline{\varepsilon}\ ,\overline{\varepsilon}^{P})\equiv\frac{1}{2}L_{R}(\varepsilon-\varepsilon^{p})^{2}+V^{eff}(\overline{\varepsilon}^{P}), \quad (3.40)$$

where $V^{eff}(\overline{\varepsilon}^{P})$ is the one-dimensional counterpart of (3.30) and is given by

$$V^{eff}(\overline{\varepsilon}^{P})=\inf_{\varepsilon^{P}}\left\{\frac{1}{|D|}\left[\int_{D}V(\varepsilon^{p},\varepsilon^{p}_{,x})dx+\sum_{x\in\Gamma_{D}}\phi(\varepsilon^{p})\right]\right\}. \quad (3.41)$$

IT is essential to emphasize that (3.41) can be used even if the elastic constants differ within the domain under consideration, while (3.30), which is valid for higher dimensions can be used only if the elastic constants are the same throughout.

CHAPTER 4

EXACT FORMULATION

The gradient formulation of the previous chapter is first applied to one dimensional examples, in which interfaces are distributed in a periodic manner. The simplification of the mathematics allows the new features of the proposed formulation to be clearly demonstrated, since in addition to the bounds that were previously developed, it is possible to obtain exact analytical solutions for some one-dimensional problems; something not possible for higher dimensions (as will be demonstrated in Chapter 7).

To fix ideas for the physical interpretation of the one-dimensional situation, a uniformly stressed, two-phase, bi-crystal (Fig. 4.1), is considered. The domain Ω is divided in two regions; subscripts 1 and 2 shall be used to denote phases 1 and 2 respectively. According to previous discussions the internal surface Γ, which separates the two phases can be thought of as an interphase interface; it is taken to be situated at x=0. The lower domain, Ω_1, is held fixed such that the displacement vanishes there, i.e. $u_1(-L_1)=0$. The load is applied on the upper domain, Ω_2, which is uniformly stressed such that the boundary displacement is given by the relation $u(L_2)=(L_1+L_2)\,\bar{\varepsilon}$, where $\bar{\varepsilon}$ denotes the average strain of the system. It should be noted that this bicrystal can be thought of as the unit cell of a polycrystal. In accordance with the classical-type boundary conditions, the higher-order traction

vanishes at both boundaries (x=±$L_{1,2}$). Finally, as was mentioned in the previous chapter both the displacement and plastic strain are assumed to be continuous across Γ (i.e. at x=0); the same holds true for the stress σ as suggested by $(3.16)_1$, while τ undergoes a jump at x=±0 equal to $\phi'(\varepsilon^P)$. In summary, we have the following boundary and interfacial conditions at x=0

$$u_1(-L_1)=0; u_2(L_2)=(L_1+L_2)\,\bar{\varepsilon}; \tau_1(-L_1)=0; \tau_2(L_2)=0$$

$$u_1(0)=u_2(0); \varepsilon_1^p(0)=\varepsilon_2^p(0); \sigma_1(0)=\sigma_2(0); [\tau]=\tau_2(0^+)-\tau_1(0^-)=\phi'\big|_{x=0}, \quad (4.1)$$

in combination with the field equations

$$\sigma_{i,x}=0 \;\; ; \;\; \tau_{i,x}=s_i, \quad (4.2)$$

the first of which is satisfied by taking $\sigma=\bar{\sigma}=$ constant.

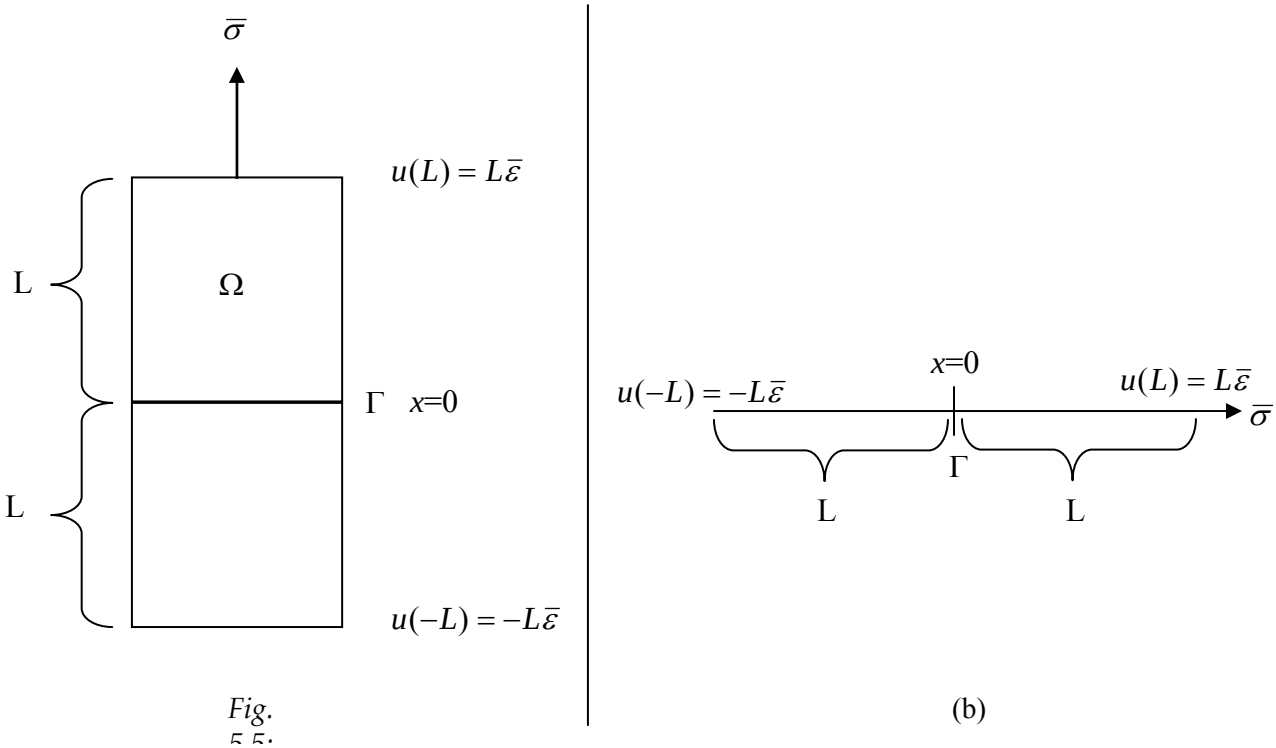

Fig. 4.1: a) physical and b) mathematical representation of the one-*dimensional model under consideration*

In order to proceed further towards the solution of the problem the constitutive relations given in (3.14) need to be employed by specifying a specific form for the gradient-dependent plastic potential $V(\varepsilon^P, \varepsilon^P_{,x})$.

4.1 LINEAR GRADIENT-DEPENDENT PLASTIC POTENTIAL

The simplest model is to assume that the material interior has a linear response and, thus, V is taken to be a quadratic function of both ε^P and $\varepsilon^P_{,x}$

$$V(\varepsilon^P, \varepsilon^P_{,x}) = \frac{1}{2}\beta_i[(\varepsilon^P)^2 + \ell_i^2(\varepsilon^P_{,x})^2]. \tag{4.3}$$

It can be seen that this form of V leads to the classical model of linear hardening (with yield stress equal to zero) in the case that the gradient term, which contains the internal length ℓ, is neglected ($\ell \equiv 0$). Moreover, the strain-gradient contribution to hardening is taken to be similar in form with that of usual strain hardening. In fact, the coefficient β measures the effect of "statistically distributed" or "forest" dislocations, while the internal length parameter $\beta\ell^2$ measures the effect of "geometrically necessary" dislocations. This can easily be concluded from the fact that ε^P and $\varepsilon^P_{,x}$ relate directly to the density of the "statistically distributed" or "geometrically necessary" dislocations, respectively. Thus, (4.3) suggests that both types of dislocation densities contribute in a similar fashion to the overall strain hardening.

Now the interfacial energy term needs to be defined. It should be noted that the precise form for ϕ should be deduced from physical arguments and by reference to microscopic models concerning the structure of the interface, and its obstacle strength during plastic flow, including the pertinent dislocation arrangement there, as suggested in Chapter 2. Below, two different models for the interfacial energy term ϕ are considered and related solutions of the corresponding one-dimensional boundary value problems are presented.

4.1.1 Linear interfacial response

In the first case considered, the interface is taken to behave similarly as the material interior. In other words, it is taken to harden analogously to the plastic strain there and, thus, the interfacial energy-like term is taken to be a quadratic function of ε^P on the interface, i.e.

$$\phi \equiv \phi(\varepsilon_0^p) = \frac{1}{2}\alpha(\varepsilon_0^p)^2 \Rightarrow [\tau] = \phi'(\varepsilon_0^p) = \alpha\varepsilon_0^p, \tag{4.4}$$

where $\varepsilon_0^P = \varepsilon^P(0)$ denotes the plastic strain on the interface and the coefficient α is a material constant. Hence the governing differential equation for this material is found by substituting (4.3) in $(4.2)_2$

$$\beta_i(\ell_i^2\varepsilon_{,xx} - \varepsilon_i^p) = -\bar{\sigma} \Rightarrow \varepsilon_i^p = A_i e^{x/\ell_i} + B_i e^{-x/\ell_i} + \frac{\bar{\sigma}}{\beta_i}, \quad \text{where } i\text{=1,2.} \tag{4.5}$$

The constants of integration, A_i and B_i, are found by direct application of the conditions $(4.1)_{3,4,6,8}$. Averaging the resulting plastic strain response provides the mean stress-plastic strain relation

$$\bar{\sigma} = \frac{\beta_1\beta_2(L_1+L_2)\left(\alpha+\beta_1\ell_1\tanh\left(\frac{L_1}{\ell_1}\right)+\beta_2\ell_2\tanh\left(\frac{L_2}{\ell_2}\right)\right)}{\alpha(\beta_1L_2+\beta_2L_1)+\ell_1\tanh\left(\frac{L_1}{\ell_1}\right)(\beta_1\beta_2L_1+\beta_1^2L_2-(\beta_1-\beta_2)^2\ell_2\tanh\left(\frac{L_2}{\ell_2}\right)-\alpha\beta_2)+(\beta_1\beta_2L_2+\beta_2^2L_1-\alpha\beta_1)\ell_2\tanh\left(\frac{L_2}{\ell_2}\right)}\dot{\bar{\varepsilon}}^p. \tag{4.6}$$

Allowing the material parameters to have the values a=2, $\beta_1 = 20$, $\beta_2 = 60$, $\ell_1 = 1$, $\ell_2 = 1.5$, the size effects in Fig. 4.2 are obtained. The ratio L_2/L_1 is kept constant to conserve the volume fractions; in this case L_2/L_1=1.5. It should be noted that from a physical point of view the specimen size must be greater than the internal length, in order for the gradient term to play a significant role in the overall response of the material.

It can be seen from Fig. 4.2 that as the specimen size decreases the required stress for continuous plastic deformation increases, implying thus a Hall-Petch type of scale dependence.

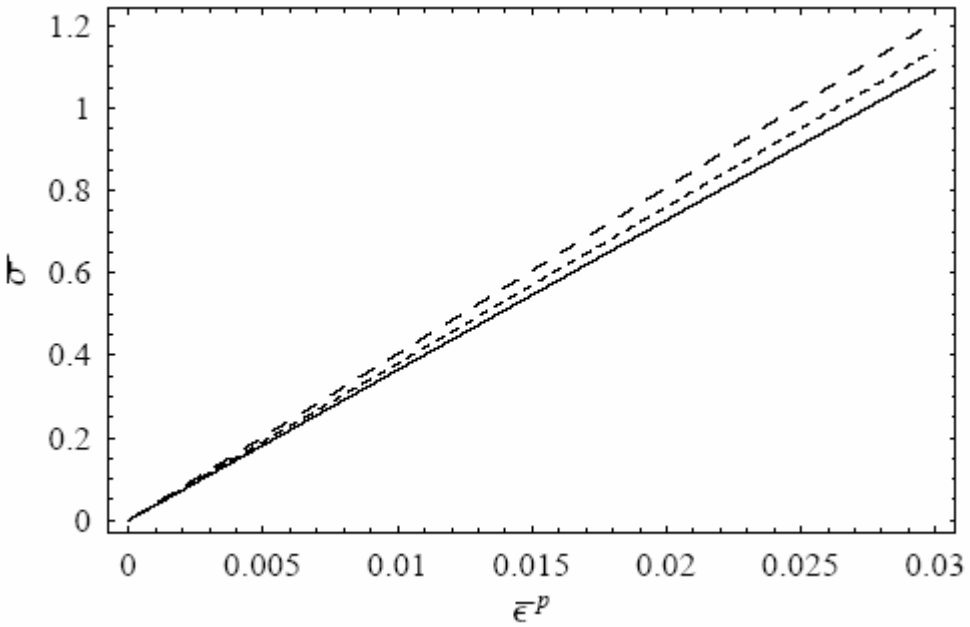

Fig. 4.2: Scale effect for linear interfacial response

4.1.2 Non-linear interfacial response

For this case, the interface is taken to be stiff and, therefore, it does not deform plastically until a critical value of the applied stress ($\bar{\sigma}_c$) is reached. After this critical stress is reached the grain boundary deforms in a "perfectly plastic" fashion, independently of both the interfacial plastic strain and the continuing hardening of the interior. It can thus be said that, in general, the interface does not yield with the rest of the material, but follows its own yield behavior. To describe this behavior mathematically, the "interfacial energy" is defined as

$$\phi \equiv \phi(\varepsilon_0^P) = \gamma \left| \varepsilon_0^P \right|. \tag{4.7}$$

It can be readily seen that this form of ϕ is not continuously differentiable. In fact, insertion of this expression into the jump condition $(4.1)_8$ results in the following two cases for the jump $[\tau]$ in the higher-order traction

$$[\tau] = \Phi'(\varepsilon^p) : \begin{cases} < \gamma, \text{ for } \varepsilon_0^p \equiv \varepsilon^p(0) = 0, \\ = \gamma, \text{ for } \varepsilon_0^p \equiv \varepsilon^p(0) > 0. \end{cases} \tag{4.8}$$

Physically, this says that as long as the interfaces are impermeable to dislocations such that the plastic strain remains zero there, the jump in the higher-order traction, $[\tau] = \tau_2(0^+) - \tau_1(0^-)$, is undetermined but lower than a critical value γ. The constant γ is a material parameter related to dislocation pileups at the interface, and their ability to cross it once a critical stress is applied. [In fact, it will be shown below that this critical value of γ is associated with a critical value of the applied stress $\bar{\sigma}_c$.] When the jump in τ reaches the critical value of γ the interface begins to deform plastically (i.e. the plastic strain there differs from zero). It then continues to deform (as long as $\bar{\sigma} > \bar{\sigma}_c$) in a "perfectly" plastic mode (in the sense that the condition $|[\tau]| = \gamma$ always holds true), such that plastic strain accumulates on both the interface and the interior, through dislocation motion. Therefore, $\bar{\sigma}_c$ can be viewed as the "interfacial yield" stress and (4.8) as the interfacial yield condition.

The relevant calculations to obtain the overall stress-strain response are similar to those in the previous subsection, but now the two cases (prior to and after interfacial yielding) are considered separately as follows.

Since V is kept the same the governing differential equation (4.5) is the same as before, but now the constants of integration are different for the pre- and post-yield cases, due to the interfacial jump condition. Prior to interfacial yield, the constants of integration in the plastic strain are solved by consideration of $(4.1)_{3,4}$, in conjunction with the fact that the interface hasn't yielded, i.e. $\varepsilon_1^p(0) = 0, \varepsilon_2^p(0) = 0$, while after interfacial yield, consideration of $(4.1)_{3,4,6}$ and $(4.8)_2$, along with subsequent averaging provides the stress-plastic strain response as

$$\bar{\sigma}=\frac{\beta_1\beta_2(L_1+L_2)}{\beta_1(L_2-\ell_2\tanh(L_2/\ell_2))+\beta_2(L_1-\ell_1\tanh(L_1/\ell_1))}\bar{\varepsilon}^p, \qquad \text{when } \bar{\varepsilon}^p \le \varepsilon_c^p$$

$$=\frac{\beta_1\beta_2\left((\gamma+(L_1+L_2)\beta_1\bar{\varepsilon}^p)\ell_1\cosh\left(\frac{L_2}{\ell_2}\right)\sinh\left(\frac{L_1}{\ell_1}\right)+(\gamma+(L_1+L_2)\beta_2\bar{\varepsilon}^p)\ell_2\cosh\left(\frac{L_1}{\ell_1}\right)\sinh\left(\frac{L_2}{\ell_2}\right)\right)}{(\beta_1L_2+\beta_2L_1)\left(\beta_1\ell_1\cosh\left(\frac{L_2}{\ell_2}\right)\sinh\left(\frac{L_1}{\ell_1}\right)+\beta_2\ell_2\cosh\left(\frac{L_1}{\ell_1}\right)\sinh\left(\frac{L_2}{\ell_2}\right)\right)-\ell_1\ell_2(\beta_1-\beta_2)^2\sinh\left(\frac{L_1}{\ell_1}\right)\sinh\left(\frac{L_2}{\ell_2}\right)},$$

$$\text{when } \bar{\varepsilon}^p \ge \varepsilon_c^p \quad (4.9)$$

where

$$\varepsilon_c^p=\frac{\gamma\cosh(L_1/\ell_1)\cosh(L_2/\ell_2)\left[\beta_1L_2(1-\tanh(L_2/\ell_2))+\beta_2L_1(1-\tanh(L_1/\ell_1))\right]}{\beta_1\beta_2(L_1+L_2)\left[\ell_1\sinh(L_1/\ell_1)\cosh(L_2/\ell_2)+\ell_2\sinh(L_2/\ell_2)\cosh(L_1/\ell_1)\right]}\ . \quad (4.10)$$

The critical stress at which the interface allows dislocation motion across it, i.e. the "interfacial yield" stress is found by solving the pre- and post- yield expressions in (4.9) for plastic strain, and then equating them to find

$$\bar{\sigma}_c=\frac{\gamma}{\ell_1\tanh(L_1/\ell_1)+\ell_2\tanh(L_2/\ell_2)}\ . \quad (4.11)$$

Allowing for the same material parameters as in the previous case, and letting the interface parameter γ=2 provides Fig. 4.3.

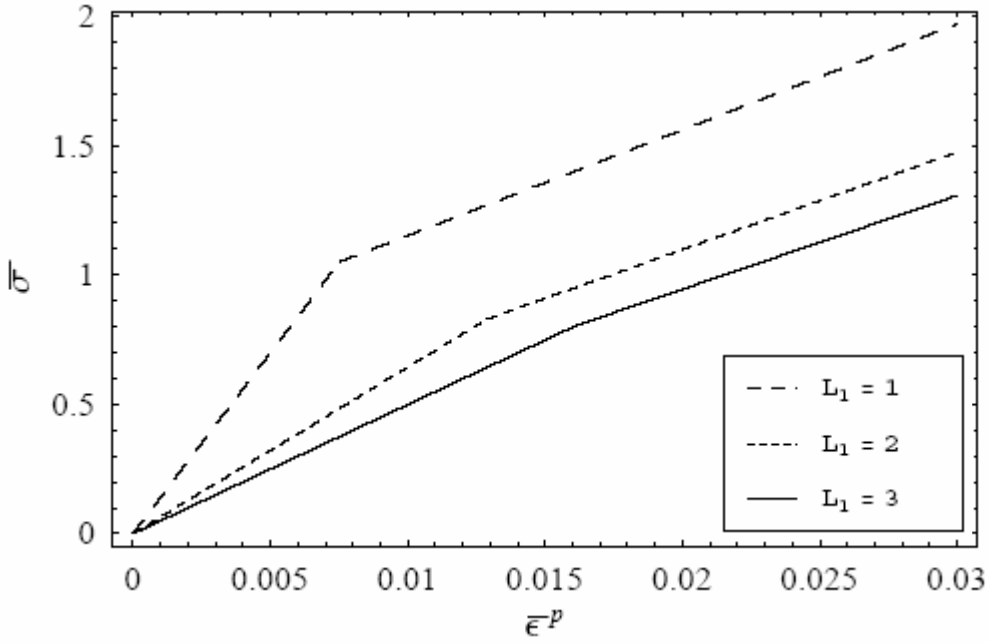

Fig. 4.3: Interfacial yield point and size effects nonlinear interfacial energy

As in Fig. 4.2, an obvious size effect is observed indicating that for fixed internal lengths, the smaller the separation of interfaces is, the stronger the average response of the system is. In fact, as shown in the figure, the overall stress-strain relation is bilinear. The "knee" observed in these curves indicates the "interfacial yield" point. The first portion of each curve is valid for an elastic-like behavior of the interface implied by the fact that no dislocations are allowed to penetrate it since the plastic strain is kept zero there. This portion of the curve also indicates that the effect of the impermeability of the interface to dislocations is to induce an overall stiffer response for the medium as the interfacial separation decreases. The critical stress $\bar{\sigma}_c$ at which the interface yields also increases with decreasing specimen size, as indicated by the "knee" of the graphs depicted in the figure. After "interfacial yielding" occurs ($\bar{\sigma} > \bar{\sigma}_c$), both the internal surface and material interior deform plastically in a "perfectly plastic" and "linearly hardening" fashion, respectively. Finally, the required applied stress for continuous plastic flow is described by the second portion of the bilinear curves indicating again that the strength increases with decreasing size.

4.2 ELASTIC-PLASTIC BOUNDARY VALUE PROBLEM

In both the examples considered in the previous section, during deformation (even for relatively small loads) plastic strain was always present in the interior of the material; as a result there was no pure elastic region in the stress-strain curve; to emphasize this, stress was plotted versus mean plastic strain (Figs 4.2&4.3). In this section, a purely elastic region is considered; this is accomplished through consideration of the grain interior yield stress σ_0 in the gradient dependent plastic potential as

$$V(\varepsilon^P, \varepsilon^P_{,x}) = \sigma^i_0 \left|\varepsilon^P\right| + \frac{1}{2}\beta_i \ell_i^2 (\varepsilon^P_{,x})^2 . \tag{4.12}$$

The interface is again taken to behave nonlinearly, according to (4.7).

Prior to grain interior yielding there is no plastic strain present in the material. Therefore, differentiation of (4.12) according to (3.11*b*) to obtain σ, when $\varepsilon^P = 0$, yields that σ can take any value up to σ_0. This indeterminacy is settled by elasticity since, for $\varepsilon^P \equiv 0$, the constitutive relation (3.11*a*) for the total stress implies a standard elastic relation for the average stress-strain response of the bi-crystal

$$\sigma = E\left(\frac{du}{dx} - \varepsilon^P\right) \Rightarrow \sigma = E\varepsilon, \quad \sigma < \sigma_0 . \tag{4.13}$$

Accounting for the fact that the material under consideration consists of two phases, the purely elastic average stress-strain response is found by use of the the displacement boundary and continuity conditions $(4.1)_{1,2,5}$ as

$$\bar{\sigma} = \frac{E_1 E_2 (L_1 + L_2)}{E_1 L_2 + E_2 L_1}\bar{\varepsilon} \text{ , when } \varepsilon^p = 0 . \tag{4.14}$$

The next portion of the stress-strain curve is constructed by assuming that phase 2 has a lower yield stress. Once σ_0^2 is reached, ε_2^P is given by inserting (4.12) in $(4.2)_2$

$$\beta_2 \ell_2^2 \frac{d^2 \varepsilon_2^P}{dx^2} + \bar{\sigma} = \sigma_0^2 \Rightarrow \varepsilon_2^P = -\frac{\bar{\sigma} - \sigma_0^2}{2\beta_2 \ell_2^2} x^2 + A_2 x + B_2 , \tag{4.15}$$

where the constants of integration are calculated through use of the fourth condition in (4.1) and letting $\varepsilon_2^P(0) = 0$ (since it is assumed that the interface yields last). Phase 1 remains purely elastic and hence $\varepsilon_1^P = 0$. Finally, use of the displacement boundary and continuity, across interface, conditions of (4.1) gives

$$\bar{\sigma} = \frac{E_1 E_2 L_2^3 \sigma_0^2 + 3\beta_2 E_1 E_2 \ell_2^2 (L_1 + L_2)\bar{\varepsilon}}{E_1 E_2 L_2^3 + 3\beta_2 \ell_2^2 (E_1 L_2 + E_2 L_1)}, \text{ when } \sigma_0^2 \le \bar{\sigma} \le \sigma_0^1 . \tag{4.16}$$

Once the applied stress reaches σ_0^1, phase 1 yields also, and ε_1^P is given by an expression similar to (4.15) but with the subscripts 2 replaced with 1. The

integration constants for ε_1^P are found through $(4.1)_3$ and $\varepsilon_1^P(0)=0$; while those for ε_2^P remain the same as before. Use of the usual displacement conditions gives the pre-interfacial yield average response as

$$\bar{\sigma}=\frac{E_1E_2(\beta_2\ell_2^2L_1^3\sigma_0^1+\beta_1\ell_1^2L_2^3\ell_1^2\sigma_0^2)+3\beta_1\beta_2E_1E_2\ell_1^2\ell_2^2(L_1+L_2)\bar{\varepsilon}}{E_1E_2L_1^3\ell_2^2\beta_2+\beta_1\ell_1^2(E_1E_2L_2^3+3\ell_2^2\beta_2+(E_2L_1+E_1L_2))}, \text{ when } \bar{\sigma}\le\bar{\sigma}_c\,. \quad (4.17)$$

Finally, the post-interfacial yield response is found through use of all conditions in (4.1) in combination with the jump condition $(4.8)_2$ as

$$\bar{\sigma}=\frac{\gamma+L_1\sigma_0^1+L_2\sigma_0^2}{L_1+L_2}\,, \text{ when } \bar{\sigma}=\bar{\sigma}_c\,. \quad (4.18)$$

Allowing the material parameters to take the values $\gamma=0.1$, $\beta_1=1$, $\beta_2=3$, $\ell_1=1$, $\ell_2=1.5$, E_1=40, E_2=20, $\sigma_0^1=0.04$, $\sigma_0^2=0.02$, (according to experimental evidence E is taken 1000 times greater from σ_0) and letting the ratio L_2/L_1=1.5, provides Fig. 4.4.

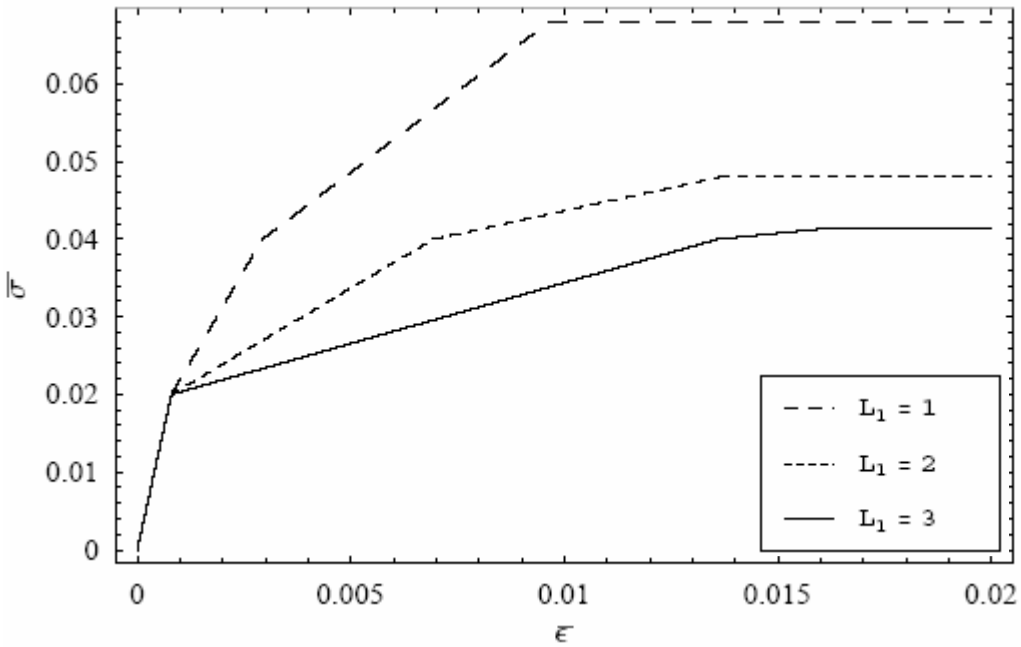

Fig. 4.4: Elastoplastic material response and related size effects

It can be seen that four linear segments of the curves in Fig. 4.4, corresponding to (4.14), (4.16), (4.17) and (4.17), constitute the overall stress-srain response of the material; the first and second "knees" indicate the yielding of phases 2 and 1 respectively, while the third "knee" corresponds to yielding of the interface.

It should be noted that the purely elastic response (first portion of curves in Fig. 4.4) is the same for all specimen sizes, since it is independent of the internal length, and depends on the overall volume fractions of phases 1 and 2, as seen in (4.14). When the material behaves in a purely elastic manner, the interfaces have no contribution since no dislocation pile-ups occur across them. Once phase 2 yields (second segment in curves of Fig. 4.4), and, hence, the applied stress lies in the region $\sigma_0^2 \le \bar{\sigma} \le \sigma_0^1$, the purely elastic response of phase 1 is competing with the perfect plastic response of phase 2; in addition the interface does not permit dislocation penetration and hence contributes to the stress-strain curve through a stiffening manner. The third linear segment of this figure indicates the response when phase 1 has also yielded, but the interface continues to obstruct dislocation motion through its stiffening behavior. This "stiffening" mechanism (which is similar to that present in the first segment of the bilinear plots in Fig. 4.3) competes with the assumed "perfect" plasticity taking place in the grain interiors, resulting into a reduced average stiffening response. After the applied stress reaches a critical value ($\bar{\sigma} = \bar{\sigma}_c > \sigma_0^1 > \sigma_0^2$), causing yielding of the interface and allowing dislocations to penetrate it, both the interior and interface deform in a perfectly plastic manner, and continuous plastic flow of the material occurs at a constant value of the applied stress, as shown in the last linear portion of Fig. 4.4.

Although the gradient-dependent plastic potential in all examples considered so far had a relatively simple form, it was very effective in exhibiting the new features of the formulation developed in Chapter 3, such as scale effects not

limited by an upper bound, as well as the existence of an "interfacial yield" stress. In particular, interfacial yield was clearly depicted, as a sharp "knee", in the resulting stress-strain curves.

4.3 THE FLECK-WILLIS GRADIENT-DEPENDENT PLASTIC POTENTIAL

The form of V that is considered in this section and those to follow results in highly nonlinear differential equations and hence it is not possible to obtain analytical exact solutions if the material has two phases. Therefore the remaining two sections of this chapter are concerned with homogeneous media, such as polycrystals, in which grain boundaries are distributed periodically with period $2L$. It suffices to consider one periodic cell, occupying the region $-L< x < L$, with an interface at $x=0$. It is therefore necessary to consider only the half period $0< x <L$ with the conditions

$$[\tau] = 2\tau(0^+) = \phi'\big|_{x=0}\,;\tau(L) = 0\,. \tag{4.19}$$

The nonlinear gradient potential that will be first considered is that employed by Fleck and Willis [7]. In one dimension it reads

$$V\left(\varepsilon^P, \varepsilon^P_{,x}\right) = \frac{\sigma_o e_o}{n+1}\left(\frac{E_P}{e_o}\right)^{n+1} \text{ where } E_P \equiv \left[{\varepsilon_P}^2 + \ell^2\left(\varepsilon^P_{,x}\right)^2\right]^{1/2}, \tag{4.20}$$

where n is the hardening exponent and e_0 the normalizing strain. The interfaces behave according to the nonlinear manner defined by (4.7). Substitution of (4.20) in $(3.14)_2$ results in the following differential equation

$$\frac{1}{\left(E_P\right)^{3/2}}\left\{\sigma_o \ell^2\left[\frac{\sqrt{\left(\varepsilon^P\right)^2 + \ell^2\left(\varepsilon^P_{,x}\right)^2}}{e_o}\right]^n\left[n\ell^2\left(\varepsilon^P_{,x}\right)^2\varepsilon^P_{,xx} + \varepsilon^P\left((n-1)(\varepsilon^P_{,x})^2 + \varepsilon^P_{,x}\varepsilon^P_{,xx}\right)\right]\right\}$$

$$-\frac{\sigma_o \varepsilon^P_{,x}}{e_o}\left(E_P\right)^{n-1} = -\bar{\sigma}, \tag{4.21}$$

to be solved along with the following conditions (that result by direct substitution of ϕ and V in (4.19))

$$\varepsilon^{p}_{,x}(0) \;\langle\; \frac{\gamma}{2\sigma_o \ell^2}\left(\frac{e_o}{E_P}\right)^{n-1} \text{ when } \varepsilon^{p}(0)=0, \text{ or } \varepsilon^{p}_{,x}(0) = \frac{\gamma}{2\sigma_o \ell^2}\left(\frac{e_o}{E_P}\right)^{n-1} \text{ when } \varepsilon^{P}(0)\neq 0$$

and
$$\varepsilon^{P}_{,x}(\pm L)=0. \tag{4.22}$$

Due to the highly nonlinear nature of (4.21), only a numerical solution for the stress-strain curve can be found. Fig. 4.5 is obtained by letting the material parameters assume the values σ_o=10, e_o=0.01, γ=22, $\ell = 1$ and n=0.1.

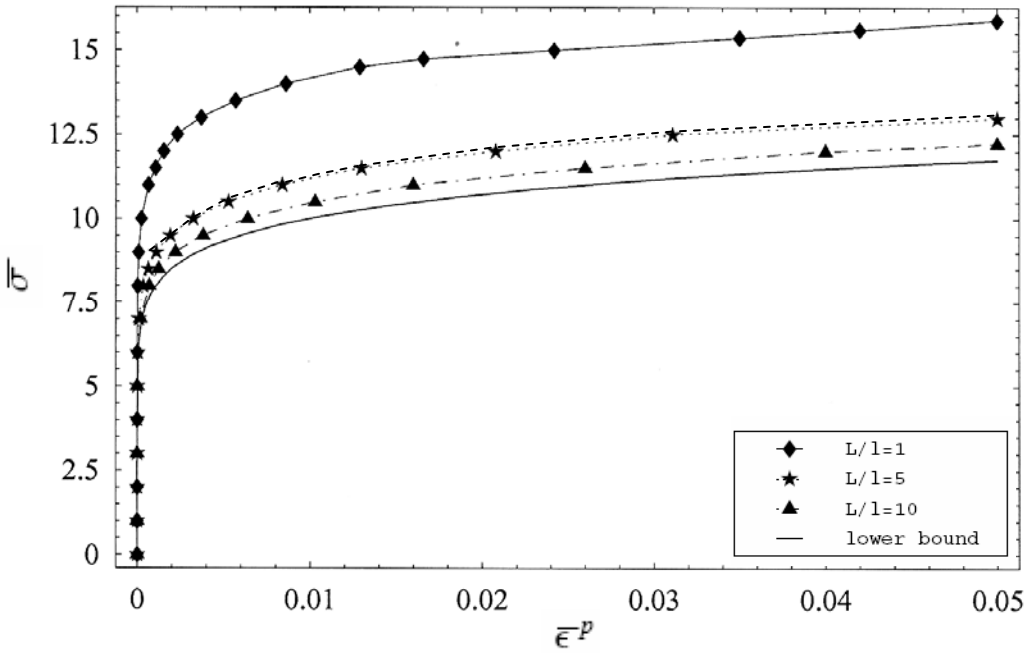

Fig. 4.5: Size effects for F-W potential when n=0.1

It can be seen that the size effects are similar to those obtained previously (Figs. 4.2, 4.3&4.4) i.e. as the specimen size decreases the applied stress required for continuous plastic deformation of the material increases. The lower bound that is depicted results from (3.35) and is given by

$$V_R(\bar{\varepsilon}^p) \equiv \frac{\sigma_0 e_0}{n+1}\left(\frac{\bar{\varepsilon}^p}{e_0}\right)^{n+1} \leq V^{eff}(\bar{\varepsilon}^p). \tag{4.23}$$

Fig. 4.6 is constructed for a material with the same material parameters, but a higher hardening exponent, *n*=0.3.

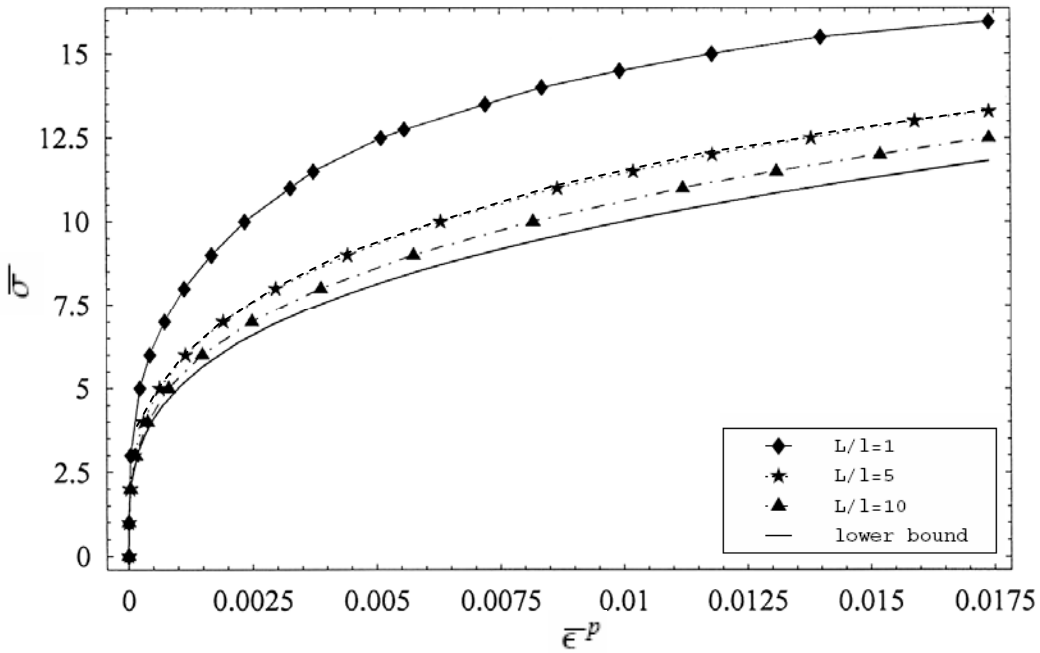

Fig. 4.6: Size effects for F-W potential when n=0.3

4.4 A NEW GRADIENT DEPENDENT PLASTIC POTENTIAL

Since there is no physical evidence justifying the existence of materials with a response according to that defined by Fleck and Willis [7], another highly nonlinear V is introduced here for comparison purposes

$$V\left(\varepsilon^P, \varepsilon^P_{,x}\right) = \frac{\sigma_o e_o}{n+1}\left(\frac{\varepsilon^P}{e_o}\right)^{n+1} + \frac{\sigma_o e_o \ell^2}{2}\left(\frac{\varepsilon^P_{,x}}{e_o}\right)^2 . \tag{4.24}$$

This V produces a simpler differential equation when substituted in $(3.14)_2$

$$\sigma_o\left(\frac{\varepsilon^P}{e_o}\right)^n - \frac{\sigma_o \ell^2}{e_o}\left(\varepsilon^P_{,xx}\right) = -\sigma . \tag{4.25}$$

Again the interfaces are taken to be characterized by the nonlinear form of ϕ so the conditions of (4.19) are replaced with

$$\varepsilon^P_{,x}(0) < \frac{\gamma}{2\sigma_o \ell} \text{ when } \varepsilon^P(0) = 0 , \quad \text{or} \quad \varepsilon^P_{,x}(0) = \frac{\gamma}{2\sigma_o \ell} \text{ when } \varepsilon^P(0) \neq 0$$

and $$\varepsilon^P_{,x}(\pm L) = 0 . \tag{4.26}$$

Numerical solution of (4.25), along with (4.26) (allowing for the same material parameters as in the previous section) provides the scale effects shown in Fig. 4.7. The distinct corner, observed when L=1 indicates the "interfacial-yield" point.

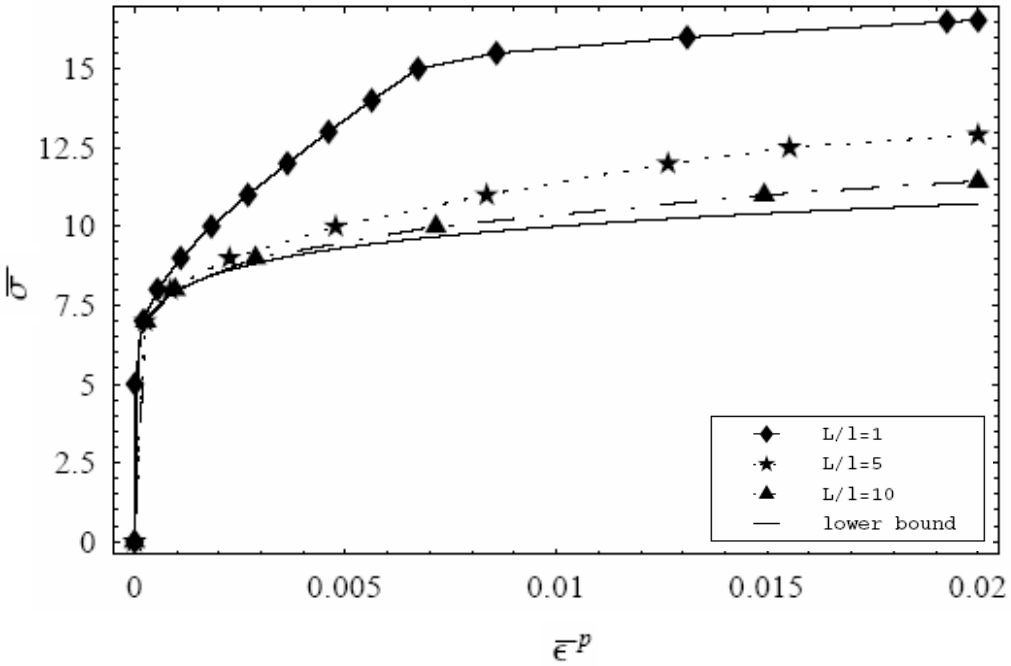

Fig. 4.7: Size effects for new gradient dependent potential when n=0.1 and γ=22

Since the exact material values were used to obtain Figs. 4.5&4.7, it follows that they can be compared directly.

It is observed that the newly introduced gradient-dependent plastic potential allows for greater scale-effects. This can be easily demonstrated by combining the curves from both potentials in a new plot; hence Fig. 4.8 is constructed. The dotted and smooth curves indicate the F-W and new potential respectively. What is of particular interest is the fact that the curves obtained by both *V*s coincide for the largest specimen considered, since except in a negligible boundary layer, the plastic strain is uniform so the gradient term has no effect. In this connection, it should be noted that as the specimen size increases, the

gradient term gradually loses its effect, and hence the solution is given by the lower bound.

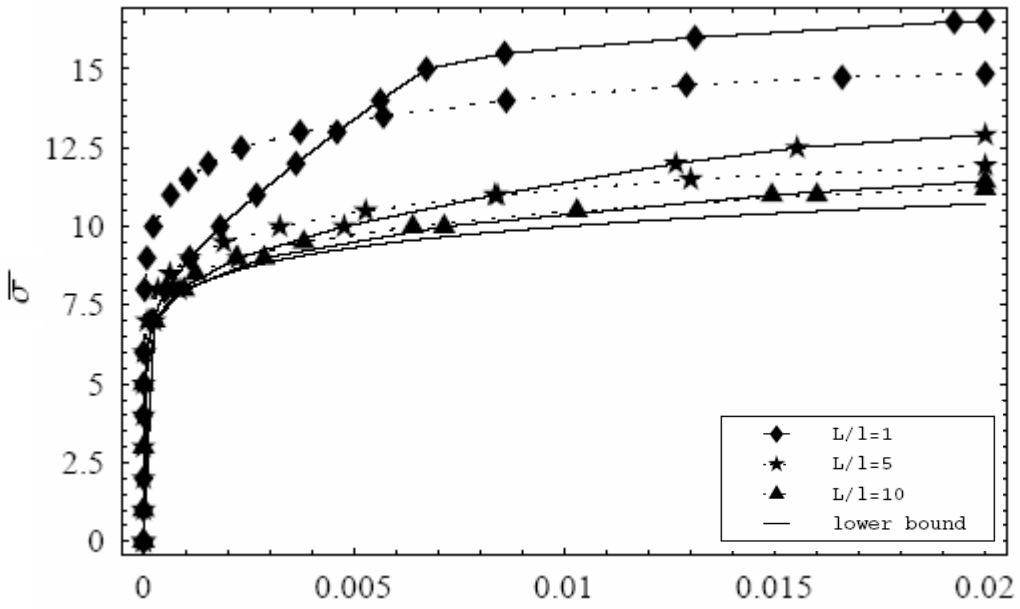

Fig. 4.8: Comparison between the two highly nonlinear potentials when n=0.1

To better illustrate the effect that the value of the interfacial term has, stress-strain plots for this new potential are computed, for the same yield stress and normalizing strain, as before, but with a greater value of γ, γ=50.

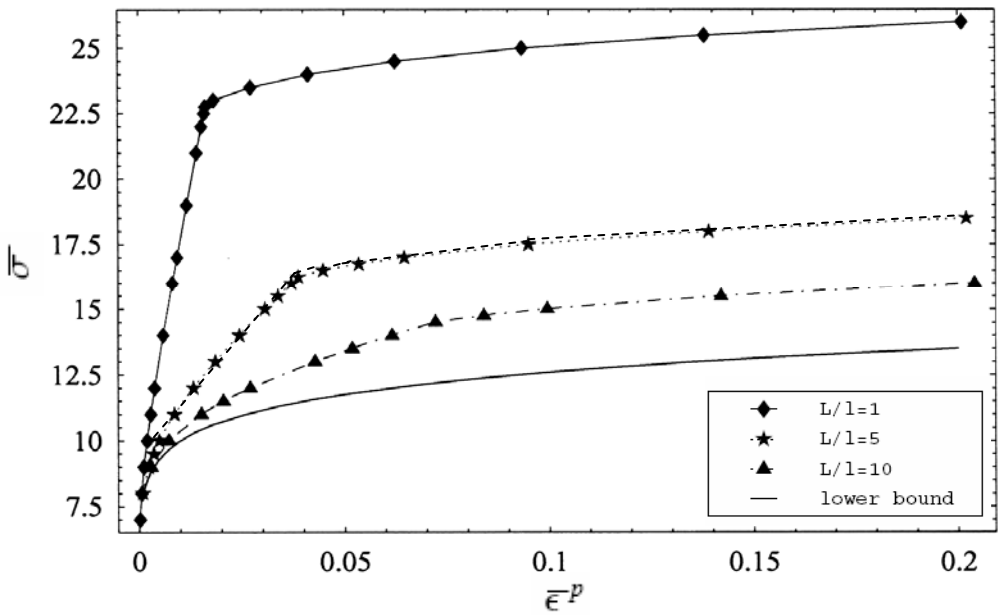

Fig. 4.9: Size effects for new gradient dependent potential when γ=50, n=0.1

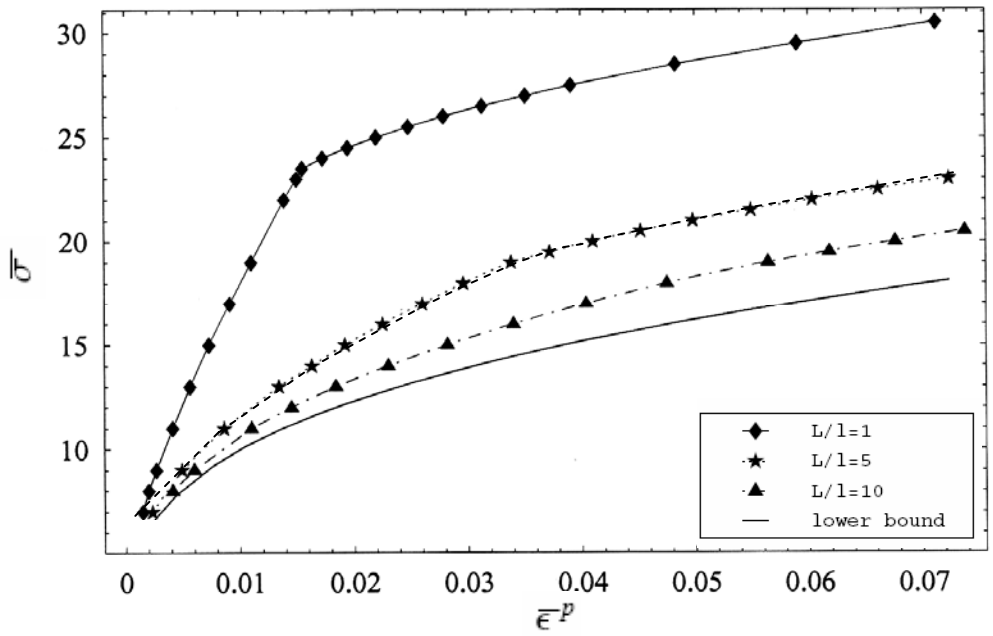

Fig. 4.10: Size effects for new gradient dependent potential when γ=50, n=0.3

From Figs. 4.9&4.10, it can be seen that a sharp corner, indicating "interfacial yield" is rather distinct when $L/\ell = 1$, and $L/\ell = 5$; this feature was also observed, but with less clarity in Fig. 4.7, for the lower value of γ, when $L/\ell = 1$.

Furthermore, direct comparison of Figs. 4.7&4.9 can give an indication of the effect of the interfacial energy-like term in the overall material response, since aside from γ the remaining material parameters used for the construction of both figures remain the same. It can be easily seen that when γ is increased (Fig. 4.9) the overall material response stiffens. This allows us to think of γ as an interfacial strength modulus, and demonstrates the strength enhancing role of interfaces during plastic flow. The most appropriate way therefore to deduce this physical quantity is through dislocation-interface considerations, similar to those discussed in Chapter 2. In particular, examining the formation of dislocation pileups and ledges across boundaries can provide rather good estimates for the interfacial parameter γ; this is demonstrated in Chapter 8, in which the value of γ

that is deduced from dislocation considerations is shown to be in very good agreement with the experimental value, deduced directly from nanoindentation experiments.

CHAPTER 5

LINEAR COMPARISON METHOD FOR HOMOGENEOUS MEDIA

For all periodic examples in the previous chapter it was possible to obtain an exact solution. Once, however, the one-dimensional material under consideration is allowed to have a random microstructure, which in the case of a homogeneous medium is accomplished through a random interface distribution, an exact solution does not exist even if both the interfacial and gradient-dependent plastic potentials assume a simple quadratic form. It is for such media that the variational formulation developed in Chapter 3, in particular the "linear comparison method", comes into its own. Before applying this technique to a medium with a random interface distribution, it is considered more appropriate to apply it to the previously discussed periodic homogeneous media, so that the solutions obtained through the comparison approach can be compared with the aforementioned exact solutions.

5.1 HOMOGENEOUS PERIODIC MEDIUM

5.1.1 Linear Medium

In Chapter 3 it was explained that the response for a linear medium must be obtained, as a first step towards this approach. The gradient-dependent and

interfacial potential of this medium are taken to be quadratic and hence are defined similarly to (4.3) and (4.4). The governing differential equation is also similar to (4.5); the only difference is that since the material is taken to be homogeneous, the suffixes *i* can be ignored. The constants of integration *A* and *B* are found by considering the conditions

$$\beta\ell^2\varepsilon^p_{,x}(0^+) = \alpha\varepsilon^p(0)/2 \text{ and } \varepsilon^p_{,x}(L) = 0\,. \tag{5.1}$$

Expression (5.1) is deduced by inserting the aforementioned V and ϕ in (4.19). Therefore the average stress-strain response is found as

$$\bar{\sigma} = \beta^{eff}\bar{\varepsilon}^p, \tag{5.2}$$

where

$$\beta^{eff} = \beta\left\{\frac{1+\left(2\beta\ \ \ell/\alpha\right)\tanh\left[L/\ell\right]}{1+\left(2\beta\ \ \ell/\alpha - L/\ell\right)\tanh\left[L/\ell\right]}\right\}. \tag{5.3}$$

The effective plastic potential can be found by direct integration of (5.2), according to $(3.6)_2$, since the effective relations conform to the pattern for a non-strain-gradient material, and hence

$$V_c^{eff}(\bar{\varepsilon}^p) = \frac{1}{2}\beta^{eff}(\bar{\varepsilon}^p)^2\,. \tag{5.4}$$

5.1.2 Linear V, nonlinear ϕ

Now the solution for the medium with linear plastic response but nonlinear interface response can be found by inserting (4.3), (4.4), (4.20) and (4.7) for V_c, ϕ_c, V, and ϕ, respectively, in (3.37) and optimizing the resulting inequality with respect to the material parameters, α and β, of the linear medium. Performing the optimization first with respect to α is equivalent to solving the problem for a linear medium (with constant β), but with the nonlinear interface potential (4.7). This generates the potential for this case V_0^{eff} given by

$$V_0^{eff}(\bar{\varepsilon}^p) = \inf_{\alpha}\left\{V_c^{eff} + \frac{E}{\alpha}\right\}, \tag{5.5}$$

where E is defined as

$$E = \frac{\gamma^2}{4L}, \text{so that} \max\left(\gamma\left|\varepsilon^p\right| - \alpha(\varepsilon^p)^2/2\right) = E/\alpha\,. \tag{5.6}$$

Completion of the infimum calculation, which is approached either as $\alpha\to\infty$ or for a finite stationary point, provides that the "refined" upper bound for the effective potential is

$$V_0^{eff}(\overline{\varepsilon}^p) = \frac{\beta(\overline{\varepsilon}^p)^2}{2[1-(\ell/L)\tanh(L/\ell)]}, \qquad \text{when } \overline{\varepsilon}^p \le \varepsilon_c^p$$

$$= \frac{\beta(\overline{\varepsilon}^p)^2}{2[1-(\ell/L)\tanh(L/\ell)]} + \frac{1}{2}\beta\left[(\overline{\varepsilon}^p)^2 - (\varepsilon_c^p)^2\right] + \frac{\gamma}{2L}[\overline{\varepsilon}^p - \varepsilon_c^p] \quad \text{when } \overline{\varepsilon}^p \ge \varepsilon_c^p, \tag{5.7}$$

where

$$\varepsilon_c^P = \frac{\gamma}{2\ell\beta}\left\{\frac{1-(\ell/L)\tanh(L/\ell)}{\tanh(L/\ell)}\right\}. \tag{5.8}$$

It should be noted that relations (5.7-5.8) are reproduced if the exact stress-mean plastic strain response is integrated; the exact solution is easily obtained by solving the differential equation (4.5) along with the conditions

$$\varepsilon_{,x}^p(L) = 0; \varepsilon^p(0) = 0 \text{ as long as } [\tau] \le \gamma, \text{ or } \beta\ell^2\varepsilon_{,x}^p(0^+) = \gamma/2 \text{ otherwise.} \tag{5.9}$$

5.1.3 Nonlinear material response

The refined upper bound for the Fleck-Willis potential is found through comparison with the linear medium of Section 4.5.1; hence (4.3), (4.4), (4.20) and (4.7) are substituted for V_c, ϕ_c, V, and ϕ, respectively, in (3.37) to obtain the inequality

$$V^{eff}(\overline{\varepsilon}^p) \le V_c^{eff} + \frac{\sigma_0 e_0}{2}\left(\frac{1-n}{1+n}\right)\left(\frac{\sigma_0}{\beta e_0}\right) + \frac{E}{\alpha}. \tag{5.10}$$

If the first and second terms in (5.10) are optimized with respect to α they can be replaced by (5.5); in particular since only these terms contain α optimizing (5.10) with respect to this parameter gives

$$V^{eff}(\bar{\varepsilon}^p) \le V_0^{eff} + \frac{\sigma_0 e_0}{2}\left(\frac{1-n}{1+n}\right)\left(\frac{\sigma_0}{\beta e_0}\right), \tag{5.11}$$

where V_0^{eff} is given by (5.7). The remainder of the minimization, with respect to β, has to be performed numerically.

If the comparison method is applied to the other highly non-linear V (4.24) of Section 4.4, the expression of the refined upper bound is given again by (5.11), but now the internal length needs to be scaled since it is multiplied with additional material parameters in the actual V. So to obtain an upper bound for this case ℓ in (5.11) has to be replaced with a scaled internal length ℓ_*, which is given as

$$\beta \ell_*^2 = \sigma_o e_o \ell^2 \Rightarrow \ell_* = \ell\left(\frac{\sigma_o e_o}{\beta}\right)^{\frac{1}{2}}. \tag{5.12}$$

Finally, it follows directly from Chapter 3 that the elementary lower and upper bounds for these nonlinear Vs are

$$V_R(\bar{\varepsilon}^p) \equiv \frac{\sigma_0 e_0}{n+1}\left(\frac{\bar{\varepsilon}^p}{e_0}\right)^{n+1} \le V^{eff}(\bar{\varepsilon}^p) \le \frac{\sigma_0 e_0}{n+1}\left(\frac{\bar{\varepsilon}^p}{e_0}\right)^{n+1} + \frac{\gamma\left|\bar{\varepsilon}^p\right|}{2L} \equiv V_V(\bar{\varepsilon}^p). \tag{5.13}$$

In order to compare the exact solutions for V^{eff}, which can be obtained through integration of the curves in Figs. 4.5, 4.6, and 4.7 (according to $(3.6)_2$), with the "refined" upper bound obtained from the comparison method, Figs. 5.1a&5.2a are constructed by minimizing (5.11) with respect to β. In addition to the effective potential-mean plastic strain curves, the comparison method, as well as the upper and lower bounds, which are depicted in Figs. 5.1a&5.2a can provide estimates for the mean stress-plastic stain response by performing a numerical differentiation to the corresponding curves in Figs. 5.1a and 5.2a. Since the derivative is not necessarily a bound, the stress-strain solutions are just approximations; again for comparison reasons they are plotted against the exact solutions of Sections 4.3 and 4.4.

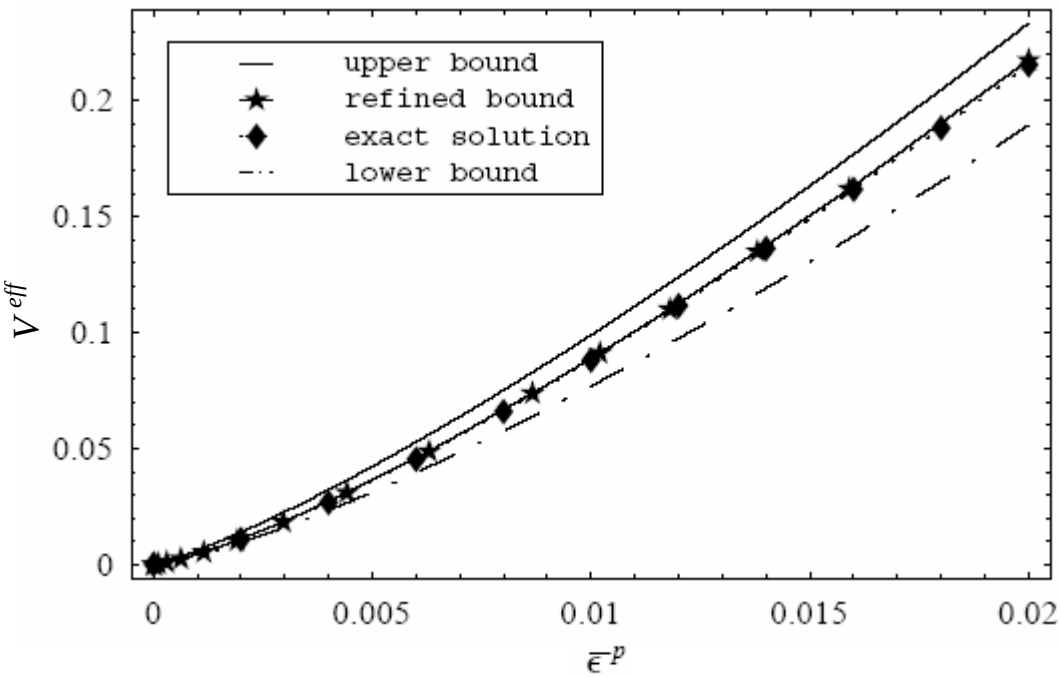

Fig. 5.1a: Comparison between exact solution and bounds for F-W potential when σ_0=10. e_0=0.1. ℓ =1.n=0.3 and L/ℓ =5

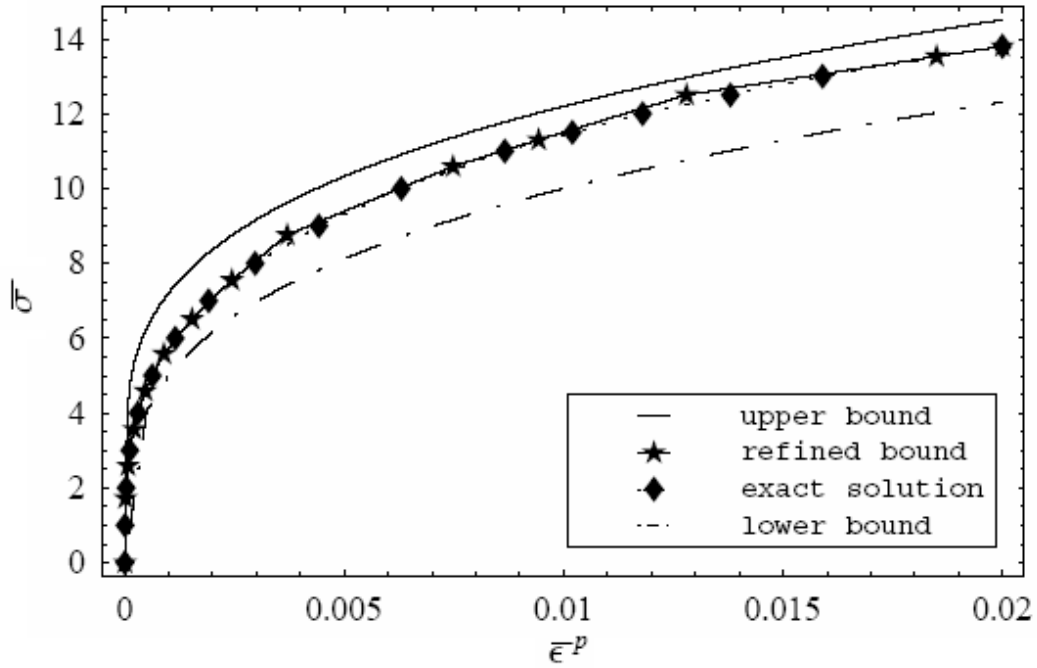

Fig. 5.1b: Comparison between exact solution and approximation from bounds for F-W potential when σ_0=10, e_0=0.1, ℓ =1, n=0.3 and L/ℓ =5

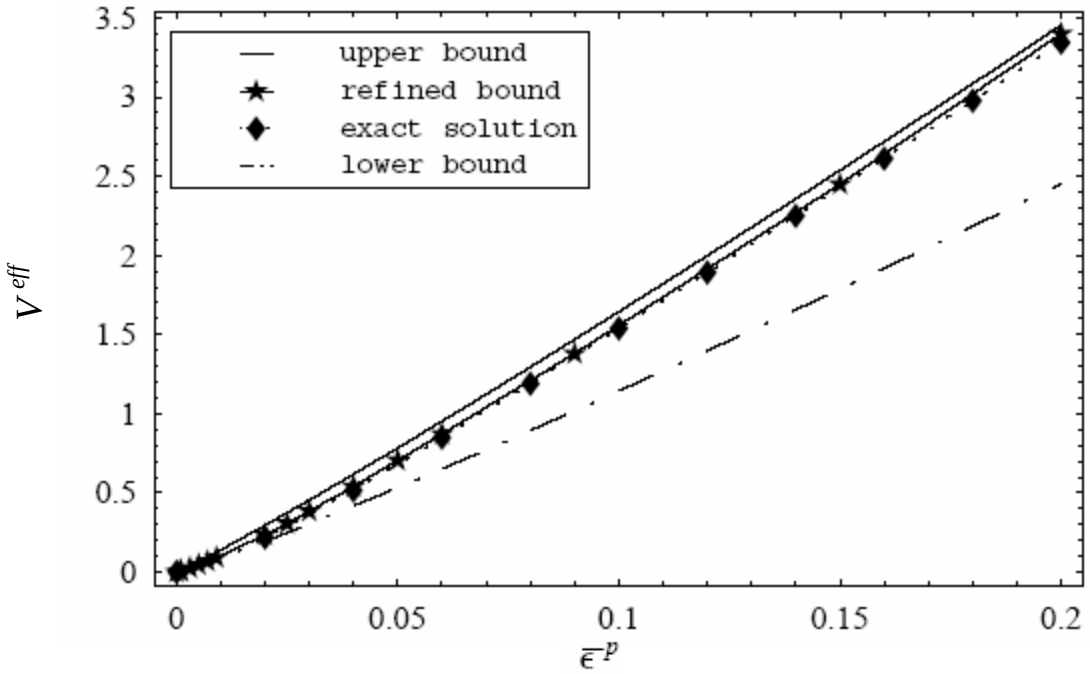

Fig. 5.2a: Comparison between exact solution and bounds for new gradient potential when σ_0=10, e_0=0.1, ℓ =1, γ=50, n=0.1 and $L/\ell = 5$

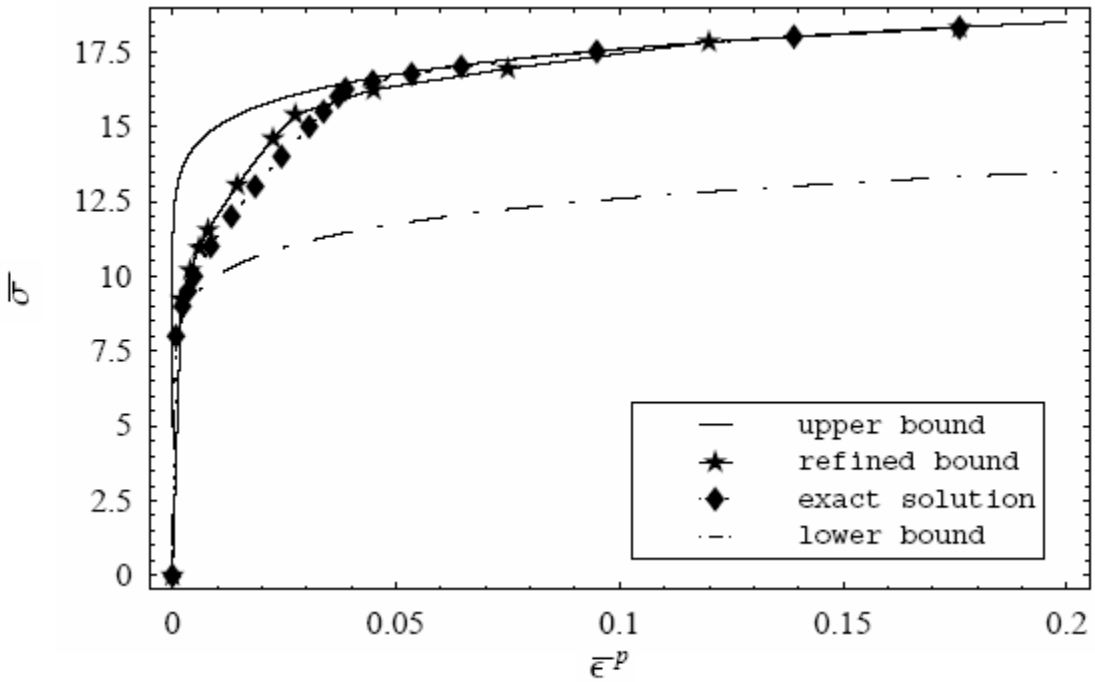

Fig. 5.2b: Comparison between exact solution and approximations from bounds for new gradient potential when σ_0=10, e_0=0.1, ℓ =1, γ=50, n=0.3 and L/l=5

As it can be seen from the above figures the exact solutions and the "refined" upper bounds obtained through the comparison method are in very close proximity. This method is thus proven to be very reliable (at least for the one-dimensional case at hand) and will be employed in the remainder of this work to find the effective response of materials for which an exact solution does not exist.

5.2 HOMOGENEOUS RANDOM MEDIUM

Based on the previously proven robustness of the linear comparison method, it is employed here to obtain the effective response for a random highly nonlinear homogeneous medium, which has the same material and interfacial response as that in Section 5.1.1; hence the gradient dependent plastic potential is given by (4.20) or (4.24), while the interfacial energy is given by (4.7); the interfaces, however, are now distributed randomly, according to a Poisson process of intensity $\lambda=1/(2L)$.

Since the linear comparison medium approach will be adopted, the first step is to obtain the effective response of a random linear medium with potentials given by (4.3) and (4.4). Due the random interface distribution an exact effective stress-strain response cannot to be computed and therefore two- and three- point statistics are employed for the development of a lower and upper bound, respectively.

5.2.1 Approximate solution

Consideration of pairwise statistics of the interfaces through use of the "quasicrystalline approximation" of Lax [69], as shown in Appendix A, provide

$$\beta^{eff} = \beta\left\{1+\frac{\ell / L}{1+(2\ell\beta/\alpha)}\right\}. \tag{5.14}$$

Equality is used for convenience in (5.14) but it is proven in the appendix that this is in fact a lower bound. Inserting (5.14) in (5.4) provides

$$V_c^{eff}(\bar{\varepsilon}^p) = \frac{1}{2}\beta\left(1+\frac{\ell/L}{1+(2\ell\beta/\alpha)}\right)(\bar{\varepsilon}^p)^2 . \tag{5.15}$$

Similarly V_0^{eff} takes the form indicated in (5.5) but with V_c^{eff} having the form of (5.15) (E is defined as in (5.6)), hence

$$V_0^{eff}(\bar{\varepsilon}^p) = \inf_{\alpha}\left\{V_c^{eff}+\frac{E}{\alpha}\right\} = \inf_{\alpha}\left\{\frac{1}{2}\beta\left(1+\frac{\ell/L}{1+(2\ell\beta/\alpha)}\right)(\bar{\varepsilon}^p)^2+\frac{E}{\alpha}\right\}. \tag{5.16}$$

The infimum is again obtained either as $\alpha\to\infty$ or for a finite, stationary point. Completion of the details provides

$$\begin{aligned} V_0^{eff}(\bar{\varepsilon}^p) &= \frac{1}{2}\beta\left(1+\frac{\ell}{L}\right)(\bar{\varepsilon}^p)^2, && \text{when } \bar{\varepsilon}^p \le \varepsilon_c^p \\ &= \beta\left(1+\frac{\ell}{L}\right)(\varepsilon_c^p)^2+\frac{1}{2}\beta\left[(\bar{\varepsilon}^p)^2-(\varepsilon_c^p)^2\right]+\frac{\gamma}{2L}[\bar{\varepsilon}^p-\varepsilon_c^p], && \text{when } \bar{\varepsilon}^p \ge \varepsilon_c^p, \end{aligned} \tag{5.17}$$

where

$$\varepsilon_c^p = \frac{\gamma}{2\ell\beta}. \tag{5.18}$$

Now everything is set to compute the effective response of the nonlinear medium with nonlinear interfacial response; hence (4.3), (4.4), (4.20)/(4.24) and (4.7) are substituted for V_c, ϕ_c, V, and ϕ, respectively, in (3.37). The resulting expression is the same as (5.10), but now V_c^{eff} is defined according to (5.15). As in Section 5.1.1, the optimization over the material parameters can be done sequentially. First optimizing with respect to α generates the expression (5.11), except that now V_0^{eff} is given by (5.17). It should be emphasized that for this case (5.17) is not a bound, but an approximation due to the fact that β^{eff} is a lower bound, and hence the inequalities do not rum the same way.

The minimization with respect to β is performed numerically, producing thus Figs 5.3a&5.4a. The lower bound designated is the same as that for the periodic medium. Numerical differentiation of these curves provides

corresponding approximations for the effective stress-plastic strain relation, shown in Figs 5.3b&5.4b.

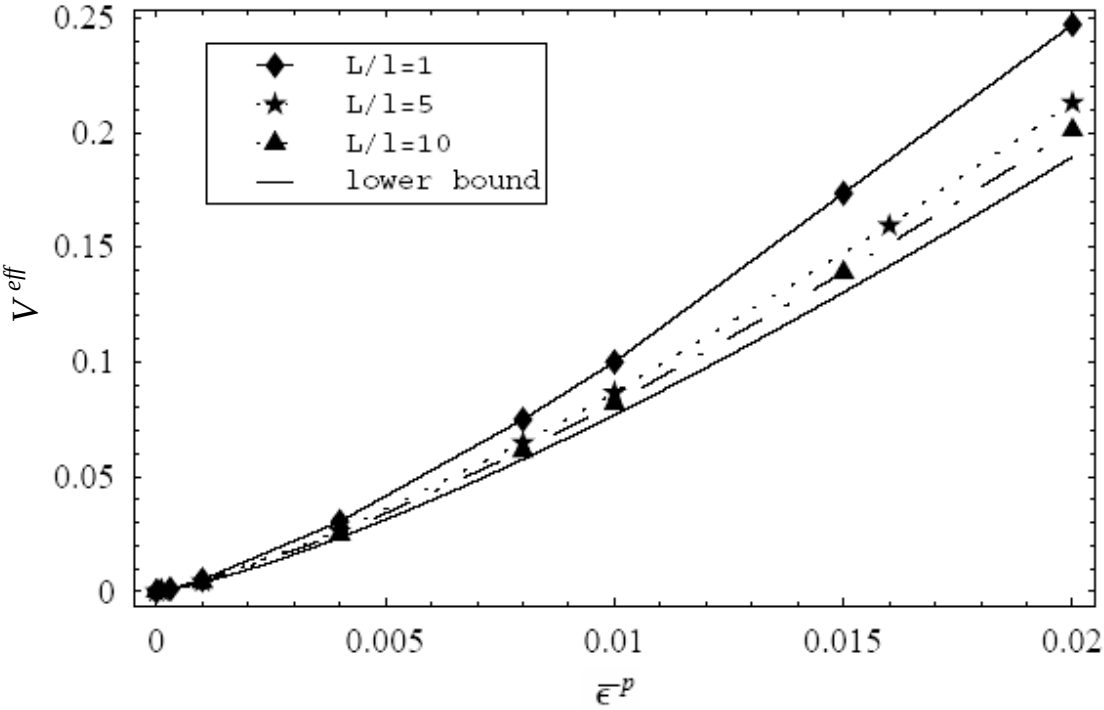

Fig. 5.3a: Size effects for random interface distribution for F-W potential when σ_0=10, e_0=0.1, ℓ =1, γ=22 and n=0.3

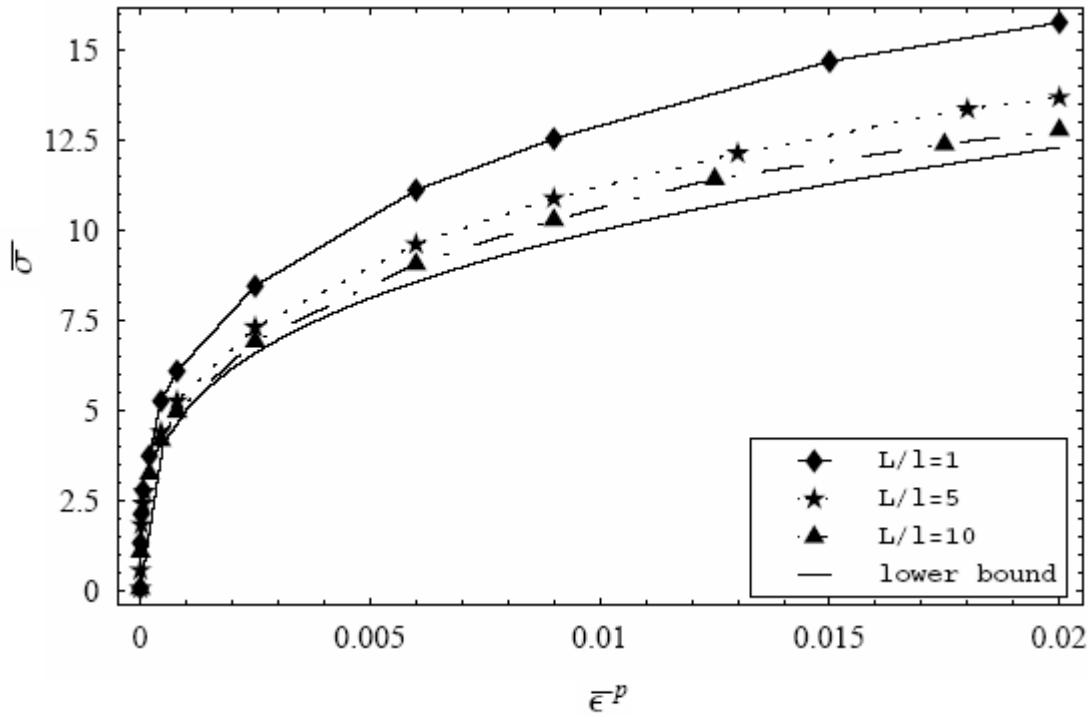

Fig. 5.3b: Size effects for random interface distribution for F-W potential when σ_0=10, e_0=0.1, ℓ =1, γ=22 and n=0.3

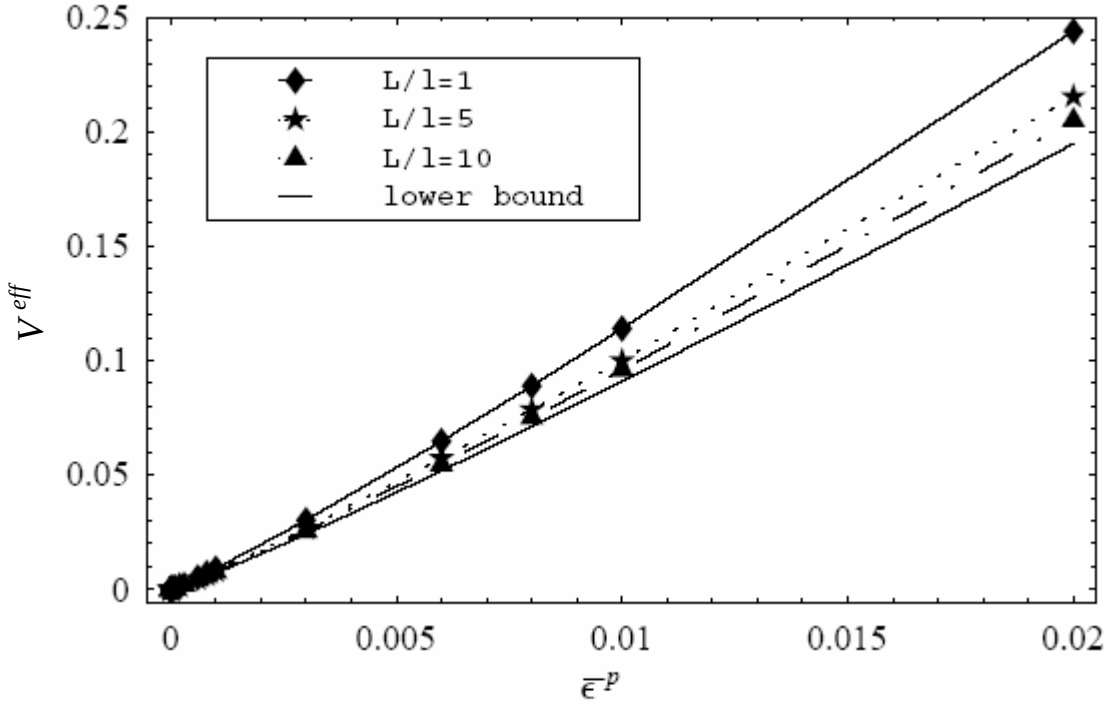

Fig. 5.4a: Size effects for random interface distribution for F-W potential when γ=22 and n=0.1

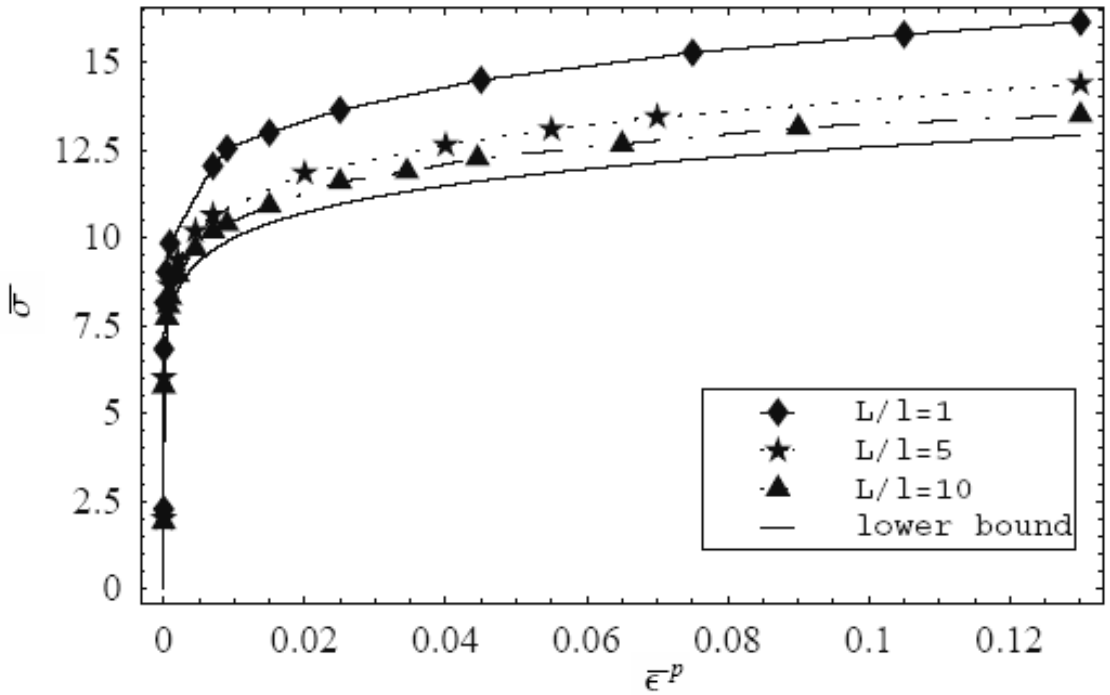

Fig. 5.4b: Size effects for random interface distribution for F-W potential when σ_0=10, e_0=0.1, ℓ =1, γ=22 and n=0.1

In particular, Figs 5.3b&5.4b are directly comparable to Figs 4.6&4.5, respectively, the only difference being the distribution of the interfaces. Figs 4.6&4.5 correspond to "perfectly ordered" interfaces, with exactly uniform spacing $2L$, while Figs 5.3b&5.4b correspond to "perfectly disordered" interfaces, with mean spacing $2L$. The figures for both cases not only show similar trends, but there exists very close numerical proximity for all specimen sizes considered. This is illustrated in Fig. 5.5, for the effective potentials, since they are directly computed from the comparison methods. Thus, the scale effects that are shown would appear to be robust.

Moreover, Fig. 5.6 is obtained for the new gradient potential by inserting (5.17) and (5.12) in (5.11), optimizing with respect to β and then differentiating; comparing Fig. 5.6 with its periodic counterpart (Fig. 4.9), again leads to the conclusion that close agreement exists between the two media.

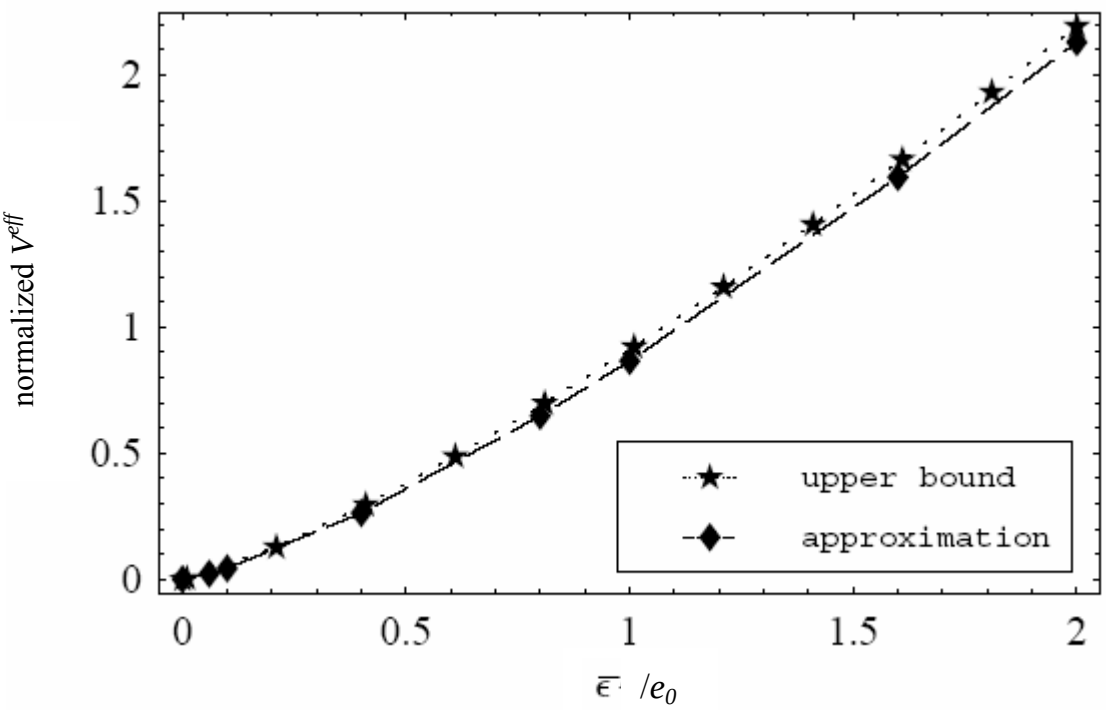

Fig. 5.5: Comparison of random and periodic media for F-W potential, when σ_0=10, e_0=0.01, ℓ =1, γ=22 with n=0.3, and L/ℓ =5

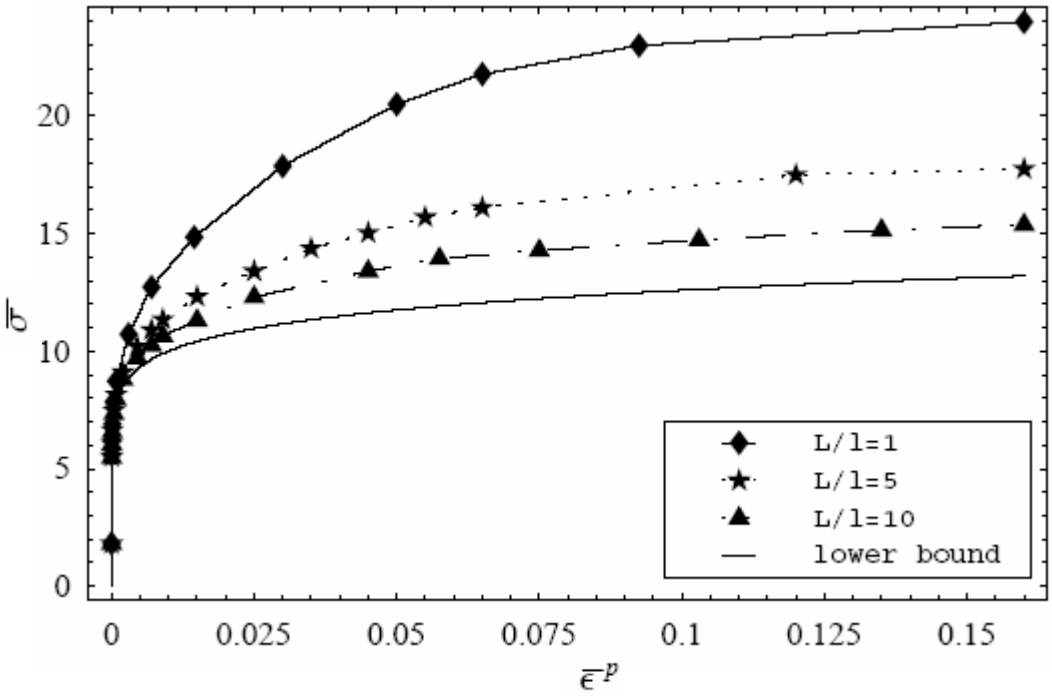

Fig. 5.6: Size effects for random interface distribution for new gradient potential when σ_0=10, e_0=0.01, ℓ =1, γ=50 and n=0.1

5.2.2 Upper bound formulation

As was mentioned the formulation of the previous section provides approximate solutions. The close correlation of these solutions with the upper bound obtained for the periodic medium (Fig. 5.5), is reassuring, but to better understand where these approximate solutions lie compared to the true upper bound of a nonlinear Poisson medium, β^{eff} is recomputed as an upper bound. This is possible by substituting a suitable "trial field" into the minimum principle (3.41). An upper bound which employs the statistics of points taken three at a time is developed in Appendix A. For the Poisson linear medium, it is

$$\beta^{eff} = \beta\left\{1+\frac{\ell}{L}\left(\frac{\alpha}{2\ell\beta}\right)-\frac{(\alpha/(2\ell\beta))^2(\ell/L)}{1+\alpha/(2\ell\beta)(1+\ell/L)}\right\}, \tag{5.19}$$

and therefore the comparison effective plastic potential is rewritten as

$$V_c^{eff}(\bar{\varepsilon}^p) \le \frac{1}{2}\beta\left\{1+\frac{\ell}{L}\left(\frac{\alpha}{2\ell\beta}\right)-\frac{(\alpha/(2\ell\beta))^2(\ell/L)}{1+\alpha/(2\ell\beta)(1+\ell/L)}\right\}(\bar{\varepsilon}^p)^2. \qquad (5.20)$$

The response for the purely non-linear random medium is obtained by substituting (5.20) in (5.10). For this form of β^{eff} the infimum with respect to α is obtained only for a finite stationary point. Hence, the resulting form for V is not divided in pre- and post- yield formulae, and a distinct plastic strain, ε_c^p, at which the interface yields cannot be obtained. The resulting size effects are shown in Fig. 5.7. It can be seen by comparison with the approximate solutions depicted in Fig. 5.4 that both solutions obtained for this nonlinear medium with a Poisson distribution of the interfaces are very close. Since two- and three- point statistics give similar results for the response of the medium under consideration, only two-point considerations will be taken in Chapter 6.

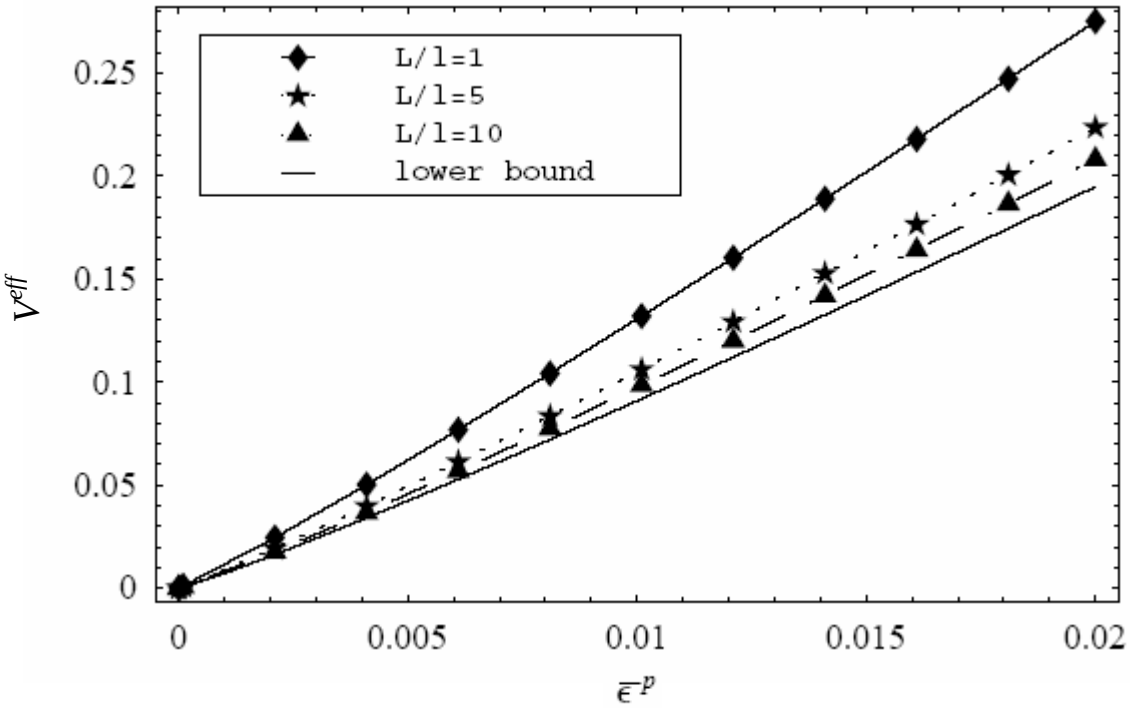

Fig. 5.7*a* : Upper bound for random interface distribution for F-W potential when σ_0=*10*, e_0=*0.01*, ℓ =*1*, γ=*22* and n=0.1

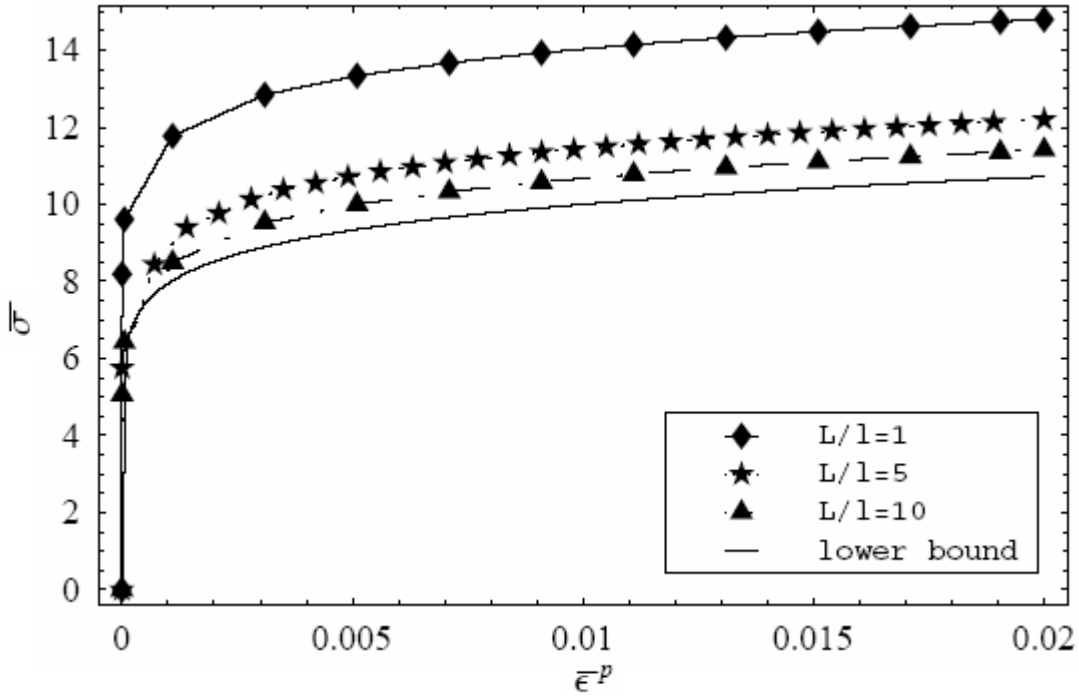

Fig. 5.7b: Upper bound for random interface distribution for F-W potential when σ_0=10, e_0=0.1, ℓ =1, γ=22 and n=0.1

In concluding this chapter it should be emphasized that the significant size effects, of Hall-Petch type, that are obtained for the homogeneous periodic and random media are solely due to the consideration of the "interfacial energy" in the overall energy functional of the material and would not be present in its absence, i.e. if γ=0, whatsoever.

CHAPTER 6

LINEAR COMPARISON FORMULATION FOR TWO-PHASE MEDIA

Since all of the nonlinear examples considered so far were homogeneous their interfaces can be thought of as grain boundaries. The present chapter is concerned with slightly more complicated internal surfaces that arise at the intersection of phases/materials with different chemical composition, and/or significantly different crystallography. Such interfaces are present in the emerging field of metal-metal nanocomposites, such as Nb-Cu wires, and hence the subsequent modeling is very significant for future applications. The mathematics are again simplified by considering only one-dimensional examples, and the comparison method is employed to obtain approximations for the overall stress-mean plastic response. In the case of a periodic distribution of the interfaces an exact solution to the stress-strain curve can be obtained by use of numerical methods. This approach, however, is not adopted because aside from the fact that it is rather involved, the solutions obtained through it cannot be compared with corresponding solutions for a random interface distribution since exact solutions do not exist for such media, as has been previously mentioned. First, the comparison method is generalized so as to account for the

presence of two phases in the domain under consideration, and then it is applied to highly nonlinear periodic and random media.

6.1 COMPARISON FORMULATION FOR TWO PHASES

Since the material at hand is heterogeneous the yield stress and internal length vary according to position, and therefore take the values σ_0^1, ℓ_1 and σ_0^2, ℓ_2 in phases 1 and 2 respectively. Both phases are taken to have a nonlinear gradient dependent plastic response given by (4.20) or (4.24); the corresponding yield stress and internal length for each phase should be used. Just as in the homogeneous examples, the interfaces are taken to respond in the nonlinear manner defined by potential (4.7). The linear medium employed is the same as that in Section 4.1; hence its gradient dependent potential assumes the form (4.3), while the interfacial response is given by (4.4).

In the case of a periodic medium each segment of material 1 is taken to be of length $2L_1$, similarly material 2 is taken to have length $2L_2$; hence the period is $2L=2(L_1+ L_2)$, and the respective volume fractions of each phase are given as

$$p_1 = \frac{L_1}{L_1 + L_2} \text{ and } p_2 = \frac{L_2}{L_1 + L_2} = 1 - p_1 . \tag{6.1}$$

These volume fractions define probabilities in the case of a statistically uniform two-phase random medium, by taking the mean length of each segment of material 1 to be $2L_1$ and that of material 2 to be $2L_2$. The probability then of finding phase r at x is p_r (i.e. (6.1)).

Inserting the actual and linear comparison potentials, in (3.37), accounting for the fact that two phases are present generates the formula

$$V^{eff}(\bar{\varepsilon}^p) \le V_0^{eff}(\bar{\varepsilon}^p; \beta_1; \beta_2) + \frac{1-n}{2(1+n)} \left\{ p_1 \sigma_0^1 e_0 \left(\frac{\sigma_0^1}{\beta_1 e_0} \right)^{\frac{1+n}{1-n}} + p_2 \sigma_0^2 e_0 \left(\frac{\sigma_0^2}{\beta_2 e_0} \right)^{\frac{1+n}{1-n}} \right\}, \tag{6.2}$$

where the minimization over α has been performed in V_0^{eff} , which as in Chapter 5 denotes the effective potential of a linear medium (4.3), with nonlinear interfacial response (4.7). It should be noted that this formula is valid both when the internal length is taken to be constant or to vary with position x. For the periodic interface distribution, the exact response for a linear two-phase medium with either a linear or nonlinear interfacial response was easily obtained for different internal lengths in each phase (Section 4.1). For the random interface distribution, however, an exact solution cannot be obtained for the comparison medium (just as in the homogenous case), and two point statistics are used for the development of an approximate solution. Since this procedure is rather involved, the internal length in the random medium is taken not to vary according to position for simplification reasons. This simplifying approximation was also employed by Fleck and Willis [7]. Since it was proven in the previous chapter that consideration of both two- and three point statistics results in almost the same results, only two point statistics will be considered.

6.2 SOLUTIONS FOR LINEAR MEDIA

As mentioned the average response for linear, heterogeneous periodic medium was found in Chapter 4 and is given by (4.6); grouping all the constants in (4.6) allows β^{eff} to be written as

$$\beta^{eff} = \frac{A + B/\alpha}{C + D/\alpha}, \tag{6.3}$$

where

$$A = \beta_1\beta_2(L_1 + L_2); B = A\left(\beta_1\ell_1 \tanh\left(\frac{L_1}{\ell_1}\right) + \beta_2\ell_2 \tanh\left(\frac{L_2}{\ell_2}\right)\right)$$

$$C = \beta_1 L_2 + \beta_2 L_1 - \beta_1\ell_2 \tanh\left(\frac{L_2}{\ell_2}\right) - \beta_2\ell_1 \tanh\left(\frac{L_1}{\ell_1}\right)$$

$$D=\beta_2\ell_2(\beta_1L_2+\beta_2L_1)\tanh\left(\frac{L_2}{\ell_2}\right)+\ell_1\tanh\left(\frac{L_1}{\ell_1}\right)\left[\beta_1(\beta_1L_2+\beta_2L_1)-(\beta_1-\beta_2)^2\ell_2\tanh\left(\frac{L_2}{\ell_2}\right)\right].\quad(6.4)$$

It should be noted that β^{eff} is written in the form of (6.3) in order to perform more conveniently the minimization with respect to α. Since the random problem is solved only for the case where the internal length is constant everywhere, it is reasonable for comparison purposes to have the solution for a periodic interface distribution for which the internal length does not vary within the domain under consideration. The solution for such a medium has the form

$$\bar{\sigma}=\beta^{eff}\bar{\varepsilon}^{p}=\left(\frac{A+B/\alpha}{C+D/\alpha}\right)\bar{\varepsilon}^{p},\qquad(6.5)$$

where the constants *A*, *B*, *C* and *D* are found through (6.4) by setting $\ell_1=\ell_2=\ell$, hence

$$A=\frac{L_1+L_2}{\ell};B=A\ell\left(\beta_1\tanh\left(\frac{L_1}{\ell}\right)+\beta_2\tanh\left(\frac{L_2}{\ell}\right)\right),C=\frac{L_1/\ell-\tanh(L_1/\ell)}{\beta_1}+\frac{L_2/\ell-\tanh(L_2/\ell)}{\beta_2},$$
$$D=\left(\frac{L_1}{\beta_1}+\frac{L_2}{\beta_2}\right)\left[\beta_1\tanh\left(\frac{L_1}{\ell}\right)+\beta_2\tanh\left(\frac{L_2}{\ell}\right)\right]\left[\frac{(\beta_1-\beta_2)^2}{\beta_1\beta_2}\ell\tanh\left(\frac{L_1}{\ell}\right)\tanh\left(\frac{L_2}{\ell}\right)\right].\qquad(6.6)$$

Now the two phase random medium is considered. As for the one-phase Poisson case the exact solution for the average response of the linear material cannot be computed. Hence a variational approximation, which is analogous to formula (5.39), is obtained by considering the statistics of points taken two at a time; details are provided in Appendix B. Remarkably, this approximation has the same form as (6.5), except that now the constants A, B, C and D are defined as

$$\begin{aligned}
&A=(L_1+L_2)(\beta_0\ell+\beta_1L_1)(\beta_0\ell+\beta_2L_2),\\
&B=\beta_0\ell(L_1+L_2)(2\beta_1\beta_2L_1L_2+\beta_0\ell(\beta_1L_1+\beta_2L_2)),\\
&C=L_1L_2(\beta_1L_2+\beta_2L_1)+\beta_0\ell(L_1^2+L_2^2),\\
&D=\beta_0\ell(\beta_0\ell(L_1+L_2)^2+2L_1L_2(\beta_1L_2+\beta_2L_1)).
\end{aligned}\qquad(6.7)$$

This approximation is a lower bound if $\beta_0\le\min\{\beta_1,\beta_1\}$, the best bound being obtained when $\beta_0=\min\{\beta_1,\beta_1\}$. Note that choice of any greater value for β_0

generates a variational approximation but not an upper bound, on account of the inequality (B.3).

Correspondingly it follows that the effective response of the comparison medium, either for periodic or random interface distributions is found to be described by

$$V_c^{eff}(\bar{\varepsilon}^p) = \frac{1}{2}\beta^{eff}(\bar{\varepsilon}^p)^2, \tag{6.8}$$

where the appropriate β^{eff}, depending on the medium of interest, is used.

6.3 LINEAR MATERIAL RESPONSE, NONLINEAR INTERFACE RESPONSE

Now, according to the comparison approach inserting (4.3), (4.4), (4.20)/(4.24) and (4.7) for V_c, ϕ_c, V, and ϕ, respectively, in (3.37) provides the generalized effective response for either a periodic or random material with quadratic gradient-dependent potential and nonlinear interfacial potential, as

$$V_0^{eff}(\bar{\varepsilon}^p) = \inf_{\alpha}\left\{V_c^{eff} + \frac{E}{\alpha}\right\} = \inf_{\alpha}\left\{\frac{1}{2}\left(\frac{A+B/\alpha}{C+D/\alpha}\right)(\bar{\varepsilon}^p)^2 + \frac{E}{\alpha}\right\}. \tag{6.9}$$

Since the material is heterogeneous, with each phase having a length L_1 and L_2, E takes the form

$$E = \frac{\gamma^2}{2(L_1+L_2)}. \tag{6.10}$$

As in the previous chapter the infimum of (5.11) is approached either as $\alpha\to\infty$ or for a finite stationary point. The detailed calculation in Appendix C provides

$$\begin{aligned} V_0^{eff}(\bar{\varepsilon}^p) &= \frac{A}{2C}(\bar{\varepsilon}^p)^2, && \text{when } \bar{\varepsilon}^p \le \varepsilon_c^p \\ &= \frac{B}{2D}(\bar{\varepsilon}^p)^2 + \frac{(2E)^{1/2}(AD-BC)^{1/2}}{D}\bar{\varepsilon}^p - \frac{EC}{D}, && \text{when } \bar{\varepsilon}^p \ge \varepsilon_c^p, \end{aligned} \tag{6.11}$$

$$\varepsilon_c^p = \left(\frac{2E}{AD-BC}\right)^{1/2} C. \tag{6.12}$$

Since the form of β^{eff} for the homogeneous periodic and random approximation can be written as (6.3) it follows that (6.11) applies to those examples as well. Expression (6.11) can now be substituted in (6.2) to obtain the effective response of nonlinear two phase media.

6.4 RESULTS FOR TWO-PHASE MEDIA

In Chapter 4 the exact stress-mean plastic response for a two-phase ($\ell_1 \neq \ell_2$) periodic linear medium with nonlinear interface potential was obtained and the resulting scale effects were shown in Fig. 4.3. To see how the results of the comparison method compare with the exact solution, Fig. 6.1 is obtained by inserting (6.4) in (6.11) and then differentiating to obtain an approximation for the stress-plastic strain response; the material parameters are defined as in Section 4.2.

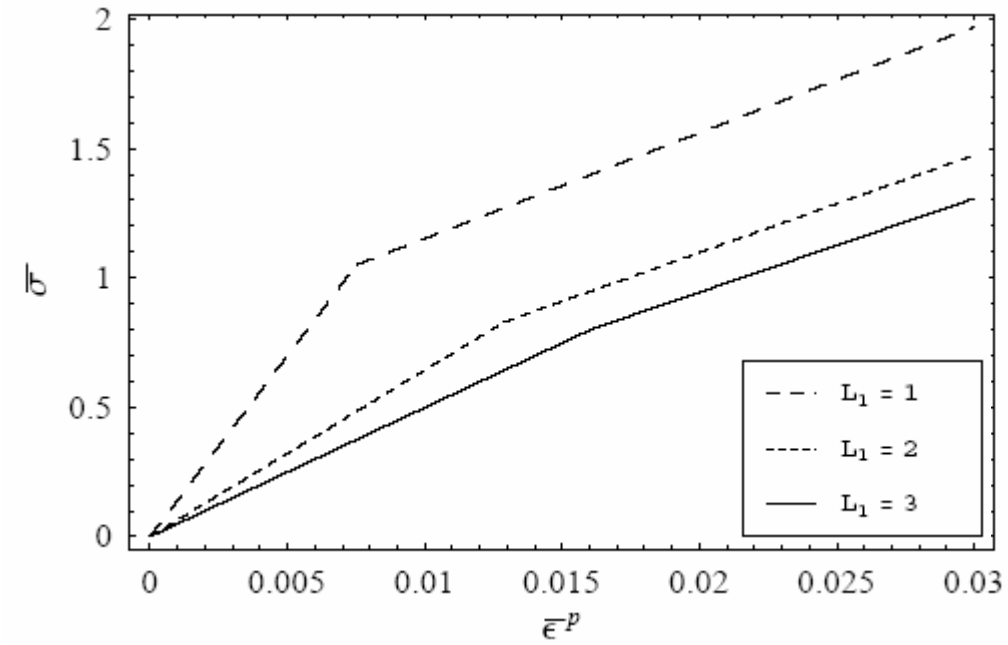

Fig. 6.1: Interfacial yield point and size effects nonlinear interfacial energy obtained through the comparison method

Direct comparison of Figs 4.3&6.1 shows that the comparison solution

produces the same stress-strain response as the exact solution of the differential equations, and its use is hence justified for two-phase media as well.

All of the results in the remainder of this section are obtained by substituting the appropriate realization of the constants of β^{eff} in (6.11) and then in (6.2) and optimizing numerically with respect to the material parameters β_1, β_2. The material parameters are defined as $\sigma_0^1 = 1$, $\sigma_0^2 = 2$, e_o=1, γ=2, and $L_2 / L_1 = 3/2$. In particular, inserting (6.4) in (6.11) and then in (6.2) allows the determination of the effective response for a highly nonlinear heterogeneous periodic medium, with different internal lengths in each phase. It should be noted that in the case of the new-gradient dependent potential the scaled internal length (5.12) must be used. Letting $\ell_1 = 1$ and $\ell_2 = 3/2$ provides Figs. 6.2 and 6.3. For illustration purposes the results obtained through use of the Fleck-Willis potential (smooth curves) and the new gradient dependent plastic potential (dotted curves) are plotted together.

It can be seen from Figs. 6.2 and 6.3 that unlike for the homogeneous medium, for this heterogeneous composite the new-gradient potential does not exhibit greater size effects from that used by Fleck and Willis. Therefore in the sequel only the Fleck-Willis potential will be employed.

The curve designated as lower bound in the following figures indicates the elementary Reuss bound and is given by the expression

$$V^{eff}(\bar{\varepsilon}^p) \geq \frac{\sigma_R e_0}{n+1}\left(\frac{\bar{\varepsilon}^p}{e_0}\right)^{n+1}, \tag{6.13}$$

where

$$\sigma_R = \{p_1 \sigma_1^{-1/n} + p_2 \sigma_2^{-1/n}\}^{-n}. \tag{6.14}$$

It should be noted that (6.13) corresponds physically to the limiting case $L_1 / \ell \to \infty$.

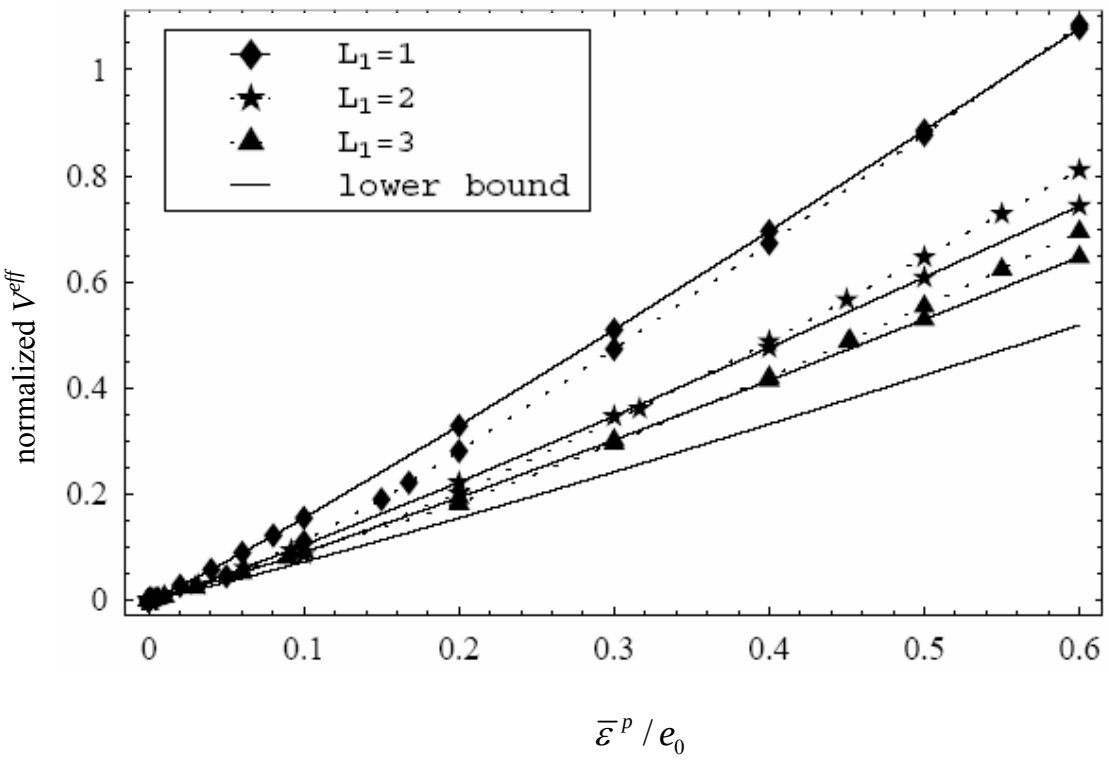

Fig.6.2: Comparison between F-W and new gradient potential, when n=0.1 for a two phase periodic medium; smooth curves: F-W, dotted curves: new potential

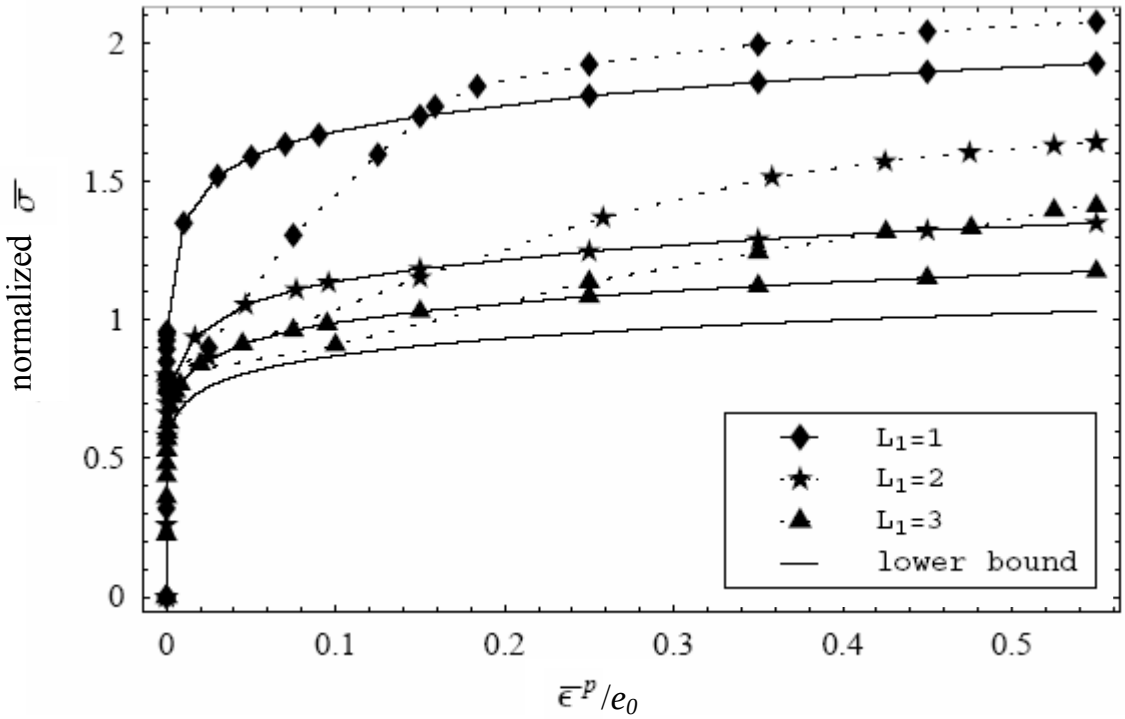

Fig. 6.3: Comparison between F-W and new gradient potential, when n=0.1 for a two phase periodic medium; smooth curves: F-W, dotted curves: new potential

To examine how the approximation of having the same internal length in both phases relates to the more physical case of having separate internal lengths in each phase, (6.6) is inserted in (6.11) and then in (6.2). The material parameters are kept the same, except that now there are two limiting cases that can be considered. The approximate internal length ℓ can be equal to either the smallest or largest of the actual internal lengths, ℓ_1, ℓ_2. In Fig. 6.4 therefore $\ell = \ell_2 = 1.5$, while in Fig. 6.5 $\ell = \ell_1 = 1$. For comparison reasons the solution with different internal lengths (dotted curves) is also shown in these figures.

It is illustrated in Fig. 6.4 that when the approximate internal length is set equal to the largest of the actual internal lengths, the response of the material becomes stiffer.

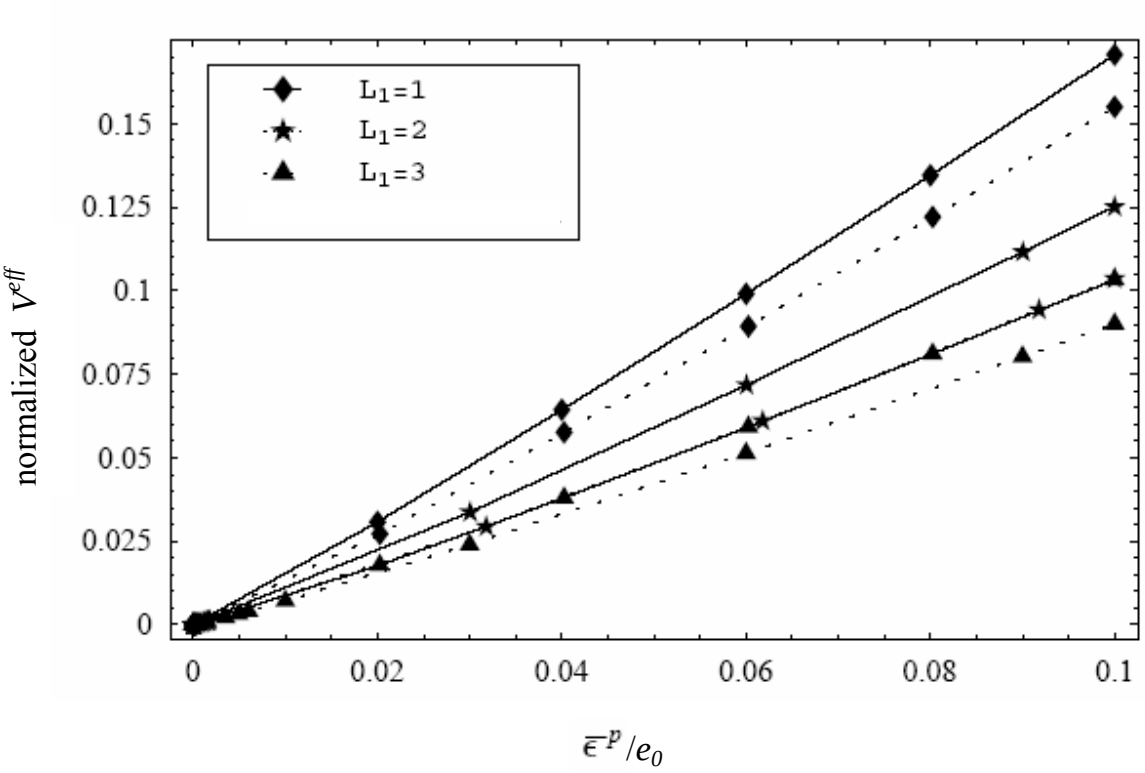

Fig. 6.4: Comparison of solutions obtained for F-W potential with *n*=0.1, *when* a) $\ell_1 = 1, \ell_2 = 1.5$: dotted *curves b)* $\ell = \ell_2 = 1.5$: smooth curves

For the case however where ℓ is set equal to the smallest of the actual internal lengths in each phase, i.e. ℓ_1 in this particular example, the actual

solution (in which $\ell_1 \neq \ell_2$) and the simplified solution ($\ell = \text{constant} = \ell_1$) are in remarkable close proximity, as shown in Fig. 6.5. This argument can be used as a valid justification for employing the constant internal length assumption when solving the heterogeneous random medium; it should be noted however that the approximate internal length must correspond to the smallest actual internal length in order for the assumed solution to be robust.

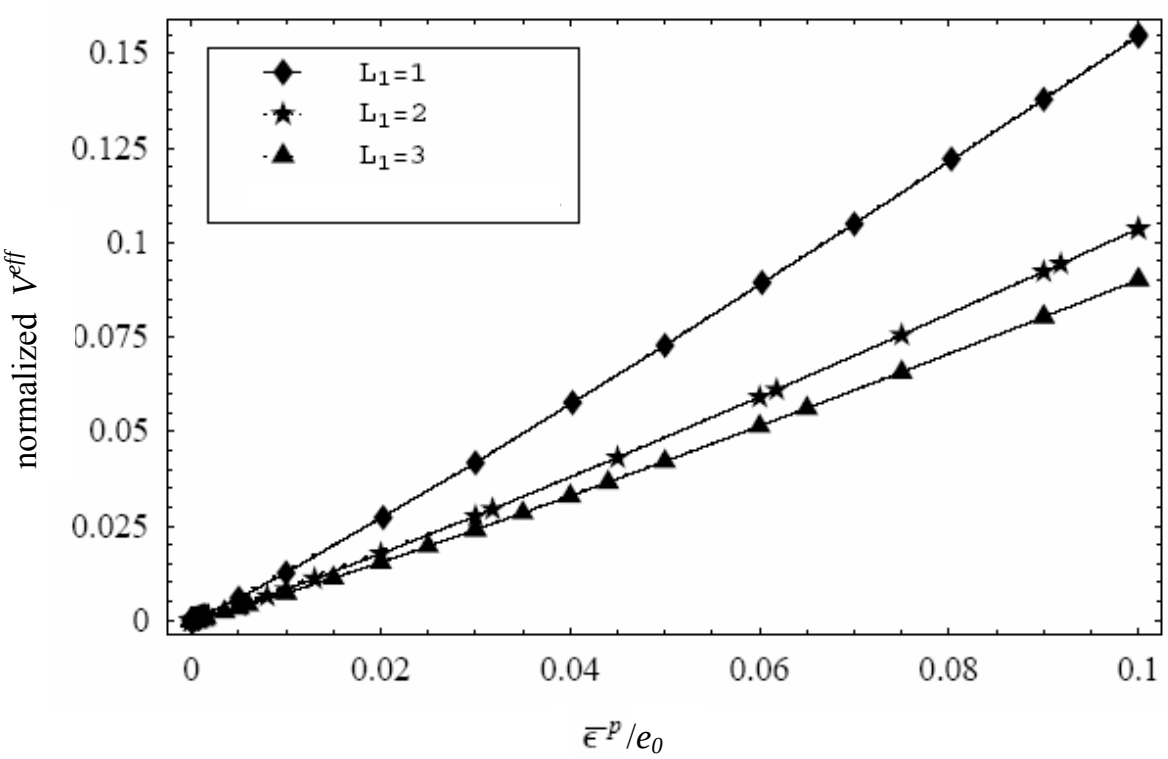

Fig. 6.5: Comparison of solutions obtained for F-W potential with *n*=0.1, *when* a) $\ell_1 = 1, \ell_2 = 1.5$: dotted *curves b)* $\ell = \ell_1 = 1$: smooth curves

Fig. 6.6 displays the response for the same periodic medium as Fig. 6.5, but with a higher hardening exponent; the assumption $\ell = \text{constant} = \ell_1$ is considered so a comparison can be made with the random two-phase media solutions that are shown in Figs. 6.8&6.9 (i.e. (6.9), is inserted in (6.11), which is in turn inserted in (6.2) and minimized); Fig. 6.9, is the counterpart of Fig. 6.6.

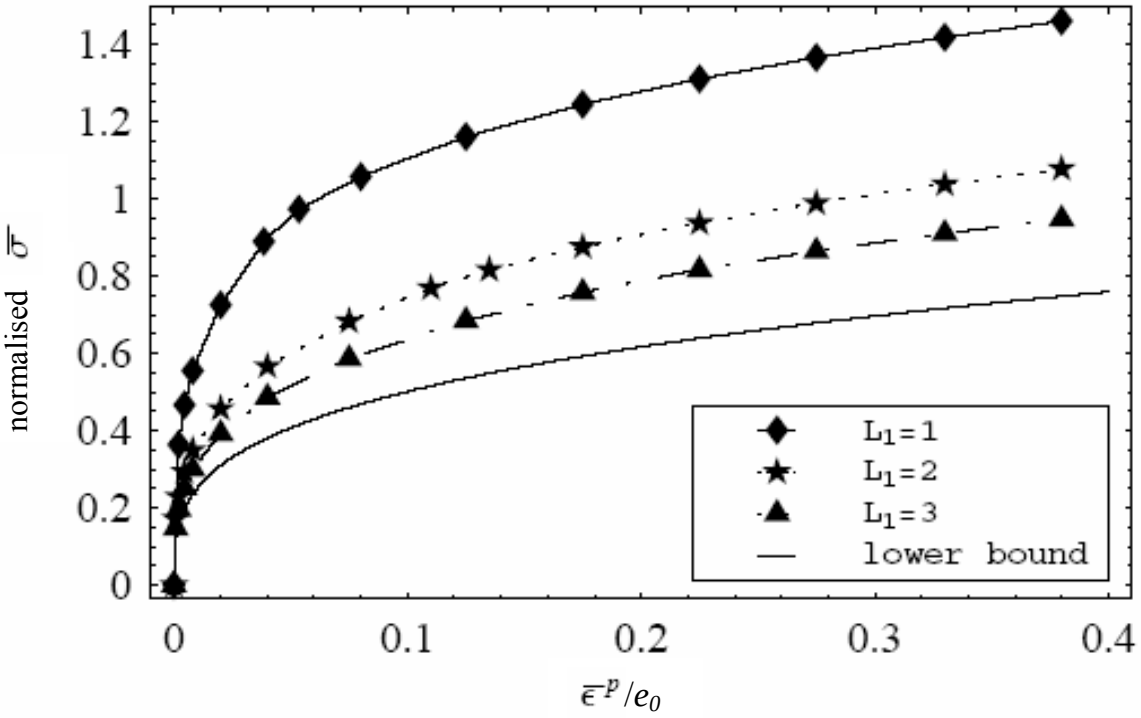

Fig. 6.6: Size effects for a two-phase periodic medium with F-W potential when n=0.3

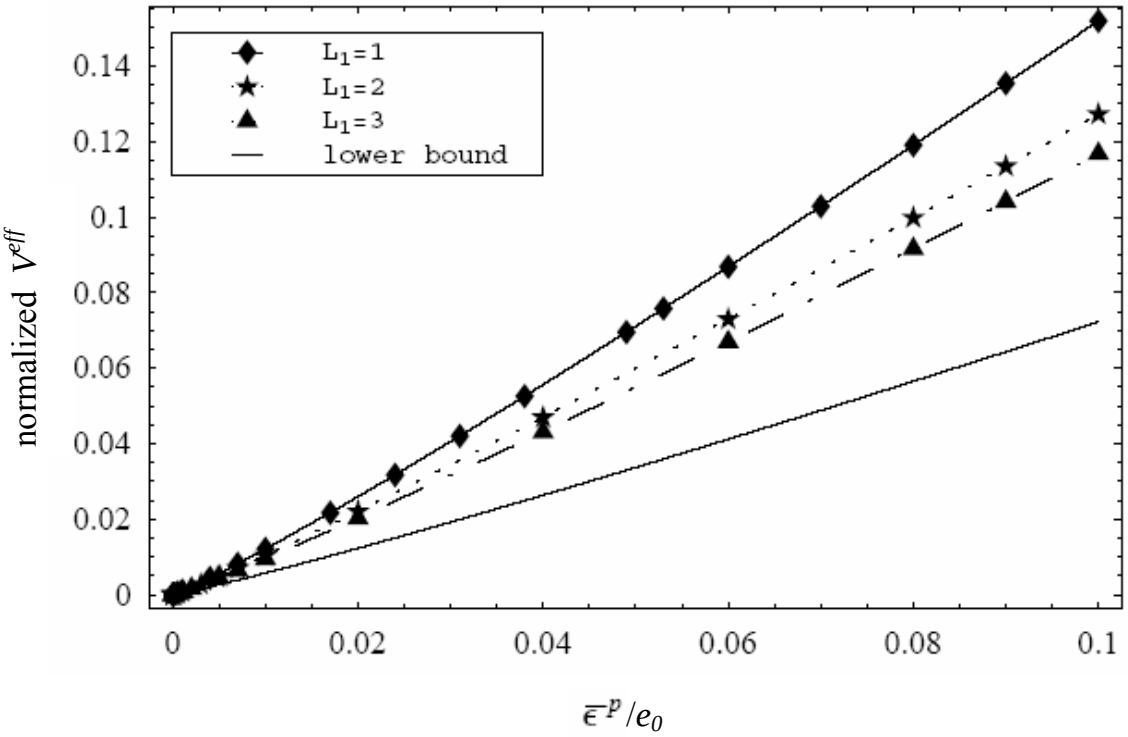

Fig. 6.7:Two-phase random medium, for F-W potential when n=0.1

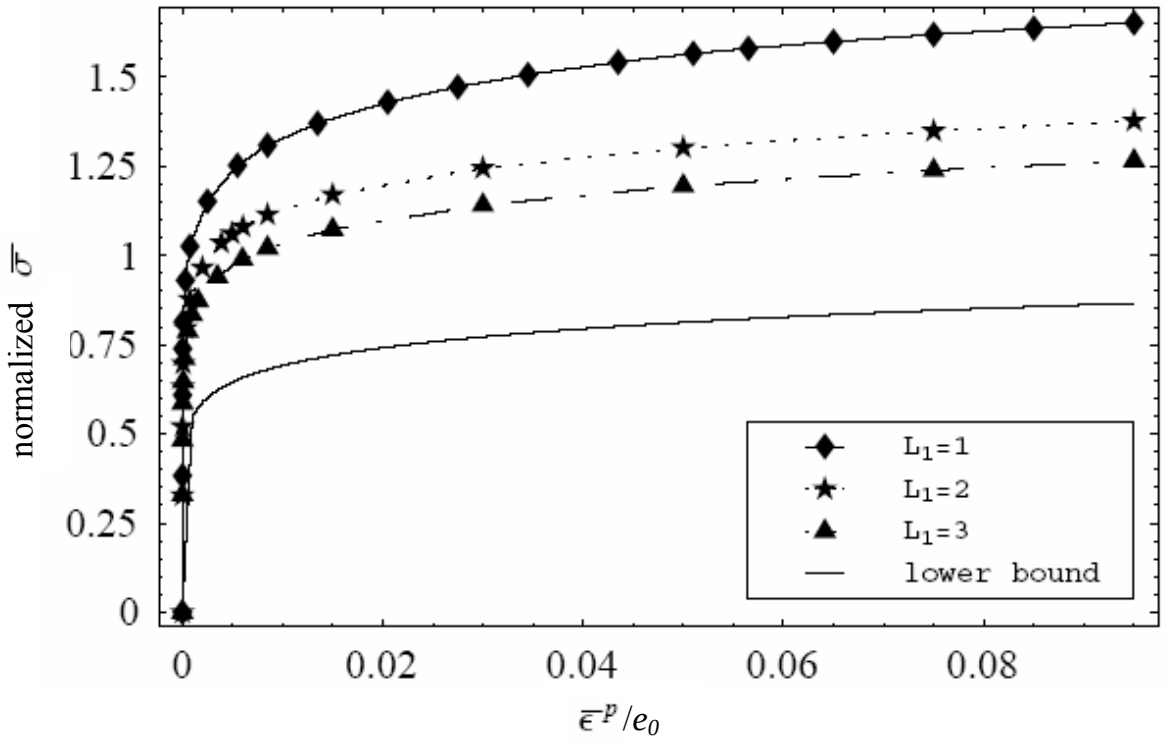

Fig. 6.8: Size effects for a two-phase random medium, for F-W potential, n=0.1

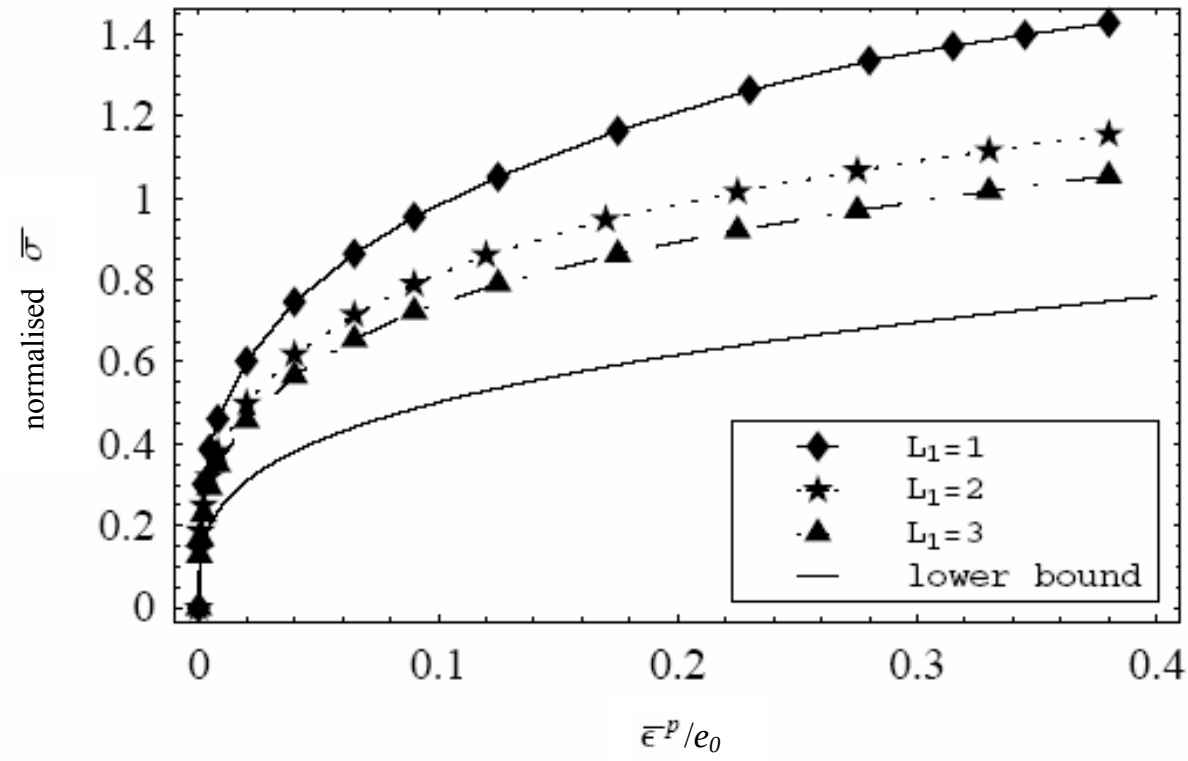

Fig. 6.9: Size effects for a two-phase random medium with F-W potential when n=0.3

It is observed in the above figures that the close numerical proximity that existed for the periodic and random homogeneous media is now present only for the largest specimen size. In particular it is seen in Fig. 6.10 that, in general, the disorder increases the strength of the material. This may be due to the randomness of the phases and not to the random interface distribution. The similarity between both materials for the largest specimen size considered is strikingly similar.

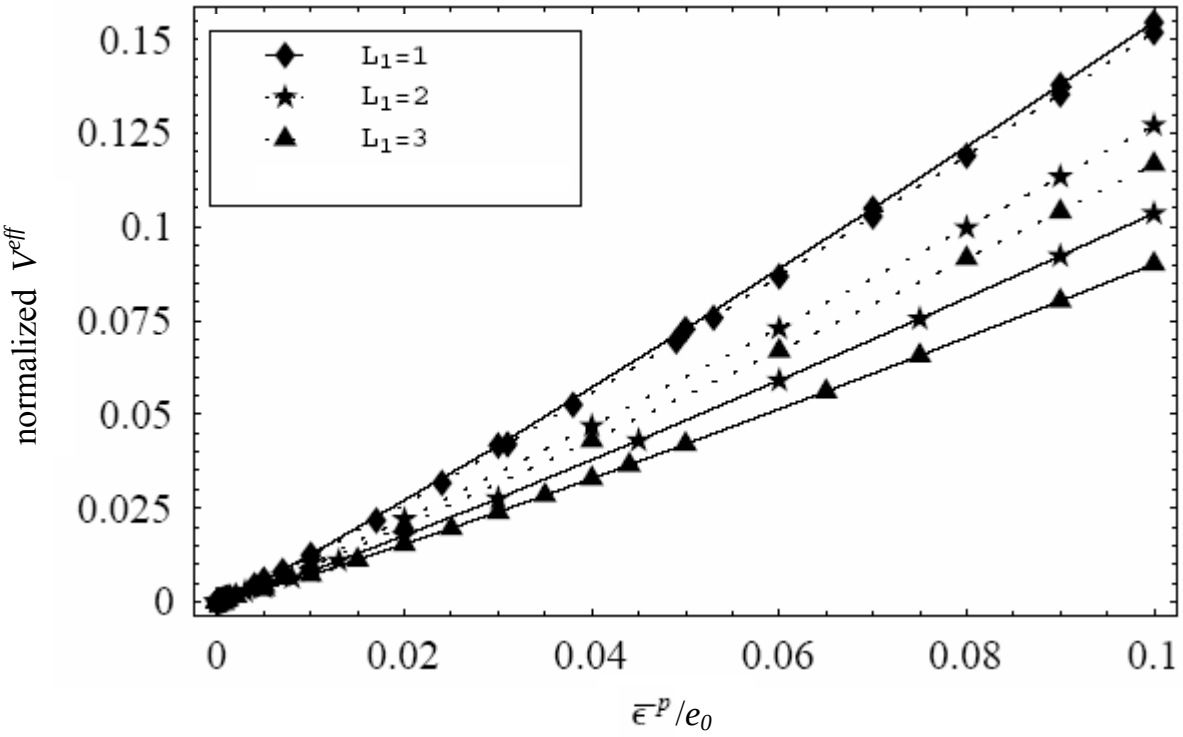

Fig. 6.10: Comparison between periodic and random media with F-W potential, when n=0.1;dotted curves: random medium; smooth curves: periodic medium

Finally, to illustrate the significant role of the "interfacial energy" in the observed size effects, Fig. 6.11 for the random material is obtained by setting γ=0. It can be seen that the scale effects are not only very small, but they lie between definite upper and lower bounds. This result can also be obtained through direct application of the Fleck-Willis [7] theory, and hence illustrates the limitation of that formulation, and the need to consider interfaces explicitly.

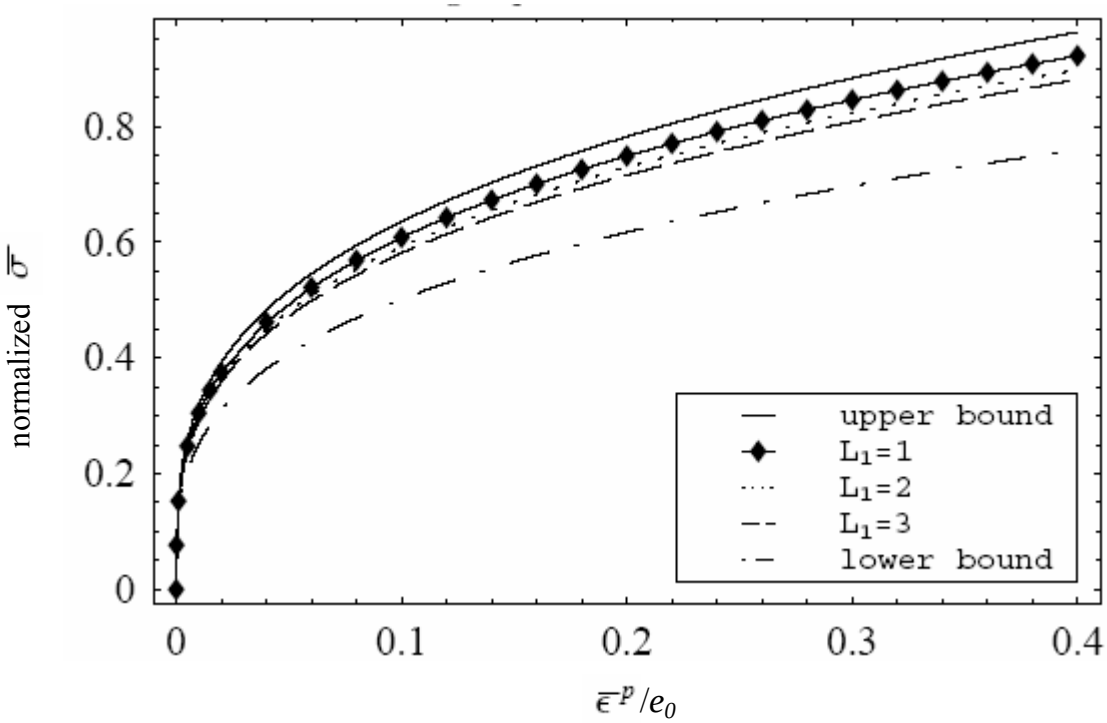

Fig. 6.11: Two-phase random medium with γ=0 (as in Fleck-Willis) and n=03

CHAPTER 7

THREE-DIMENSIONAL CONFIGURATION

The one-dimensional examples considered thus far, have been very effective in illustrating the main features of the newly developed variational formulation of Chapter 3. The purpose of the present chapter is to consider a more physical, three-dimensional, situation such as a metal fiber embedded in a metal matrix. Such material systems are currently in an experimental stage and therefore the following formulation is promising for future applications. It will be shown that although similar size-effects are observed in higher dimensions, analytical expressions for the material response cannot be obtained, even if all potentials are linear. Incompressibility is assumed for the elastic and plastic strains; therefore the variational principle of Chapter 3, must be slightly modified so as account for these constraints.

7.1 VARIATIONAL FORMULATION

The overall potential Ψ is defined as in Chapter 3, i.e.

$$\Psi(\varepsilon_{ij}, \varepsilon_{ij}^P) = \int_\Omega U(\varepsilon_{ij}, \varepsilon_{ij}^P, \varepsilon_{ij,k}^P)\, d\Omega + \int_\Gamma \phi(\varepsilon_{ij}^P)\, d\Gamma \,. \qquad (7.1a)$$

For complete incompressibility the elastic stiffness tensor L_{ijkl} which contains both Lame constants (λ and μ) is simplified so as to account only for the shear component, hence U takes the form

$$U(\varepsilon_{ij}, \varepsilon_{ij}^{P}, \varepsilon_{ij,k}^{P}) \equiv \mu(\varepsilon_{ij} - \varepsilon_{ij}^{P})(\varepsilon_{kl} - \varepsilon_{kl}^{P}) + V(\varepsilon_{ij}^{P}, \varepsilon_{ij,k}^{P}). \tag{7.1b}$$

It follows that since this definition for U differs from that in Chapter 3, the conjugate variable expressions must also be different; i.e. since U accounts only for the shearing component of L_{ijkl} differentiation of this elastoplastic potential with respect to ε_{ij}, ε_{ij}^{p} and $\varepsilon_{ij,k}^{p}$ provides the deviatoric components of the Cauchy stress, "back" stress and hyperstress. Hence the conjugate variable expressions that will be used in the sequel take the form

$$\sigma'_{ij} = \frac{\partial U}{\partial \varepsilon_{ij}}, s'_{ij} = \frac{\partial U}{\partial \varepsilon_{ij}^{p}}, \text{and } \tau'_{ijk} = \frac{\partial U}{\partial \varepsilon_{ij,k}^{p}}. \tag{7.2}$$

The general variational characterization of U^{eff} is the same as before

$$U^{eff}(\overline{\varepsilon}_{ij}, \overline{\varepsilon}_{ij}^{p}) \equiv \inf_{\varepsilon_{ij}, \varepsilon_{ij}^{p}} \left\{ \frac{1}{|D|} \left[\int_{D} U(\varepsilon_{ij}, \varepsilon_{ij}^{p}, \varepsilon_{ij,k}^{p})\, dx + \int_{\Gamma_D} \phi(\varepsilon_{ij}^{p})\, d\Gamma \right] \right\}, \tag{7.3}$$

and is minimized over fields with mean values

$$\left\langle \varepsilon_{ij} \right\rangle \equiv \frac{1}{|D|} \int_{D} \varepsilon_{ij}\, dx = \overline{\varepsilon}_{ij}, \tag{7.4}$$

$$\left\langle \varepsilon_{ij}^{p} \right\rangle \equiv \frac{1}{|D|} \int_{D} \varepsilon_{ij}^{p}\, dx = \overline{\varepsilon}_{ij}^{p}. \tag{7.5}$$

Now the first variation of (7.1a) is set equal to zero so as to obtain the principle of virtual work; allowing for complete incompressibility (i.e. $\varepsilon_{ii} = 0$ and $\varepsilon_{ii}^{p} = 0$) and using the definitions of (7.2) provides

$$\int_{\Omega} \left\{ (\sigma'_{ij} - p\delta_{ij} - \overline{\sigma}'_{ij}) \delta\varepsilon_{ij} + (s'_{ij} - q\delta_{ij} + s^{*}_{ij}) \delta\varepsilon_{ij}^{P} + (\tau'_{ijk} - r_k \delta_{ij})\, \delta\varepsilon_{ij,k}^{P} \right\} dx$$
$$+ \int_{\Gamma_D} [\partial\phi / \partial\varepsilon_{ij}^{P} - t\delta_{ij}] \delta\varepsilon_{ij}^{P} d\Gamma = 0, \tag{7.6}$$

where the constant tensors $\bar{\sigma}'_{ij}, s^*_{ij}$, and the fields r_k, p, q, t, play the role of Lagrage multipliers. It can be seen that subsequent integration by parts gives

$$\int_\Omega \left\{(-\sigma'_{ij,j}+p_{,i})\delta u_i+(s'_{ij}-q\delta_{ij}-s^*_{ij}-\tau'_{ijk,k}+r_{k,k}\delta_{ij})\,\delta\varepsilon^P_{ij}\right\}dx$$
$$+\int_{\partial D}\left\{((\sigma_{ij}-\bar{\sigma}_{ij})n_j-pn_i)\delta u_i+(\tau'_{ijk}n_k-r_kn_k\delta_{ij})\delta\varepsilon^P_{ij}\right\}dS$$
$$+\int_{\Gamma_D}\left\{[\sigma'_{ij}n_j-pn_i]\delta u_i+(\phi'(\varepsilon^P_{ij})-t\delta_{ij}-[\tau'_{ijk}n_k-r_kn_k\delta_{ij}])\delta\varepsilon^P_{ij}\right\}d\Gamma=0. \quad (7.7)$$

Hence, the equilibrium, boundary, and jump across interfaces conditions, for the case of complete incompressibility read

$$\left.\begin{aligned}\sigma'_{ij,j}-p_{,i}&=0\\ s'_{ij}-q\delta_{ij}-s^*_{ij}-\tau'_{ijk,k}+r_{k,k}\delta_{ij}&=0\end{aligned}\right\}\ \text{in D}\backslash\Gamma, \quad (7.8)$$

$$\left.\begin{aligned}(\sigma'_{ij}-\bar{\sigma}'_{ij})n_j-pn_i&=0\\ \tau'_{ijk}n_k-r_kn_k\delta_{ij}&=0\ \text{ on }\partial\Omega\end{aligned}\right\}\ \text{on }\partial\text{D}, \quad (7.9)$$

$$\left.\begin{aligned}[\sigma'_{ij}n_j-pn_i]&=0\\ [\tau'_{ijk}n_k-r_kn_k\delta_{ij}]&=\phi(\varepsilon^p_{ij})-t\delta_{ij}\end{aligned}\right\}\text{across }\Gamma_D. \quad (7.10)$$

In this connection, it should be noted that according to classical mechanics, the total stress, under complete incompressibility is expressed as

$$\sigma_{ij}=\sigma'_{ij}-p\delta_{ij}. \quad (7.11)$$

Furthermore for this particular form of U the quantities q, r_k and t can be set equal to zero, without affecting the general solution, therefore s_{ij} and τ_{ijk} are equal to their deviatoric part, and hence all of the above equilibrium conditions, with the exception of $(7.8)_1$, reduce to (3.22-3.24).

7.2 Application To Two-Phase Axially Symmetric Composite

The cylindrical composite under consideration is taken to be under a state of uniaxial stress. The load is applied on the axis of symmetry (z-axis), such that the

average strain in the *z* direction is taken to be a constant and is set equal to $\bar{\varepsilon}_{zz}$; therefore the present configuration is under generalized plane strain conditions. In particular for axially symmetric generalized plane strain, the stress and displacement equilibrium equations, as well as the general strain and displacement relations are given by

$$\frac{d\sigma_{rr}}{dr}+\frac{\sigma_{rr}+\sigma_{\theta\theta}}{r}=0,\ \text{and}\ \frac{d\sigma_{zz}}{dr}=0\Rightarrow\sigma_{zz}=\sigma_{zz}(r), \tag{7.12}$$

$$u_r=u_r(r),\ u_\theta=0,\ \text{and}\ u_z=\bar{\varepsilon}_{zz}z\ , \tag{7.13}$$

$$\varepsilon_r=\frac{du_r}{dr},\ \varepsilon_\theta=\frac{u_r}{r},\ \text{and}\ \varepsilon_z=\bar{\varepsilon}_{zz}\ ; \tag{7.14}$$

the rest of the components vanish due to symmetry. Inserting now (7.14) in the total strain incompressibility condition gives the displacement relation as

$$\varepsilon_{rr}+\varepsilon_{\theta\theta}+\varepsilon_{zz}=0\Rightarrow\frac{du_r}{dr}+\frac{u_r}{r}+\bar{\varepsilon}_{zz}=0\Rightarrow u_r(r)=\frac{A}{r}-\frac{r}{2}\bar{\varepsilon}_{zz}, \tag{7.15}$$

where the constant of integration *A* has to be zero inside the inclusion in order to avoid a singularity at $r=0$. Moreover, due to continuity of u_r across interfaces, *A*=0 also inside the matrix and hence the displacement expression is the same throughout the whole composite.

It follows from (7.14) and (7.15) that

$$\varepsilon_r=\varepsilon_\theta=-\frac{\bar{\varepsilon}_{zz}}{2}\ . \tag{7.16}$$

To proceed further towards the formulation of the problem, *V* assumes its aforementioned quadratic form

$$V(\varepsilon_{ij}^p,\varepsilon_{ij,k}^p)=\frac{1}{2}\beta_i[(\varepsilon_{ij}^p)^2+\ell_i^2(\varepsilon_{ij,k}^P)^2]\,. \tag{7.17}$$

As a result the conjugate variable expressions give

$$\sigma'_{ij}=2\mu_i(\varepsilon_{ij}-\varepsilon_{ij}^p), \tag{7.18}$$

$$s'_{ij}=\beta_i\varepsilon_{ij}^p-\sigma'_{ij}, \tag{7.19}$$

$$\tau'_{ijk} = \beta_i \ell_i^2 \varepsilon^p_{ij,k} \,. \tag{7.20}$$

Substituting (7.18) in (7.11) gives the total stress as

$$\sigma_{ij} = -p\delta_{ij} + 2\mu_i(\varepsilon_{ij} - \varepsilon^p_{ij}) \,. \tag{7.21}$$

Hence the governing differential equation, $(7.8)_2$, of the system can be re-written as

$$\sigma_{ij} + p + \beta_i \ell_i^2 \varepsilon^p_{ij,kk} = \beta_i \varepsilon^p_{ij} \,. \tag{7.22}$$

It should be noted that, due to the axial symmetry present, the only relevant components of (7.22) are the *rr*, $\theta\theta$, and *zz*, only two of which are independent. Computing the *zz*-component of (7.21) and (7.22), and combination of the two provides the first independent differential equation of the system

$$2\mu(\bar{\varepsilon}_{zz} - \varepsilon^p_{zz}) + \beta_i \ell_i^2 \left(\frac{d^2 \varepsilon^p_{zz}}{dr^2} + \frac{1}{r}\frac{d\varepsilon^p_{zz}}{dr} \right) = \beta_i \varepsilon^p_{zz} \,, \tag{7.23}$$

where it should be emphasized that the gradient of the plastic strain in (7.22) is computed for cylindrical co-ordinates under axial symmetry. Solution of (7.23) gives the plastic strain in the *z* direction as

$$\varepsilon^p_{zz} = \frac{2\mu_i}{\beta_i + 2\mu_i}\bar{\varepsilon}_{zz} + C_1^i I_0(kr) + C_2^i K_0(k_i r), \text{ where } k_i = \sqrt{\frac{\beta_i + 2\mu_i}{\beta_i \ell_i^2}} \,. \tag{7.24}$$

The subscripts/superscripts *i* in the constants of (7.24) as well as in the sections to follow denote the properties in the inclusion (which is denoted as 1) and the matrix (denoted by 2). Now, (7.21) is calculated for the *rr* and $\theta\theta$ components and the resulting expressions are subtracted to give

$$\sigma_{rr} - \sigma_{\theta\theta} = 2\mu_i(2\varepsilon^p_{rr} - \varepsilon^p_{zz}) \,. \tag{7.25}$$

Similarly by calculating (7.23) for the *rr* and $\theta\theta$ components, and subtracting the resulting expressions we obtain the second differential equation of the system

$$\sigma_{rr} - \sigma_{\theta\theta} + \beta_i \ell_i^2 [(\nabla \varepsilon^p)_r - (\nabla \varepsilon^p)_\theta] = \beta_i (\varepsilon^p_{rr} - \varepsilon^p_{\theta\theta}) \,. \tag{7.26}$$

It follows that insertion of (7.25) in (7.26) provides

$$2\varepsilon_{rr}^{p}+\varepsilon_{zz}^{p}=C_3^i I_2(kr)+C_4^i K_2(k_i r)\Rightarrow \varepsilon_{rr}^{p}=\frac{1}{2}(C_3^i I_2(kr)+C_4^i K_2(k_i r)-C_1^i I_0(kr)+C_2^i K_0(k_i r))$$

$$\Rightarrow \varepsilon_{\theta\theta}^{p}=-\varepsilon_{rr}^{p}. \quad (7.27)$$

Additionally substitution of (7.25) in (7.12) gives

$$\sigma_{rr}(r)=-\frac{2\mu_i}{k_i r}\left(C_3^i(k_i r-2I_1(k_i r))/2+C_4^i K_1(k_i r)\right)+j_i\,, \quad (7.28)$$

where the integration constant j_2 is found by setting $\sigma_{rr}(b)=0$, while j_1 is found by requiring continuity of the stress, i.e. $\sigma_{rr}^{1}(a)=\sigma_{rr}^{2}(a)$; hence j_1= j_2=0.

Writing the *rr*-component of (7.21) and combining with (7.28) allows the determination of the pressure *p*

$$p=(C_1^i-C_3^i)\mu_i I_0(k_i r)+\frac{\mu_i}{\beta_i+2\mu_i}(C_3^i(\mu_i+\beta_i)-\beta_i\bar{\varepsilon}_{zz})\,. \quad (7.29)$$

Now the *zz*-component of the stress (7.22) can be completely defined, in terms of the various constants which shall be determined from the boundary conditions, and averaged so as to give the average stress-strain response in the z-direction

$$\bar{\sigma}_{zz}(r)=\frac{2\pi}{\pi b^2}\int_0^b r\sigma_{zz}(r)dr\Rightarrow\bar{\sigma}_{zz}(r)=\frac{2}{b^2}\left[\int_0^a r\sigma_{zz}(r)dr+\int_a^b r\sigma_{zz}(r)dr\right]. \quad (7.30)$$

7.3 DETERMINATION OF CONSTANTS IN THE PLASTIC STRAIN RELATIONS

In order for ε_{zz}^{p} to be nonsingular at *r*=0 it is required to take $C_2^1=0$, similarly $C_4^1=0$ in order for ε_{rr}^{p} and $\varepsilon_{\theta\theta}^{p}$ to be nonsingular. This is because the modified Bessel functions of the second kind (i.e. $K_n(x)$) approach infinity as $r\to 0$, and hence are undefined at *r* = 0. As in the previous examples considered, the higher-order traction is taken to be zero at the outer boundary. Hence,

$$\left.\frac{d\varepsilon_{rr}^{p}}{dr}\right|_{r=b}=0;=\left.\frac{d\varepsilon_{zz}^{p}}{dr}\right|_{r=b}=0; \quad (7.31)$$

the conditions concerning $\varepsilon^p_{\theta\theta}$ are not employed since they are dependent on ε^p_{rr}. The four more equations needed to determine the complete set of constants in the plastic strain expressions, are formulated separately for the two interfacial energy terms that have been used so far.

7.3.1 Linear interfacial response

The first case considered is that according to which the interface has a linear response so

$$\phi \equiv \phi(\varepsilon^p_{ij})\Big|_{x=0} = \frac{1}{2}\alpha\,(\varepsilon^p_{ij})^2\Big|_{x=0} \Rightarrow [\tau] = \phi'(\varepsilon^p_{ij})\Big|_{x=0} = \alpha\varepsilon^p_{ij}\Big|_{x=0}. \qquad (7.32)$$

Therefore the remaining 4 equations are those that ensure continuity of the plastic strains across the interfaces, as well those that allow the higher-order tractions to suffer a jump equal to that of (7.32), in other words

$$\varepsilon^{p,1}_{rr} = \varepsilon^{p,2}_{rr};\ \varepsilon^{p,1}_{zz} = \varepsilon^{p,2}_{zz};$$

$$\beta_2\ell_2^2\frac{d\varepsilon^{p,2}_{rr}}{dr}\Big|_a - \beta_1\ell_1^2\frac{d\varepsilon^{p,1}_{rr}}{dr}\Big|_a = \alpha\varepsilon^p_{rr}(0);\ \beta_2\ell_2^2\frac{d\varepsilon^{p,2}_{zz}}{dr}\Big|_a - \beta_1\ell_1^2\frac{d\varepsilon^{p,1}_{zz}}{dr}\Big|_a = \alpha\varepsilon^p_{zz}(0). \qquad (7.33)$$

7.3.2 Non-linear interfacial response

When the nonlinear behavior of the interfaces is considered the interfacial yield condition is given by

$$\phi \equiv \phi(\varepsilon^p_{ij})\Big|_{r=a} = \gamma(\varepsilon^p_{ij}\,\varepsilon^p_{ij})^{1/2}\Big|_{r=a} \Rightarrow$$

$$[\tau_{ijk}n_k] \le \gamma, \text{when } \varepsilon^p_{ij}\Big|_{r=a} = 0$$

$$[\tau_{ijk}n_k] = \gamma\frac{\varepsilon^p_{ij}}{\sqrt{\varepsilon^p_{kl}\varepsilon^p_{kl}}}, \text{when } (\varepsilon^p_{kl}\varepsilon^p_{kl})^{1/2} \neq 0, \qquad (7.34)$$

in particular:

a) Before the interface yields the plastic strain there is zero so

$$\varepsilon^{p,1}_{rr}(a) = 0;\ \varepsilon^{p,2}_{rr}(a) = 0;\ \varepsilon^{p,1}_{zz}(a) = 0;\ \varepsilon^{p,2}_{zz}(a) = 0; \qquad (7.35)$$

b) After the interface yields

$$\varepsilon_{rr}^{p,1} = \varepsilon_{rr}^{p,2}; \varepsilon_{zz}^{p,1} = \varepsilon_{zz}^{p,2};$$

$$\beta_2 \ell_2^2 \left.\frac{d\varepsilon_{rr}^{p,2}}{dr}\right|_a - \beta_1 \ell_1^2 \left.\frac{d\varepsilon_{rr}^{p,1}}{dr}\right|_a = \gamma \frac{\varepsilon_{rr}^p(a)}{\sqrt{(\varepsilon_{rr}^p)^2\big|_{r=a} + (\varepsilon_{\theta\theta}^p)^2\big|_{r=a} + (\varepsilon_{zz}^p)^2\big|_{r=a}}}$$

$$\beta_2 \ell_2^2 \left.\frac{d\varepsilon_{zz}^{p,2}}{dr}\right|_a - \beta_1 \ell_1^2 \left.\frac{d\varepsilon_{zz}^{p,1}}{dr}\right|_a = \gamma \frac{\varepsilon_{zz}^p(a)}{\sqrt{(\varepsilon_{rr}^p)^2\big|_{r=a} + (\varepsilon_{\theta\theta}^p)^2\big|_{r=a} + (\varepsilon_{zz}^p)^2\big|_{r=a}}}. \qquad (7.36)$$

7.3.3 General Solution

Solving the above system of equations provides that for both interfacial energies, in addition to $C_2^1 = 0, C_4^1 = 0$, which was proven at the beginning of this section, $C_3^1 = C_3^2 = C_4^2 = 0$, hence the general average stress-plastic strain response in the z-direction takes the form

$$\bar{\sigma}_{zz}(r) = \frac{3}{b^2}\left\{ a\mu_1 \left(\frac{a\beta_1 \bar{\varepsilon}_{zz}}{\beta_1 + 2\mu_1} - \frac{2C_1^1 I_1(ak_1)}{k_1} \right) \right.$$
$$\left. + \frac{3\mu_2}{k_2(\beta_2 + 2\mu_2)} \left((b^2 - a^2)k_2 \beta_2 \bar{\varepsilon}_{zz} + 2(\beta_2 + 2\mu_2)[C_1^2(aI_1(ak_2) - bI_1(bk_2)) + C_2^2(bK_1(bk_2) - aK_1(ak_2))] \right) \right\}, \qquad (7.37)$$

where the appropriate set of constants are considered depending on the assumed interfacial energy.

7.4 Results For Axially Symmetric Configuration

7.4.1 Linear interfacial response

For the linear interfacial energy the overall stress-strain response of the material is linear and the constants in (7.37) can be grouped together as

$$\bar{\sigma}_{zz}(r) = \frac{3}{2}\beta^{eff}\bar{\varepsilon}_{zz}^p. \qquad (7.38)$$

where again β^{eff} can be written in the form

$$\beta^{eff} = \frac{A + B/\alpha}{C + D/\alpha}\ , \tag{7.39}$$

in which

$$A = A_1(\hat{\alpha}/\alpha);\ B = A_1 + B_1;\ C = \hat{\alpha}/\alpha;\ D = 1\,; \tag{7.40}$$

the constants A_1, B_1 and $\hat{\alpha}$ are given in Appendix E, and are found by solving simultaneously the system of equations that consists of (7.31) and (7.33) . It should be noted that the factor $3/2$ in (7.38) accounts for the incompressible, three-dimensional configuration, at hand.

Allowing for the material parameters to take the values $\beta_1 = 1, \beta_2 = 2, \mu_1 = 3, \mu_2 = 2, \ell_1 = 1, \ell_2 = 1.5, \alpha = 1.2$ provides the size effects shown in Fig. 7.1.

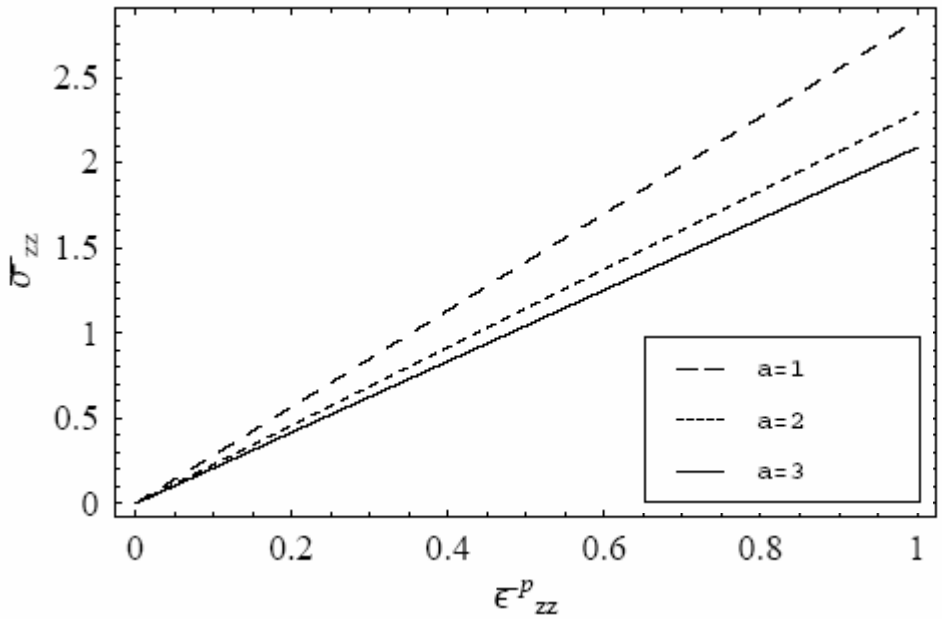

Fig. 7.1: Size effects for an axially symmetric composite with linear V and ϕ

7.4.2 Non-linear interfacial response

Solving the system of equations prior to interfacial yield (i.e. (7.31) and (7.35)) provides that the constants required for defining the average stress-strain response (7.37), prior to interfacial yielding are given by

$$C_1^1 = \frac{3\mu_1 \bar{\varepsilon}_{zz}}{(-\beta_1 - 2\mu_1) I_0(ak_1)}; \quad C_1^2 = \frac{2\mu_2 K_1(bk_2)\bar{\varepsilon}_{zz}}{(-\beta_2 - 2\mu_2)[I_1(bk_2)K_0(ak_2) + I_0(ak_2)K_1(bk_2)]}$$

$$C_2^2 = \frac{I_1(bk_2)}{K_1(bk_2)} C_1^2 . \tag{7.41}$$

After the interface yields solution of $(7.31)_2$ and $(7.36)_2$ provides analytical expressions for two of the three constants as

$$C_1^2 = \frac{[(\beta_2/(\beta_2 + 2\mu_2) - \beta_1/(\beta_1 + 2\mu_1))\bar{\varepsilon}_{zz} + I_0(ak_1)C_1^1]K_1(bk_2)}{I_1(bk_2)K_0(ak_2) + I_0(ak_2)K_1(bk_2)} \text{ and } C_2^2 = \frac{C_1^2 I_1(bk_2)}{K_1(bk_2)}. \tag{7.42}$$

The remaining constant, C_1^1, is found numerically from the interfacial jump condition, $(7.36)_4$. Allowing for the same material parameters as in the previous subsection, i.e. $\beta_1 = 1, \beta_2 = 2, \mu_1 = 3, \mu_2 = 2, \ell_1 = 1, \ell_2 = 1.5, \gamma = 1.2$, where α has been replaced with γ, provides Fig. 7.2.

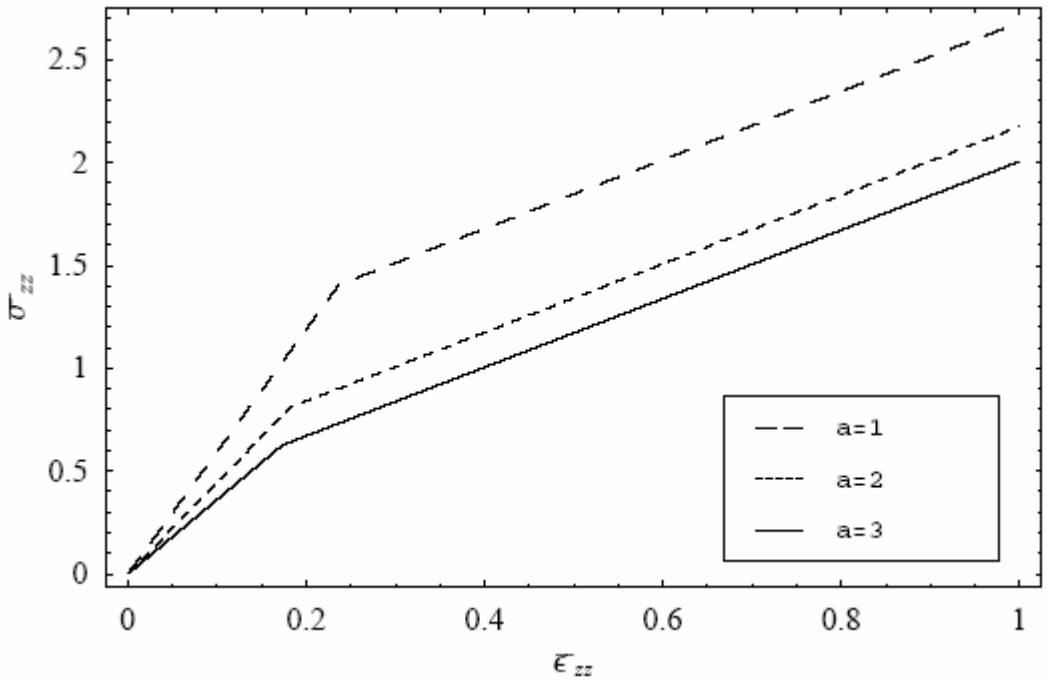

Fig. 7.2: Size effects for an axially symmetric composite with linear V and nonlinear ϕ

It can be seen that the exhibited size effects are similar to those of its one dimensional counterpart (Fig. 4.3); it should be noted, however, that now the

strain at which the interface yields increases as the specimen size decreases, whereas the opposite was observed in Fig. 4.3. A significant drawback for this three dimensional, axial configuration is that it does not allow the development of an analytical expression for the "interfacial yield" stress, since the constant C_1^1 needs to be found numerically. This will be true for all configurations in higher dimensions.

It should be noted that the bound formulations of Chapter 3, including the comparison method, were developed based on the assumption that the elastic constants L_{ijkl} are the same throughout the whole domain under consideration, (see expression (3.27)). These bounds are valid for a medium which constitutes of phases that have different elastic constants, only in the special one-dimensional case. Therefore, it was possible to apply the comparison method to the heterogeneous one-dimensional examples of Chapter 6. For this axial three-dimensional configuration the comparison method, as displayed in Chapter 3 can be used only if the inclusion and surrounding matrix have the same shear moduli; such a material system, however, does not have much physical relevance and therefore is not examined herein. It should be noted, however, that since β^{eff} (7.39) for this system is of the same form as that in Chapter 6, the corresponding effective response, in the case of constant μ, for a highly nonlinear medium, i.e. its gradient dependent plastic potential assumes the form of (4.20) or (4.24) is given by inserting (6.11) in (6.2). Due to the three-dimensional incompressibility conditions that are present, the constants A and C should be scaled by the factor 3/2. Additionally the probabilities, for the present case, are given as $p_1=a^2/b^2$ and $p_2=(b^2-a^2)/b^2$.

For the more interesting case of different shear moduli, which was solved exactly for a quadratic V in the previous subsections, a V^{eff} does not exist and therefore the comparison method produces a bound for U^{eff}, which depends on both the total and plastic strain, in addition to the material parameters α, β_1 and β_2. Illustration of this approach is beyond the scope of this chapter, whose main

purpose was to demonstrate how a configuration with direct physical application should be treated.

CHAPTER 8

EXPERIMENTAL CONFIRMATION OF THEORETICAL FORMULATION

The previous chapters were concerned with the development and applications of an appealing mathematical framework, which accounts explicitly for the presence of interfaces in composites and polycrystals. The main new features of this novel formulation are: interfaces are allowed to follow their own yield behavior and hence an "interfacial yield" stress is present, and size effects which are in some cases solely due to the presence of the interfacial penalty are observed. The purpose of this final chapter is to confirm through experimental observations the existence of such an "interfacial yield" stress, as well as the occurrence of corresponding size effects. The experiments were performed through nano-indentation, hence a brief introduction is first given on this subject. Then, after the experimental results are presented and analyzed they are fit to the analytical one-dimensional interfacial yield stress expression that was obtained in Chapter 4. This allows us to obtain qualitative values for the main physical parameters, the internal length and the interfacial energy-like term, that are present in the theory. This is of particular interest since these are the first estimates of their type, and they are proven to be in good agreement with quantities deduced through dislocation mechanics.

8.1. NANO-INDENTATION

In the past two decades, significant focus has been given towards the development of experimental techniques for characterizing the mechanical properties of thin films and small volumes of material. Load and depth sensing indentation, commonly referred to as nano-indentation, is a way by which this has been achieved [70]. A detailed analysis of the technique of nano-indentation can be found in the PhD thesis of Nuno Carvalho [71] on which the present summary is based. It should be realized that the material properties that can be probed with this technique depend on the indenter tip geometry. The most common categories of tip geometries are: spherical, cube triangular, and cube corner. In general, sharp, geometrically-similar indenters such as the Berkovich triangular pyramid are useful when one wishes to probe properties at the smallest possible scale. This tip is often preferred over the Vicker's (cube corner) for hardness measurements because the apex can be more readily fashioned to meet at a point rather than the inevitable line that occurs with the Vickers four-sided geometry. Moreover, it has no major flaws and is easier to calibrate. Therefore, the force/area relationship can be reliably calculated at very low loads. Spherical indenters are usually employed by ultra-low load indentation methods [72].

The properties routinely measured with the Berkovich indenter are the hardness and the elastic modulus [73]; additionally, methods which are still in a first stage, are also available for measuring strain rate sensitivity, and internal friction [74]. When the specimen temperature can be controlled, it is also possible to determine parameters characteristic of thermally-activated plastic flow, such as the activation energy and stress exponent for creep [75]. The experiments to be presented are based on hardness measurements; hence the techniques followed to obtained such data is presented in the sequel.

In order to determine the hardness and elastic properties of a material using load and depth sensing indentation techniques, several methods have been developed [73,76-78]. One of the important advantages of these methods is that it is not necessary to measure the area of the hardness impression by imaging, thereby facilitating property measurements at the sub-micron scale. The contact area and the mechanical properties are determined from the data of one complete cycle of loading and unloading. The unloading data is treated assuming that the displacement recovered is largely elastic. Then, the hardness and Young's modulus can be determined by solving the elastic contact problem [79].

The mathematical foundations for the contact problem of indentation of an elastic half-space by a rigid punch were considered more than a century ago by Boussinesq [80] and Hertz [81]. Later, Love used elasticity methods to derive solutions for cylindrical [82a] and conical [82b] punches. However, a complete solution for the contact problem was only derived in 1945 by Sneddon [83], who established an analytical procedure based on Fourier transforms for obtaining the relationships of load, displacement, and contact area for a punch of arbitrary axisymmetric shape. His results show that the load-displacement relationships for simple punch geometries can be expressed as

$$P = \alpha h^m , \tag{8.1}$$

where P is the indenter load, h is the total elastic displacement of the indenter, m is 1, 1.5, and 2 for a flat cylindrical punch, parabola of rotation, and cone, respectively, and α is a constant. Stillwell and Tabor [84] performed the earliest experiments in which load and displacement sensing indentations by conical indenters were used to measure mechanical properties. Their experiments revealed that upon unloading the shape of the hardness impression was still conical, and only the depth had recovered, resulting in a larger included tip angle. Therefore, the elastic contact solutions could be applied and the plasticity

accounted, by taking into consideration the shape of the deformed surface. With these results, they demonstrated that the elastic modulus and the size of the contact impression could be derived accurately from the shape of the unloading curve (of the load vs. depth plot) and the total amount of recovered displacement.

Another key development was the definition of the reduced modulus, which includes the effects of non-rigid indenters on the load-displacement behavior, via the equation*

$$\frac{1}{E_r} = \frac{(1-\nu^2)}{E} + \frac{(1-\nu_i^2)}{E_i}, \tag{8.2}$$

where E and ν are the Young's modulus and Poisson's ratio, respectively, for the specimen while E_i and ν_i are the corresponding quantities of the indenter. The first experiments to obtain load-displacement data which could be used to measure the elastic modulus, were done by Bulychev and co-workers [85] using a microhardness testing apparatus. They analyzed the data according to the equation

$$S = \frac{dP}{dh} = \frac{2}{\sqrt{\pi}} E_r \sqrt{A}, \tag{8.3}$$

where S is the stiffness in the contact between the indenter and the specimen, i.e. the slope of the upper portion of the unloading data, and A is the projected area of the elastic contact area measured from the indentation hardness impression. Eq. (8.3) has its origins in the elastic contact theory [86]. Although it was originally derived for a conical indenter, Bulychev et al. [85] showed that the equation could be applied for spherical and cylindrical indenters. Subsequently, Pharr et al [79] showed that (8.3) applies to any indenter that can be described as a body of revolution of a smooth function. Moreover, King [87] using a finite element method, showed that when (8.3) is rewritten as

* The origin of this equation can be traced back to Hertz's analysis

$$S = \frac{2}{\sqrt{\pi}} \beta E_r \sqrt{A}\,, \tag{8.4}$$

it can be applied to indenter geometries which are not described as bodies of revolution, like flat-ended punches with square (Vickers-like) and triangular (Berkovich-like) cross sections, providing β is taken to be 1.012 and 1.034, respectively.

In the late 1980's Doerner and Nix [78] presented a method to determine the hardness and modulus from load-displacement data using (8.3). They recognized that for most metals, during initial unloading the area in contact with the indenter remains constant. Accordingly, the elastic behavior could be modeled as that of a blunt punch indenting, over the contact area, an elastic solid. To evaluate the contact area independently, they proposed to extrapolate the initial part of the unloading curve to zero load and determine the extrapolated depth. Then, using the indenter shape function, the contact area can be calculated. Knowing the contact area, the hardness, H, which is equivalent to the average pressure under the indenter, is calculated from

$$H = \frac{P^{max}}{A}\,, \tag{8.5}$$

where P^{max} is the maximum load.

Oliver and Pharr [73] have developed a procedure that accounts for the elastic recovery by expanding the assumptions developed by Loubet et al [77] and Doerner and Nix [78], without assuming a flat punch geometry. The method expresses the load-displacement relation derived by Sneddon [86], for purely elastic material the more general form by

$$P = \alpha (h - h_f)^m\,, \tag{8.6}$$

where the total displacement is now modified for the indenter impression; h_f is the final displacement after complete unloading, as shown schematically in Fig. 7.1a, and α, m are constants. A drawback of the analysis proposed by Oliver and Pharr [73] is that the suggested power law relationship does not take into

account any residual plasticity present in an elastic/plastic material. Their analysis procedure begins by rewriting (8.4) as

$$E_r = \frac{1}{\beta}\frac{\sqrt{\pi}}{2}\frac{S}{\sqrt{A}}, \tag{8.7}$$

which relates the reduced modulus, E_r, to the contact area, A, and the measured stiffness, S. Then, the unloading curve is fitted to the power-law relation of (8.6), where α, m and h_f are empirically determined fitting parameters. The unloading stiffness is subsequently obtained by differentiating the load-displacement relation at the maximum depth of indentation, $h = h_{max}$, leading to:

$$S = \frac{dP}{dh}(h = h_{max}) = m\alpha(h_{max} - h_f)^{m-1}. \tag{8.8}$$

The depth along which contact is made between the indenter and the specimen, called contact depth, h_c, is also estimated from the load-displacement data through the relationship

$$h_c = h_{max} - \varepsilon\frac{P_{max}}{S}, \tag{8.9}$$

where the parameter ε depends on the indenter geometry, being $\varepsilon = 0.72$ for a conical indenter, $\varepsilon = 0.75$ for the Berkovich tip and $\varepsilon = 1$ for a flat punch. Fig. 8.1 depicts the cross section of an indentation and a schematic load-displacement curve, where all the parameters used in the analysis are identified. The indenter area function, A, is calculated using the unloading curve and based on the assumption that the elastic modulus is independent of the indentation depth, while the compliance of the specimen, C_S, and additional machine compliance, C_f, can be modeled as a two springs system in series. Taking the specimen compliance during elastic contact as the inverse of the contact stiffness, the contact area can be described by rewriting (8.3) as

$$A = \frac{\pi}{4}\frac{1}{E_r^2}\frac{1}{(C - C_f)^2}, \tag{8.10}$$

where C is the total measured compliance, $(C = C_S + C_f)$.

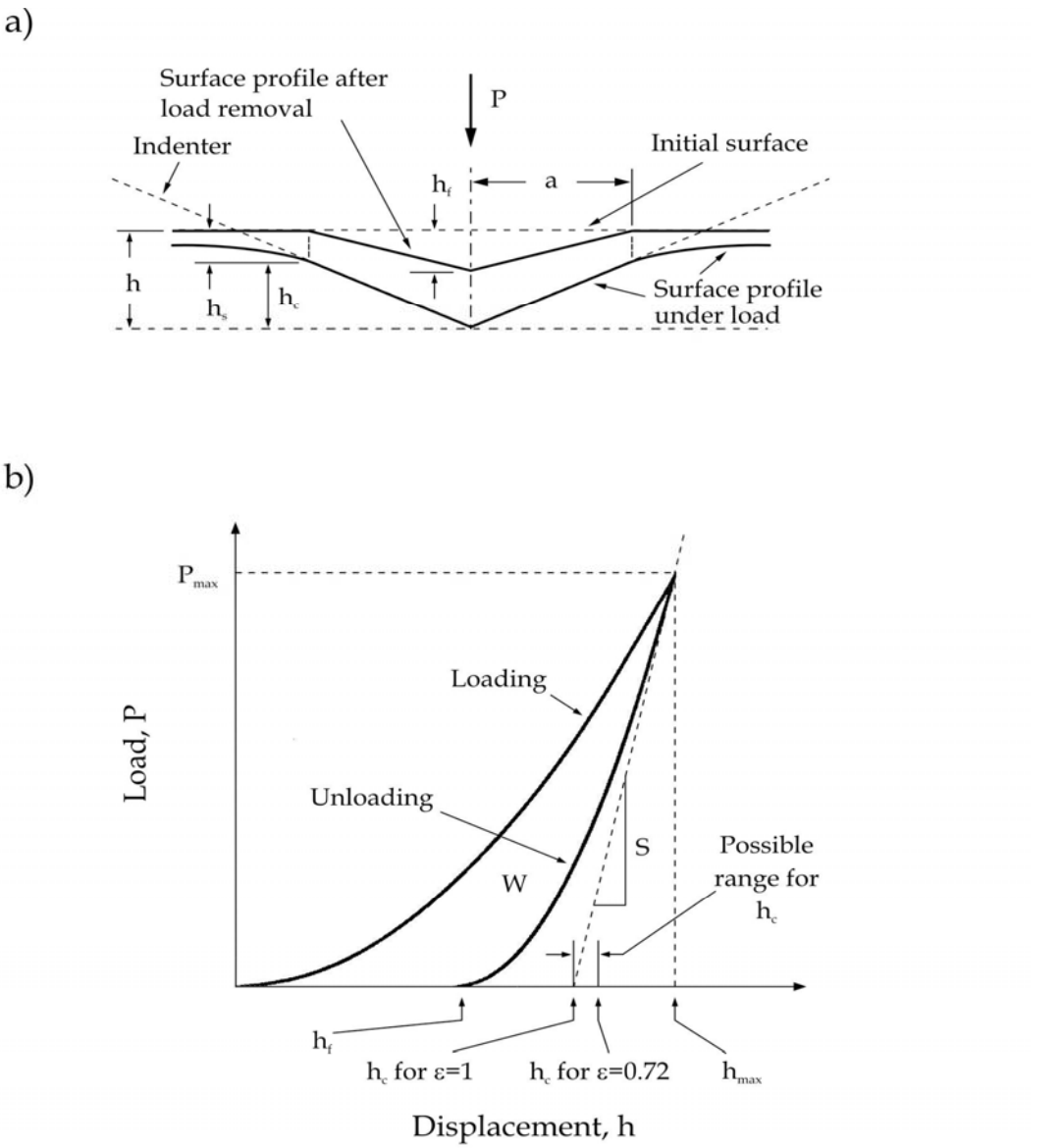

Fig. 8.1: Schematic representations of: a) a cross section of an indentation and b) the load versus indenter displacement curve, showing the quantities in the analysis, as well as a graphical interpretation of the contact depth [71]

The first estimate of the contact area is made for large indentations, by applying the indenter shape function for a perfect Berkovich indenter at the contact depth, which is given by

$$\begin{aligned} A(h_c) &= 3\sqrt{3}\,h_c^2 \tan^2\theta \\ &= 24.56\,h_c^2, \end{aligned} \tag{8.11}$$

where θ is the indenter included half-angle of 65.3°. Assuming that the large indentations are unaffected by tip rounding, the initial values of the elastic modulus and machine compliance are obtained by plotting C *vs* $A^{-1/2}$, where if the modulus is constant, the plot is linear and the intercept a direct measure of C_f. However, for real Berkovich indenters the shape function is far more complex due to tip rounding.

Therefore, the contact area is now calculated for different indentation depths in a material with well-known, isotropic elastic properties (usually fused quartz), and plotted vs the corresponding contact depths. The resulting graph is fitted to a nine-term polynomial, and the new values of the machine compliance are then calculated by using the obtained area function and the procedure is repeated until convergence occurs and the indenter shape function is deduced. Then, the contact area can be determined from the load-displacement data, and the hardness and reduced modulus are calculated from (8.5) and (8.7), respectively.

With a state-of-the-art instrument and a careful analysis, the mechanical properties (i.e. hardness and elastic modulus) of several materials can be measured using this method with accuracies better than 10% [73]. There are, however, some materials in which the methodology can lead to a significant overestimate of the hardness and modulus due to an underestimate of the true contact area when large amount of pile-up forms around the residual impression. The underestimate of the contact area occurs because (8.7) and (8.9) were derived from a purely elastic contact solution, and thus may not work well for elastic/plastic indentation. In the former situation, the material around the indenter always sinks-in, while in the latter the material may either sink-in or pile-up. Therefore, it is not surprising that the method has been found to work well for hard ceramics, in which sink-in predominates [73], but one may expect errors when the method is applied to soft metals that exhibit extensive pile-up [88].

A method of characterizing materials for pile-up and the types in which it is important have been developed in detail by Bolshakov et al. [88-90] by using a finite element method. From a purely mechanical viewpoint, the fundamental material parameters controlling elastic/plastic deformation during indentation are the elastic constants, E and ν, the yield stress, σ_y, and the work-hardening rate, η. However, a convenient, experimentally measurable parameter can be used to identify the expected indentation behavior of a given material. This parameter is the ratio of the final indentation depth to the displacement at peak load, h_f/h_{max}, which is independent of the indenter penetration due to the self-similar geometry of the conical indenter.

The pile-up or sink-in behavior depends on the amount of work hardening, as well as on the value of h_f/h_{max}. Specifically, the pile-up is large only when $h_f/h_{max} \approx 1$ and the amount of work hardening is small. Nevertheless, when $h_f/h_{max} < 0.7$, very little pile-up is present, irrespectively of the work hardening behavior of the material. The Oliver and Pharr method is based on an elastic analysis, which can account for sink-in only. Therefore, the accuracy of the method in estimating the real contact area depends on the amount of pile-up. Furthermore, when $h_f/h_{max} > 0.7$, the accuracy of the method relies strongly on the work-hardening characteristic of the material. If the material does not work harden, the method underestimates the contact areas by as much as 60%. On the other hand, the contact areas for materials with a large amount of work hardening are predicted very well by the method. At this point it should be noted that from an experimental point of view, it is not possible to predict whether a material work-hardens based solely on load-displacement data. Conversely, when the pile-up is small i.e., $h_f/h_{max} < 0.7$, the method gives a good estimate of the contact area, independently of the work hardening behavior. As hardness values are obtained for a given material using (8.5), inaccuracies in the contact area caused by not accounting for pile-up leads to similar inaccuracies in

the hardness. The problem of overestimation of the elastic modulus was addressed by Hay et. al.[91].

8.2 "Interfacial Yielding" Observations

Another area in which nano-indentation has been very effective is in observing the occurrence of dislocation motion. This is exhibited as a plateau in the load-depth curve, i.e. since dislocations begin to move, the tip can be displaced deeper into the sample at a constant load. Extensive research has been performed for the explanation of such displacement bursts, as they are commonly referred to; it has been argued that they indicate the initiation of plastic flow in the material and hence information for yield stress can be obtained. Recent nano-indentations on a Fe-14%Si bicrystal [34], show that indenting near the grain boundary results in a second displacement burst in the load-depth curve, and is believed to indicate dislocation transference across the boundary. This phenomenon can also be thought of as corresponding to the existence of an "interfacial yield" stress which the aforementioned theory, developed at the previous chapters, predicts. Before relating the experimental observations to the theory some details concerning the experimental procedure are given.

8.2.1 Experimental procedure

As previously mentioned, the indentations were carried out near an isolated and well-defined edge-on grain boundary of a Fe-14wt%Si alloy bicrystal (courtesy Dr. Pavel Lejcek of the Institute of Physics, Czech Republic for providing the Fe-Si bicrystal). After the surface was polished using a final polishing colloidal silica suspension, Electron Backscatter Diffraction (EBSD) was employed to locate the grain boundary with respect to a grid of marker indents. Additionally, the EBSD analysis provided the boundary misorientation, which is represented by a (-0.293, 0.120, 0.026) Rodrigues vector and does not correspond to any low-index

coincident site lattice (CSL) boundary in body-centered cubic crystallography. The indenter tip employed was a pyramidal Berkovich tip and the measurements were performed using the continuous stiffness measurement (CSM) technique [77]. In order to vary the distance to the grain boundary with the smallest possible increments, lines of indentations were drawn across the grain boundary at very low angles (<3^o). The azimuthal orientation of the indenter was chosen to have one side of the triangular impression of the Berkovich tip parallel to the boundary. The maximum indentation depth was 200 nm and the spacing between indentations was 3 μm. To exclude the possibility of mutual interaction between the plastically deformed zones of subsequent indentations, we compared lines of indents with spacings ranging from 3 to 10 μm in the matrix of the bicrystal; no significant deviations in the load - displacement data and the calculated hardness values were found.

8.2.2 Experimental Observations

At relatively small depths all indentations exhibited a displacement burst, which indicates material yielding (e.g. Fig. 8.2). The indents that were close to the boundary exhibited a second plateau as shown in Fig. 8.3a. In particular, some indentations near the boundary exhibited two plateaus, Fig. 8.3b. It may be possible for example that part of the first dislocation batch which began moving was absorbed by the boundary, then as the load increased a second dislocation batch began moving.

Examining Figs 8.2 with 8.3a, respectively, shows that there is quite an amount of extra plasticity stored near the grain-boundary as compared with the bulk behavior. This is better demonstrated by plotting the two figures together in Fig. 8.4.

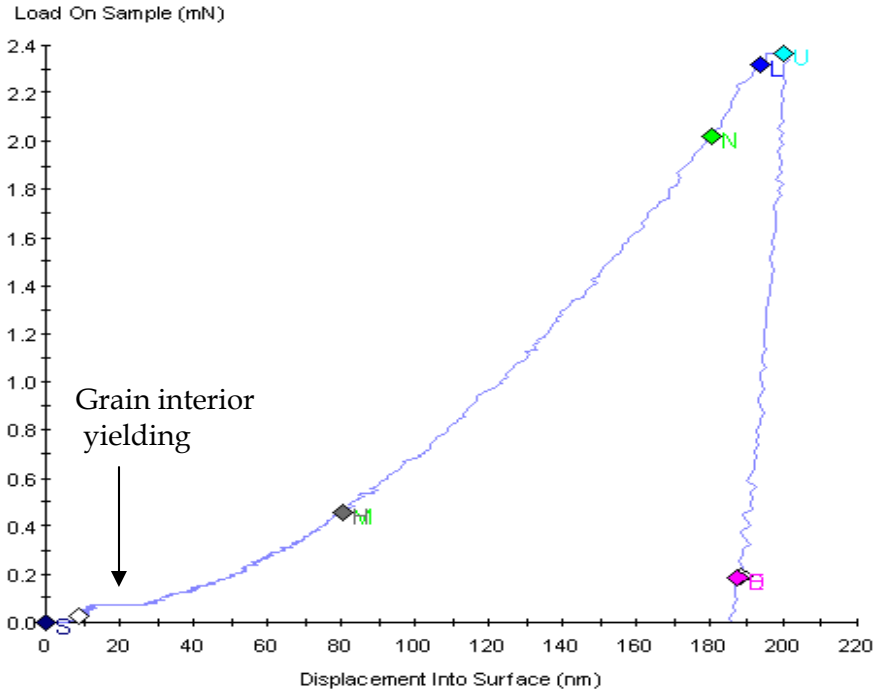

Fig. 8.2: Indentations in the bulk

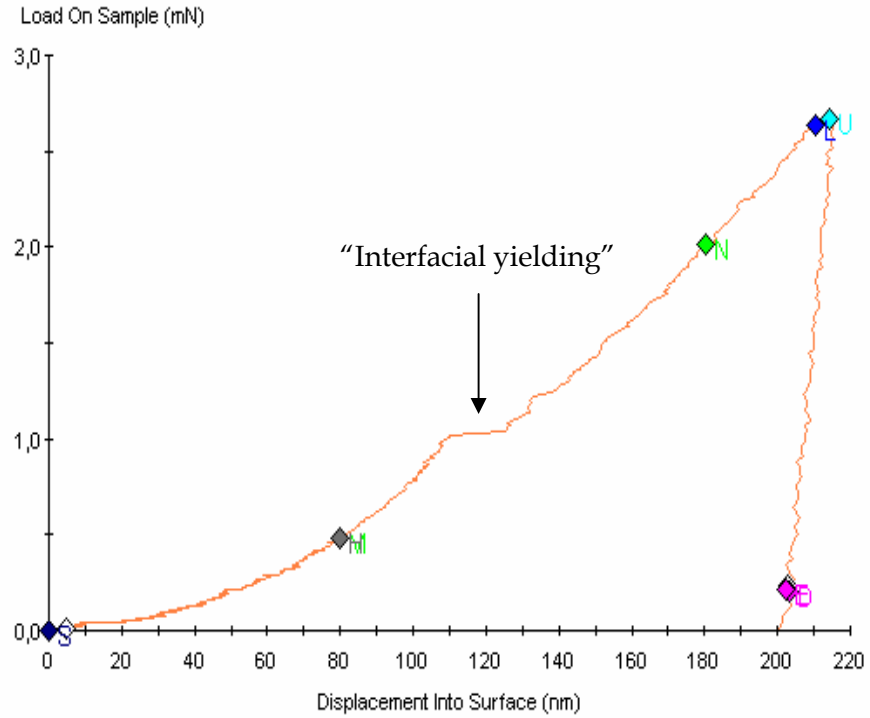

Fig. 8.3a: Indentations near the interface

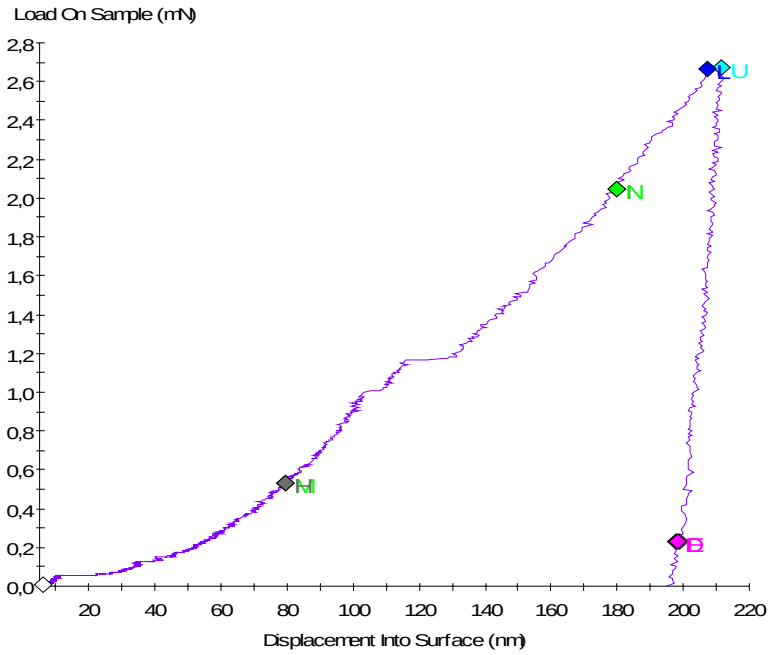

Fig. 8.3b: Indentations near the interface, exhibiting two displacement bursts

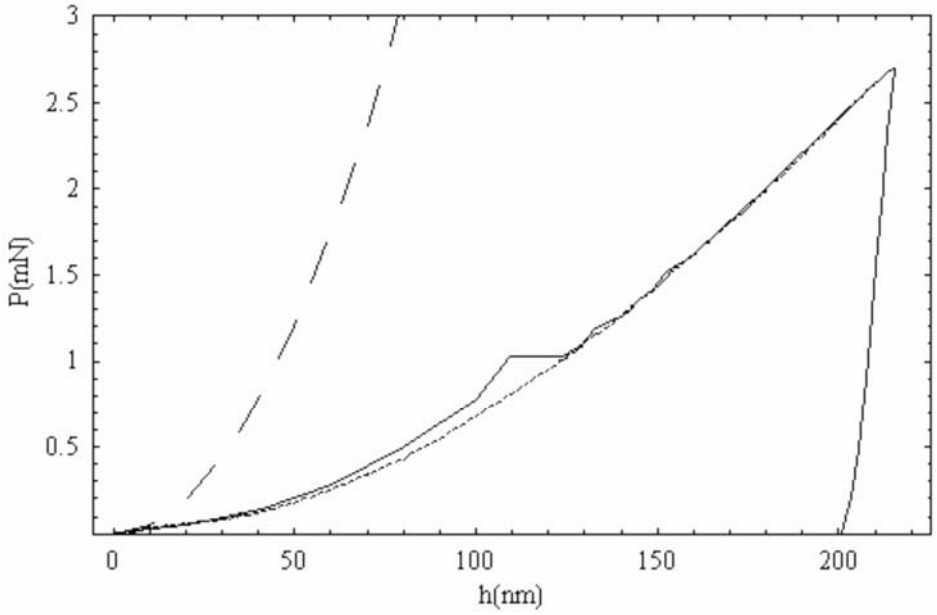

Fig.8.4: Experimental observations and elastic solution of the Berkovich indenter (dashed line); Solid line: bi-crystal near grain-boundary; dotted line: bulk behavior far away from grain-boundary

In particular, it can be seen from Fig.8.4 that by subtracting the $(P \text{ vs } h)_{bulk}$ curve from the $(P \text{ vs } h)_{GB}$ up to the burst, the excess stored energy is found to be $W_{GB}= 8\ 10^{-12}$ J.

It is of interest to investigate whether this amount of energy is related to a dislocation based mechanism. It is not meant, of course, to reproduce the value of W_{GB} exactly but to examine the order of magnitude of the various interactions involved. Let us assume that a dislocation pile-up experiences an applied shear stress as given by the experiment (about 600 MPa); the applied shear stress at the plateau is approximately six times less than the recorded hardness. The length of a dislocation pile-up under an applied shear stress may be estimated from the well-known relationship (e.g. [68])

$$l_{pile-up} = \frac{\mu b n}{\pi \tau_a}, \tag{8.12}$$

where n is the number of dislocation loops in the pile-up, ignoring the difference between edge and screw parts. The distance from the indenter to the GB at the onset of the burst is of the order of 300 nm, and therefore (8.12) gives that n is approximately equal to 25, i.e. there are about 25 dislocations in the pileup. The stress fields of a stressed dislocation pileup of 25 dislocations have been calculated based on linear elasticity and the shear stress is depicted in Fig. 8.5 (the interface is at $x / l_{pile-up} = 0$).

Under an applied shear stress of τ_A the positions of the edge dislocations in the pileup with the first dislocation locked at $x = 0$ are given by:

$$\sum_{i,i\neq j}^{N-1} \frac{\mu b}{2\pi(1-\nu)} \frac{1}{x_j - x_i} + \tau_A = 0\,. \tag{8.13}$$

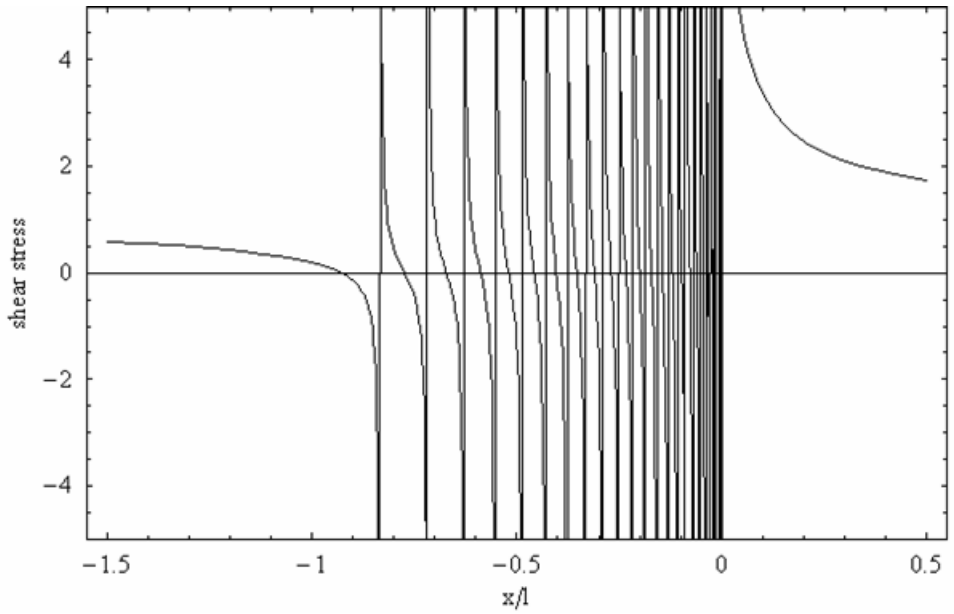

Fig. 8.5: Shear stress due to a dislocation pile-up of 25 dislocations in front of a boundary at $x / l_{pile-up} = 0$ *. The shear stress is in units of the applied shear stress of 600 MPa*

It can be shown that the positions x_i of the dislocations are given by the zeros of the polynomial

$$g(x) = \prod_{i=1}^{N-1} (x - x_i), \tag{8.14}$$

and that $g(x)$ is given by the first derivative of the N-th Laguerre polynomial [93,94]

$$g(x) = L'_N \left(\frac{4\pi(1-\nu)\tau x}{\mu b} \right). \tag{8.15}$$

The calculations provide the position of each of the 25 dislocations with respect to each other, which can be used to compute the total energy of the dislocation burst, i.e. the plateau of Fig. 8.3a. Compared to the experimentally observed length of the burst (= n times the Burgers vector $\vec{b}$) the theoretical prediction is of the same order of magnitude as experimentally observed.

Because the positions of the dislocations in the stressed pile-up are known, the elastic energy stored in the 25 dislocation loops near the spearhead of the pile-up can be predicted from:

$$E_t = \sum_i E_i^{self} + \sum_p \sum_q E^I(r_{pq}) . \qquad (8.16)$$

It turns out that the self energy of the leading 25 dislocation loops of radius 300 nm is far less than the interaction energy among the dislocation loops $\sum_p \sum_q E^I(r_{pq})$, i.e. 5.8 10^{-14} J and 5.1 10^{-12} J, respectively. This was also found in [95] for indentations in thin films. Comparison with the experimentally determined value for W_{GB} of 8 10^{-12} J leads to the conclusion that there is a fair agreement with E_t and that the plateau observed in the *P vs h* curves can be attributed to the release of dislocations in the pile-up in front of the boundary.

In the energy calculations so far we have ignored the increase in elastic energy (see Chapter 2) of the boundary due to the burst. Since in all experimental observations the $(P \text{ vs } h)_{GB}$ returns after the burst to $(P \text{ vs } h)_{\text{bulk}}$ this contribution to the energy change is considered to be small. It is important to realize that the grain-boundary in the bicrystal of the FeSi sample is unconstrained. Suppose 25 dislocations are absorbed in the boundary and relax equidistant over 50 nm. Even in that case, using (2.10) or (2.20) the grain-boundary energy increases only 1.5 10^{-14} J with respect to the misorientation of 35.2^0 in the FeSi, i.e. far less than E_t.

8.3 COMPARISON WITH GRADIENT PLASTICITY THEORY

As was mentioned the dislocation transference phenomenon depicted in Fig.8.2 is similar to the "interfacial yield" that results from the mathematical formulation developed in the previous chapters. It is therefore important to see how the experimental data correspond to the theoretical predictions. As was observed in

the previous chapters, the newly developed strain-gradient formulation predicts that as specimen size decreases, the "interfacial yield" stress increases. It would be therefore interesting to examine if the experimental data follow this pattern. The experimental data obtained are shown in Table 1.

Table 1

Tip to boundary distance at onset of burst (nm)	*Hardness before burst (GPa)*
106	4.25
131	3.7
210	3.2
335	3.17

It can be seen from this table that as the distance from the grain boundary decreases, the hardness of the material before the occurrence of the displacement burst increases. Since, according to the previous section, the burst can be interpreted as the onset of dislocation transference across the grain boundary this hardness can provide the yield stress of the boundary; it has been observed that the yield stress is approximately 1/3 of the hardness. To get a better feeling of how the experimental data behave, the data points of Table 1 are plotted in Figure 8.6. Since the distance between the indenter tip and the grain boundary is bounded between the tip and the boundary, it can be considered as being the specimen size. Fig. 8.4 is of great importance because it not only depicts "size effects" for the "interfacial yield" stress, for the first time, but it is in qualitative agreement with the proposed mathematical formulation, since as the specimen decreases the "interfacial yield" stress increases. It should be noted that no similar dependence was observed for the grain interior yield stress, which remained constant for all indentations performed, regardless of the distance to the grain boundary.

Furthermore, in Section 4.1.2 an analytical expression (4.11) was obtained for the "interfacial yield" stress of a two-phase material that never experienced pure elastic deformation. Since the purely elastic region that was observed in the nano-indentations of the Fe-14%Si bicrystal is almost negligible (see Fig. 8.2 and 8.3), it is reasonable to fit the aforementioned analytical expression to the data of Fig. 8.6. Since the bicrystal at hand is single-phased, (4.11) is modified for a homogeneous material by letting $\ell_1 = \ell_2 = \ell$ and $L_1 = L_2 = L$

$$\bar{\sigma}_c = \frac{\gamma}{2\ell}\coth\left(\frac{L}{\ell}\right). \tag{8.17}$$

Even though (8.17) is derived under one dimensional considerations, without explicitly considering the physics and mechanics that come into play during an indentation, it fits surprisingly well the experimental data, as Fig. 8.6 shows.

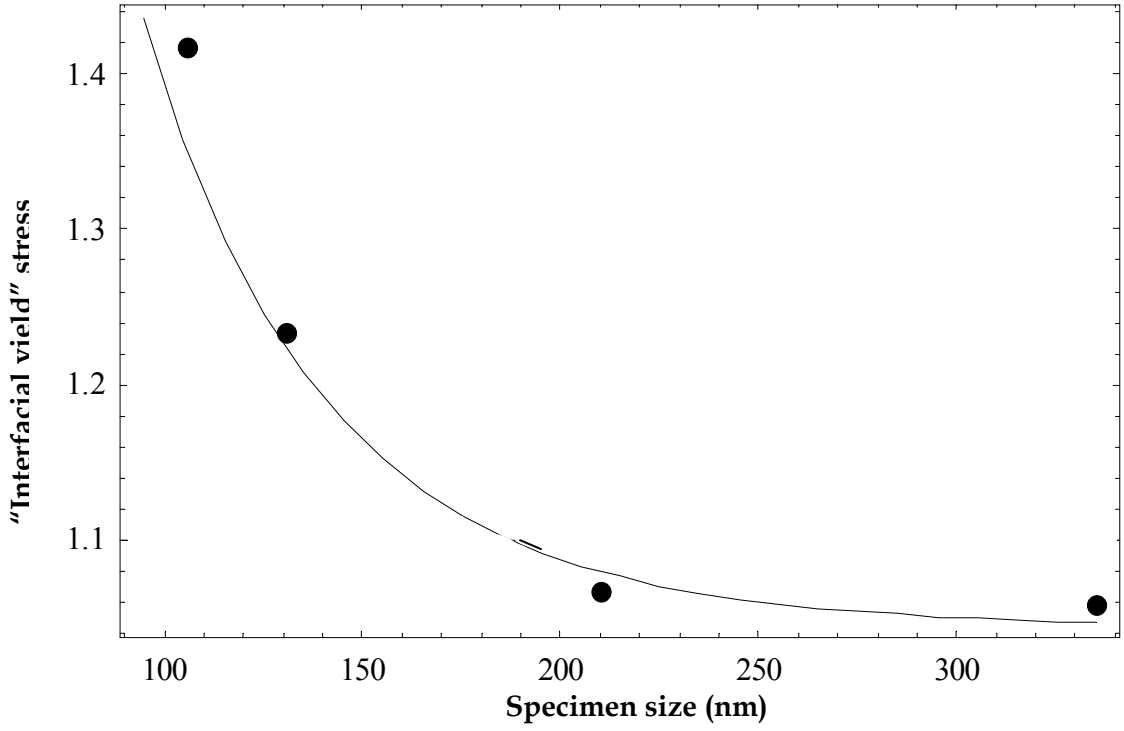

Fig.8.6: Compilation of all experimental data for the dependence of "interfacial yield" to specimen size. Solid line : fit according to (8.17). Points refer to experimental data

In particular, fitting (8.17) into the experimental data provides approximate values for the internal length, $\ell = 103\text{nm}$, and for the interfacial energy-like term, $\gamma = 215\text{N/m}$ of Fe-14%Si. Since these values for ℓ and γ are the first estimates to be obtained for these parameters it is desired to check their validity through dislocation mechanics considerations. A length scale of 100 nm is reasonable, since this is on the order of the spacing between dislocation sources in the material; furthermore, in the dislocation pileup model (discussed above) 80% of the dislocations are positioned over this length scale near the boundary, as shown in Fig. 8.7.

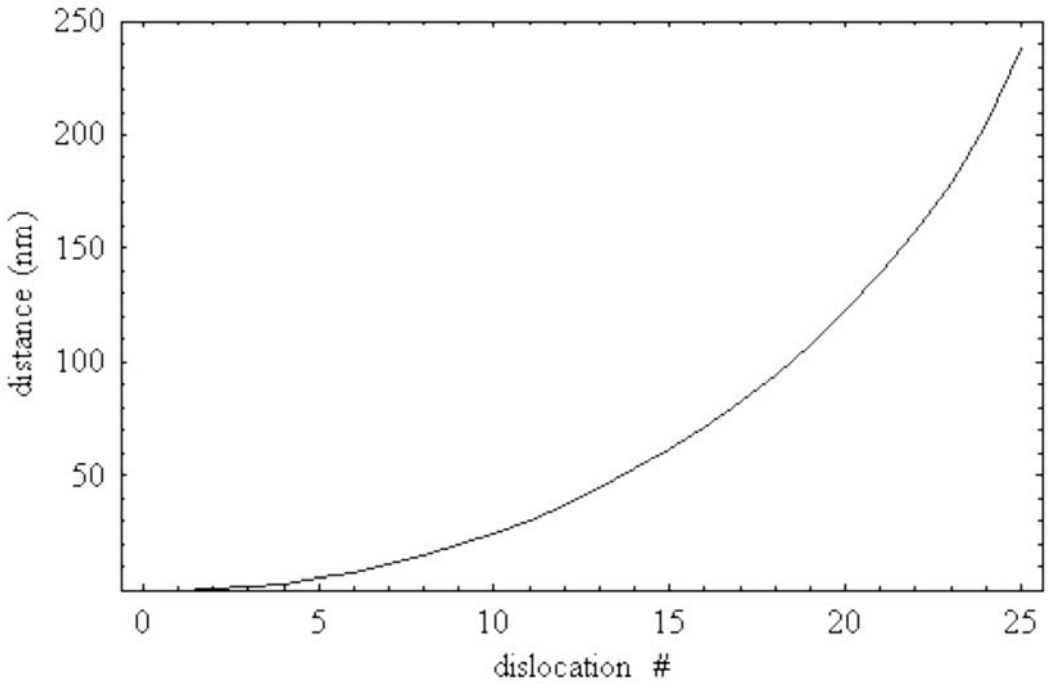

Fig.8.7. Distribution of 25 dislocations under an applied shear stress of 600 MPa in front of an interface.

To check the value of γ one may connect the "interfacial yielding", as put forward in the mathematical treatment, to the dislocation- based description by writing:

$$\tau \propto \frac{\gamma}{\ell} = \alpha\mu b\sqrt{\rho_G}\ . \tag{8.18}$$

where μ and $\sqrt{\rho_G}$ represent the shear modulus around the interface area and the geometrically stored dislocations, respectively; α is a constant depending on the dislocation interactions ranging between 0.1-1 [2]. Assuming that the internal length ℓ is a multiplier of the distances between the geometrically stored dislocations, i.e. $\ell = n\lambda_G$, (8.18) provides

$$\gamma \approx \alpha\mu bn \,. \tag{8.19}$$

Assuming that $\alpha = 0.5$, and considering 20 dislocations (i.e. n=20) to be spread over a distance of 120 nm in front of the interface, as the present case suggests, allows γ to be evaluated as 200 N/m, which is consistent with the predicted value from the fit. In this connection, it could be said that γ can be viewed as an effective modulus of the interface depending on the number of geometrically stored dislocations n, which are distributed over a certain length scale, ℓ, in front of the interface. Furthermore, the combination of applied shear stress and obstacle strength of the boundary affects the value of n and therefore γ.

It can, therefore, be concluded that the newly proposed gradient plasticity formulation, which accounts explicitly for the presence of internal boundaries, is experimentally confirmed to a certain extent as indicated by nano-indentation measurements. These measurements do not only establish the existence of an "interfacial yield" stress as the theory suggests, but also provide a qualitative verification and corresponding estimates for the key material parameters used in the mathematical formulation.

APPENDICES

APPENDIX 1

(i) Details on Frank's Rule

For a general low-angle grain boundary Frank's rule can be employed to determine the relevant dislocation configuration. If the misorientation axis $\vec{u}$, the misorientation angle θ and the grain boundary plane normal $\vec{n}$ are known, the orientation and spacing of the dislocations in the boundary plane can be predicted. In general, more than one possible configuration is found, and the correct one can be predicted by considering the elastic energy of each configuration. An arbitrary vector $\vec{V}$ is chosen in the grain boundary plane and a vector $\vec{V}$ is constructed by performing the relative rotation $\vec{r} = \theta\vec{u}$ of the two grains (Fig. a).

In general, $\vec{V}'$ does not lie in the boundary plane. Next, a circuit is constructed from the end point of $\vec{V}'$ through one grain, passing the grain boundary at the common origin of $\vec{V}$ and $\vec{V}'$ and through the other grain to the end point of $\vec{V}$. The closure vector of this circuit is $\vec{S} = \vec{V}' - \vec{V}$. $\vec{S}$ is equal to the sum of the Burgers vectors of the dislocations enclosed by the circuit:

$$\vec{S} = \sum_i n_i \vec{b}_i . \qquad \text{(a.1)}$$

The dislocations enclosed by the circuit are all cut by the vector $\vec{V}$. For small θ the closure failure $\vec{S}$ is given by the vector product :

$$\vec{S} = \vec{r} \times \vec{V} \,. \qquad \text{(a.2)}$$

By choosing several different vectors $\vec{V}$ and calculating the corresponding vectors $\vec{S}$, the dislocation structure can be obtained. For example in a symmetrical tilt boundary, $\vec{S} = 0$ if $\vec{V}$ is chosen parallel to the rotation axis, which means that all misfit dislocations are parallel to $\vec{u}$. Their spacing can be obtained by choosing a second vector $\vec{V}$, which is not parallel to $\vec{u}$. It is noted that the elastic interaction between dislocations that belong to a network and an individual dislocation in the lattice is not the same as the elastic interaction between two individual dislocations. In good approximation, this elastic interaction is negligible at distances greater than the spacing of the dislocations in the network.

(ii) Details on the Structural Unit Model

An example is the application of the structural unit model from computer simulations found in the $\Sigma 57$ [110] symmetric tilt boundary with $(\vec{2}27)$ boundary plane and rotation angle $\theta = 44^0$ (Fig.a).

The structure of this boundary can be described very well as a contiguous sequence of units from two other symmetric tilt boundaries with the same rotation axis, the $\Sigma 11(\vec{1}13)(\theta = 50.48^0)$ and the $\Sigma 27(\vec{1}15)(\theta = 31.59^0)$. The units from the favored boundary that is closest in misorientation to the $\Sigma 57$ boundary are called *majority units* and the structure of the low coincidence boundary is described as a misorientation with respect to the boundary consisting entirely of the majority units.

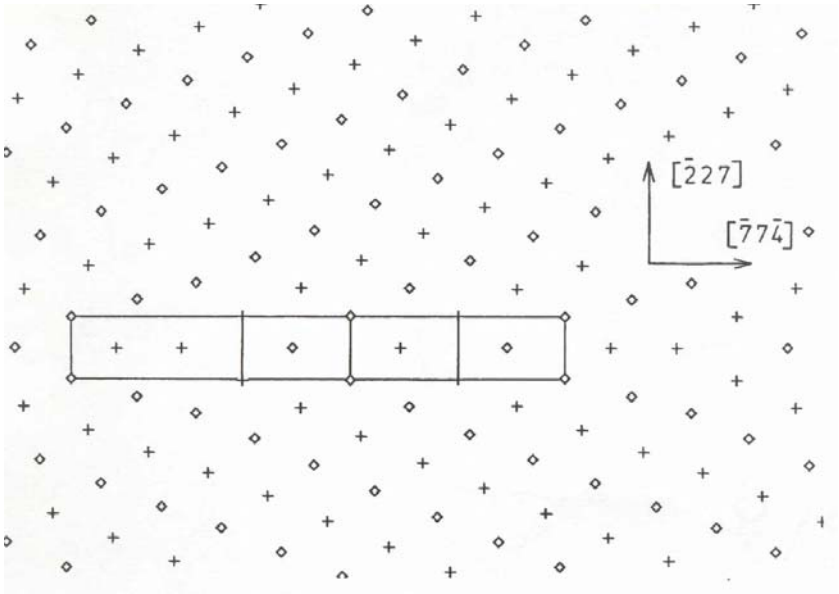

Fig. a: $\Sigma 57(\theta = 44^0)$ *grain boundary. This boundary contains structural units of the* $\Sigma 11$ *and the* $\Sigma 27$ *boundaries*

The minority units contain the core of the DSC dislocations describing the orientation difference. In this example, the units of the $\Sigma 27$ boundary are the locations of the $1/11[\bar{2}26]$ DSC dislocations of the $\Sigma 11$ boundary. We can reproduce the misorientation difference of 6.5° between the $\Sigma 57$ and the $\Sigma 11$ boundary with b=0.603 a_0 , i.e. the length of the Burgers vector of $1/11[\bar{2}26]$ DSC dislocationms) and d=5.34 a_0 , i.e. the distance between the $\Sigma 27$ units. Using Eq. (2.1) we obtain $\theta \approx b/d = 6.5^0$.

Another important concept regarding the structure of grain boundaries is the structural multiplicity of grain boundaries [50,51], i.e. the occurrence of several metastable structures for the same boundary. In the framework of the structural unit model, a necessary condition for the description of non-favored boundaries as a continuous sequence of structural units of favored boundaries, is that the units are compatible in the sense that they may appear in the same boundary without severe distortion. It has been shown [48] that when the units of the favored boundaries are not compatible, two independent series of

boundary structures exist which are composed of units of a favored boundary and compatible units of some other boundary. Each series emanates from a favored boundary and a discontinuous change of boundary structure exists at the misorientation where the two series have the same energy. In the vicinity of this misorientation at least two metastable structures exist [52,53].

However, a much larger multiplicity of structures exists when a favored boundary has several metastable structures which are very similar in energy. The boundaries that contain units of such a favored boundary may consist of different combinations of the several possible units. The structures with different combinations may have very similar energies, thus giving rise to very extensive multiplicity. If the condition of periodicity is relaxed, an infinite number of combinations is possible. It can be expected that in ordered compounds structural multiplicity will be more extensive than in monoatomic materials.

APPENDIX 2

A. BOUNDS FOR THE SINGLE-PHASE LINEAR MEDIUM

This appendix develops bounds for β^{eff}, for a single medium with potential (4.3), which contains interfaces distributed randomly. The potential associated with each interface is given by (4.43). The subscript *c* (for "comparison") adds nothing to the reasoning and so is omitted throughout this appendix. The starting point is the variational definition (3.41).

Two-point lower bound.

First, a lower bound for the potential is obtained by introducing the dual interface potential

$$\phi^*(t) = \sup_{\varepsilon^p}\{t\varepsilon^p - \phi(\varepsilon^p)\}\,. \tag{A.1}$$

When the interfacial energy assumes a quadratic form as in (3.4), its dual (A.1) takes the form

$$\phi^*(t) = \frac{t^2}{2\alpha}\ . \tag{A.2}$$

Use now of the definition of (A.1) provides the Fenchel inequality

$$\phi(\varepsilon^p) \geq t\varepsilon^p - \phi^*(t)\,, \tag{A.3}$$

for all ε^p and *t*. Hence, the effective response of the material (2.41) can be written as

$$V^{eff}(\bar{\varepsilon}_{ij}^P) \geq \inf_{\varepsilon^P} \frac{1}{2R}\left\{\int_{-R}^{R} \frac{1}{2}\beta[(\varepsilon^p)^2 + \ell^2(\varepsilon_{,x}^p)^2]dx + \sum_{x\in\Gamma_D}[t\varepsilon^p - \phi^*(t)]\right\}, \tag{A.4}$$

for any *t*; the infimum is attained when the following equations are satisfied

$$\beta[\varepsilon^p - \ell^2\varepsilon_{,xx}^p] = \bar{\sigma}, x \notin \Gamma_D\,, \tag{A.5}$$

$$\beta\ell^2[\varepsilon_{,x}^p] = t(x)\,, \text{ across any interface,} \tag{A.6}$$

$$\varepsilon^p_{,x}\Big|_{\pm R} = 0\,. \tag{A.7}$$

This purely linear problem is now solved by considering the Green's function $G(x,x')$ that satisfies the following differential equation and boundary condition:

$$G(x,x') - \ell^2 G_{,xx}(x,x') = \delta(x-x')\,,\ -R<x<R\,, \tag{A.8a}$$

$$G_{,x}(\pm R, x') = 0\,. \tag{A.8b}$$

It follows directly from (A.8) that $\int_{-R}^{R} G(x,x')dx = 1$, and standard reasoning gives $G(x,x') = G(x',x)$. Solving therefore the system of equations (A.5-7) through use of the Green's function gives the plastic strain expression as

$$\varepsilon^p(x) = \frac{1}{\beta}\left\{\bar{\sigma} - \sum_{x'\notin\Gamma_D} G(x,x')t(x')\right\}. \tag{A.9}$$

It can be seen that the specified mean value of ε^p is obtained by setting the Langrage multiplier $\bar{\sigma}$, which is equivalent to the mean stress, equal to $\bar{\sigma} = \beta\bar{\varepsilon}^p + n_\Gamma \bar{t}$, where n_Γ is the mean density of interfaces in the interval under consideration (-*R*, *R*), and $\bar{t}$ the mean value of *t* over these interfaces. Hence (A.9) can be re-written as

$$\varepsilon^p(x) = \bar{\varepsilon}^p - \frac{1}{\beta}\left\{\sum_{x'\notin\Gamma_D} G(x,x')t(x') - n_\Gamma \bar{t}\right\}. \tag{A.10}$$

Now the system if equations (A.5-7) is expressed as

$$\beta[\varepsilon^p - \ell^2\varepsilon^p_{,xx}] = \bar{\sigma} - \sum_{x\notin\Gamma_D} t(x')\delta(x-x'), -R<x<R; \varepsilon^p_{,x}(\pm R) = 0\,. \tag{A.11}$$

As a result the integral in (A.4) is reduced to

$$\int_{-R}^{R}\frac{1}{2}\beta[(\varepsilon^p)^2 + \ell^2(\varepsilon^p_{,x})^2]dx = \frac{1}{2}\left[\beta(\varepsilon^p)^2 - \frac{n_\Gamma^2\bar{t}^2}{\beta} + \frac{1}{2R}\sum_{x'\in\Gamma_D}\sum_{x''\in\Gamma_D} G(x',x'')\frac{t(x')t(x'')}{\beta}\right]. \tag{A.12}$$

Substituting therefore (A.12) in (A.4) gives

$$V^{eff}(\bar{\varepsilon}^p) \geq \frac{1}{2}\left[\beta(\bar{\varepsilon}^p)^2 + \frac{n_\Gamma^2\bar{t}^2}{\beta} - \frac{1}{2R}\sum_{x'\in\Gamma_D}\sum_{x''\in\Gamma_D} G(x',x'')\frac{t(x')t(x'')}{\beta}\right] + n_\Gamma\bar{t}\,\bar{\varepsilon}^p - \frac{1}{2R}\sum_{x''\in\Gamma_D}\phi^*(t(x))\,. \tag{A.13}$$

If this inequality is optimized over $t(x)$ the exact V^{eff} is produced. Taking however $t \equiv \text{constant} = \bar{t}$ gives the lower bound expression

$$V^{eff}(\bar{\varepsilon}^p) \geq \frac{1}{2}\beta(\bar{\varepsilon}^p)^2 + n_\Gamma \bar{t}\,\bar{\varepsilon}^p - \frac{S_2 \bar{t}^{\,2}}{\beta} - n_\Gamma \phi^*(\bar{t}) \,, \tag{A.14}$$

$$S_2 = \frac{1}{2R}\sum_{x' \in \Gamma_D}\sum_{x'' \in \Gamma_D} G(x', x'') - n_\Gamma^2 \,. \tag{A.15}$$

Allowing ϕ to take its quadratic form: $\phi(\varepsilon^p) = \frac{1}{2}\alpha(\varepsilon^p)^2$ and optimizing (A.14) with respect to $\bar{t}$ gives

$$V^{eff}(\bar{\varepsilon}^p) \geq \frac{1}{2}\left\{\beta + \frac{n_\Gamma}{S_2/(n_\Gamma \beta) + 1/\alpha}\right\}(\bar{\varepsilon}^p)^2 \,, \tag{A.16}$$

from which it follows that the lower bound for β^{eff} is

$$\beta^{eff} \geq \beta\left\{1 + \frac{n_\Gamma}{S_2/n_\Gamma + \beta/\alpha}\right\}. \tag{A.17}$$

If R is large in comparison with the correlation length for the interfaces, S_2 can be evaluated by replacing the special average with an ensemble average; $G(x', x'')$ in this case takes its infinite body form

$$G(x - x') = \frac{e^{-|x-x'|/\ell}}{2\ell} \,, \tag{A.18}$$

and

$$S_2 = \frac{1}{2\ell}\int e^{-|x'|/\ell}[n_{\Gamma\Gamma}(x') - n_\Gamma^2]dx' \,, \tag{A.19}$$

where $n_{\Gamma\Gamma}(x - x')$ is the probability of finding interfaces at x and x'. When the interfaces are distributed according to a Poisson process of intensity n_Γ the two point density $n_{\Gamma\Gamma}$ is

$$n_{\Gamma\Gamma}(x - x') = n_\Gamma \delta(x - x') + n_\Gamma^2 \,. \tag{A.20}$$

For this particular medium therefore $S_2 = n_\Gamma/(2\ell)$ and formula (3.39) results by setting $n_\Gamma = \lambda = 1/(2L)$.

Three point upper bound

An upper bound now is developed by substituting the trial field (A.10) into (2.41). The new work that is required is the evaluation of

$$\frac{1}{2R}\sum_{x\in\Gamma_D}\frac{1}{2}\alpha(\varepsilon^p(x))^2, \tag{A.21}$$

in which it follows that ε^p is given by (A.10). In particular

$$\frac{1}{2R}\sum_{x\in\Gamma_D}(\varepsilon^p(x))^2 = n_\Gamma\left(\bar{\varepsilon}^p+\frac{n_\Gamma\bar{t}}{\beta}\right)^2 - 2\left(\bar{\varepsilon}^p+\frac{n_\Gamma\bar{t}}{\beta}\right)^2\frac{1}{2R}\sum_{x\in\Gamma_D}\sum_{x'\in\Gamma_D}G(x,x')\frac{t(x')}{\beta}$$
$$+\frac{1}{2R}\sum_{x\in\Gamma_D}\sum_{x'\in\Gamma_D}\sum_{x''\in\Gamma_D}G(x,x')G(x,x'')\frac{t(x')t(x'')}{\beta^2}. \tag{A.22}$$

Optimizing with respect to arbitrary $t(x)$ would give V^{eff} exactly, as in the previous case, therefore the approximation $t \equiv \text{constant} = \bar{t}$ is adopted again. This gives

$$V^{eff}(\bar{\varepsilon}^p) \le \frac{1}{2}\left\{\beta(\bar{\varepsilon}^p)^2 + n_\Gamma\alpha(\bar{\varepsilon}^p)^2 - 2n_\Gamma\alpha\frac{\bar{t}}{\beta}S_2 + \frac{\bar{t}^2}{\beta}S_2 - 2n_\Gamma\alpha\frac{\bar{t}^2}{\beta^2}S_2 + n_\Gamma\alpha\frac{\bar{t}^2}{\beta^2}S_3\right\} \tag{A.23}$$

where the definition (A.15) still holds and S_3 is defined through

$$n_\Gamma S_3 = \frac{1}{2R}\sum_{x\in\Gamma_D}\sum_{x'\in\Gamma_D}\sum_{x''\in\Gamma_D}G(x,x')G(x,x'') - n_\Gamma^3. \tag{A.24}$$

Now the bound (A.23) is optimized with respect to $\bar{t}$ to give

$$V^{eff}(\bar{\varepsilon}^p) \le \frac{1}{2}\beta(\bar{\varepsilon}^p)^2\frac{\left\{1+\frac{n_\Gamma\alpha}{\beta}\left(\frac{S_3}{S_2}-1\right)+\left(\frac{n_\Gamma\alpha}{\beta}\right)^2\left(\frac{S_3}{S_2}-\frac{S_2}{n_\Gamma^2}-2\right)\right\}}{1-\frac{n_\Gamma\alpha}{\beta}+\frac{n_\Gamma\alpha}{\beta}\left(\frac{S_3}{S_2}-1\right)}. \tag{A.25}$$

For large R, the restriction for S_3 can be simplified (as was for S_2) by replacing spatial averages with ensemble averages, and Green's function taking its infinite-

body form (A.18). For this particular Poisson interface distribution, it is advantageous to split $n_\Gamma S_3$ into contributions involving one, two, and three distinct points as

$$n_\Gamma S_3 = \frac{1}{2R}\left\{\sum_x (G(x,x))^2 + \sum_x \sum_{x' \neq x} [2G(x,x)G(x,x') + (G(x,x))^2] + \sum_x \sum_{x' \neq x} \sum_{x'' \neq x,x'} G(x,x')G(x,x'')\right\} - n_\Gamma^3. \quad \text{(A.26)}$$

Since the interfaces are distributed according to a Poisson process the spatial average is replaced by the ensemble average to give

$$n_\Gamma S_3 = \frac{n_\Gamma}{4\ell^2} + \frac{n_\Gamma^2}{4\ell^2}\left[2\int_0^\infty e^{-x/\ell}dx + \int_0^\infty e^{-2x/\ell}dx\right] + \frac{n_\Gamma^3}{4\ell^2}\left(\int_0^\infty e^{-x/\ell}dx\right)^2 - n_\Gamma^3 = \frac{n_\Gamma}{4\ell^2} + \frac{n_\Gamma^2}{4\ell^2}. \quad \text{(A.27)}$$

Substituting therefore (A.27) and (A.19) in (A.25), along with the fact that $n_\Gamma = \lambda = 1/(2L)$ produces the upper bound given in (4.44).

B. LOWER BOUND AND APPROXIMATIONS FOR THE TWO-PHASE LINEAR MEDIUM

This appendix develops a lower bound for β^{eff} for a two-phase random linear medium. Since it was shown in Chapter 5 that the bounds obtained through use of two and three point statistics had similar trends, only the two-point statistics will be considered here for simplicity. It is analogous to the lower bound for the single-phase medium given in Appendix A, in that it makes use of the statistics of points taken two at a time. The formalism also delivers variational approximations. The potential V for the medium (again the subscript c is dropped) is given by (4.3); in particular

$$\beta(x) = \beta_1 \chi_1(x) + \beta_2 \chi_2(x), \tag{B.1}$$

where χ_1 takes the value 1 in material 1, and 0 in material 2; it follows that $\chi_2(x) = 1 - \chi_1(x)$. The interfaces are characterized by the quadratic potential (4.4). Now to proceed further, a linear comparison medium with uniform properties is introduced; its potential is given by $V_0(\varepsilon^P, \varepsilon^P_{,x}) = \frac{1}{2}\beta_0[(\varepsilon^P)^2 + \ell^2(\varepsilon^P_{,x})^2]$. Since the properties are uniform everywhere, β_0 =constant and a lower bound is obtained by taking $\beta_0 < \min \beta_1, \beta_2$ and defining

$$(V - V_0)^*(s, \hat{s}, x) = \sup_{\varepsilon^p, \gamma}\{s\varepsilon^p + \hat{s}\gamma - (V - V_0)(\varepsilon^p, \gamma)\} = \frac{s^2 + \hat{s}^2/\ell^2}{2(\beta(x) - \beta_0)}. \tag{B.2}$$

Thus,

$$V(\varepsilon^p, \varepsilon^p_{,x}, x) = \frac{1}{2}\beta_0(\varepsilon^p)^2 + s\varepsilon^p + \hat{s}\varepsilon^p_{,x} - (V - V_0)^*(s, \hat{s}, x). \tag{B.3}$$

Combination of (B.3) with (A.3), and (2.41) gives the lower bound relation

$$V^{eff}(\bar{\varepsilon}^p) \geq \inf_{\varepsilon^p} \frac{1}{2R}\left\{\int_{-R}^{R} ((\beta_0/2)[(\varepsilon^p)^2 + \ell^2(\varepsilon^p_{,x})^2] + s\varepsilon^p + \hat{s}\varepsilon^p - (V - V_0)^*(s, \hat{s}, x))dx + \sum_{x \in \Gamma_D}(t\varepsilon^p - \phi^*(t))\right\} \tag{B.4}$$

The infimum with respect to ε^p is attained when

$$\varepsilon^p(x) = \overline{\varepsilon}^p \frac{1}{\beta_0}\left\{\int_{-R}^{R}[G(x,x')(s(x')-\overline{s})+G_{,x'}(x,x')\hat{s}(x')]dx' + \sum_{x'\in\Gamma_D} G(x,x')t(x') - n_\Gamma \overline{t}\right\}. \quad \text{(B.5)}$$

where G is the Green's function that was introduced in Appendix A. Substituting (B.5) into (B.4) produces an expression analogous to (A.13) but more involved, due to the presence of $s(x)$ and $\hat{s}(x)$. An intermediate formula, obtained by integrating by parts and exploiting the differential equation and boundary conditions satisfied by ε^p, is

$$V^{eff}(\overline{\varepsilon}^p) \geq \frac{1}{2}\beta_0(\overline{\varepsilon}^p)^2 + \frac{1}{4R}\int_{-R}^{R}[(\varepsilon^p)^2(s-\overline{s}) + \varepsilon^p_{,x}\hat{s}]dx + \left(\frac{1}{4R}\sum_{x\in\Gamma_D}\varepsilon^p(x)t(x) - \frac{1}{2}\overline{\varepsilon}^p n_\Gamma \overline{t}\right)$$
$$+ \overline{\varepsilon}^p(\overline{s} + n_\Gamma \overline{t}) - \frac{1}{4R}\int_{-R}^{R}\frac{s^2 + \hat{s}^2/\ell^2}{\beta-\beta_0}dx - \frac{n_\Gamma \overline{t}^2}{2\alpha}. \quad \text{(B.6)}$$

Combining (B.5) with (B.6) gives $V^{eff}(\overline{\varepsilon}^p)$ as a quadratic function of $s(x)$, $\hat{s}(x)$ and $t(x)$. As for the homogeneous random media, optimization with respect to these variables will provide the exact $V^{eff}(\overline{\varepsilon}^p)$; therefore, to obtain a bound we set $t \equiv \text{constant} = \overline{t}$, $\hat{s}(x) = 0$ and

$$s(x) = s_1\chi_1(x) + s_2\chi_2(x). \quad \text{(B.7)}$$

Hence the general form for V^{eff} now reads

$$V^{eff}(\overline{\varepsilon}^p) \geq \frac{1}{2}\beta_0(\overline{\varepsilon}^p)^2 + \overline{\varepsilon}^p(\overline{s} + n_\Gamma\overline{t}) - \frac{1}{2}\left\{\sum_{i=1}^{2}\sum_{j=1}^{2}A_{ij}s_is_j + 2\sum_{i=1}^{2}B_is_i\overline{t} + C\overline{t}^2\right\}$$
$$- \frac{1}{2}\left\{\sum_{i=1}^{2}\frac{p_is_i^2}{\beta_i-\beta_0} + \frac{n_\Gamma\overline{t}^2}{\alpha}\right\} \quad \text{(B.8)}$$

where the volume fraction of material i is given by

$$p_i = \frac{1}{2R}\int_{-R}^{R}\chi_i(x)dx\ , \quad \text{(B.9)}$$

and the constants A_{ij}, B_i and C are defined as

$$A_{ij} = \frac{1}{2R}\int_{-R}^{R}dx\int_{-R}^{R}\big(\chi_i(x)-p_i\big)G(x,x')\big(\chi_j(x')-p_j\big)dx', \quad \text{(B.10)}$$

$$B_i = \frac{1}{2R}\int_{-R}^{R} dx \int_{-R}^{R} \left(\chi_i(x) - p_i\right) G(x,x') \left\{ \sum_{x'' \in \Gamma_D} \delta(x' - x'') - n_\Gamma \right\} dx', \qquad \text{(B.11)}$$

$$C = \frac{1}{2R}\int_{-R}^{R} dx \int_{-R}^{R} \left\{ \sum_{y \in \Gamma_D} \delta(x - y) - n_\Gamma \right\} G(x,x') \left\{ \sum_{y' \in \Gamma_D} \delta(x' - y') - n_\Gamma \right\} dx'. \qquad \text{(B.12)}$$

The previously stated relation $\chi_2(x) = 1 - \chi_1(x)$ implies that

$$A_{11} = A_{22} = -A_{12} = -A_{21},\ B_1 + B_2 = 0,\ p_1 + p_2 = 1. \qquad \text{(B.13)}$$

Substituting (B.13) in (B.8) gives the simpler upper bound form

$$V^{eff}(\bar{\varepsilon}^p) \geq \frac{1}{2}[\beta_0(\bar{\varepsilon}^p)^2 + (\bar{s} + n_\Gamma \bar{t})(\bar{\varepsilon}^p)], \qquad \text{(B.14)}$$

in which the values of s_i and $\bar{t}$ that maximize (B.14) are found by solving the equations

$$\frac{p_1 s_1}{\beta_1 - \beta_0} + A_{11}(s_1 - s_2) + B_1 \bar{t} = p_1 \bar{\varepsilon}^p,$$

$$\frac{p_2 s_2}{\beta_2 - \beta_0} + A_{11}(s_1 - s_2) + B_1 \bar{t} = p_2 \bar{\varepsilon}^p,$$

$$\frac{n_\Gamma \bar{t}}{\alpha} + B_1(s_1 - s_2) = n_\Gamma \bar{\varepsilon}^p. \qquad \text{(B.15)}$$

The problem that remains is the evaluation of A_{11}, B_1 and C. If the medium is a stationary random medium and R is large compared to a correlation length, these constants can be expressed as ensemble averages:

$$A_{11} = \int G(x)\left(p_{11} - p_1^2\right) dx,$$

$$B_1 = \int G(x)\left(q_{1\Gamma}(x) - p_1 n_\Gamma\right) dx,$$

$$C = \int G(x)\left(n_{\Gamma\Gamma}(x) - n_\Gamma^2\right) dx, \qquad \text{(B.16)}$$

where $G(x)$ is defined in (A.18) and

$$p_{11}(x-x') = \left\langle \chi_1(x)\chi_1(x') \right\rangle,$$

$$q_{1\Gamma}(x-x') = \left\langle \chi_1(x) \sum_{y'\in\Gamma_D} \delta(x'-y') \right\rangle,$$

$$n_{\Gamma\Gamma}(x-x') = \left\langle \sum_{y\in\Gamma_D} \sum_{y'\in\Gamma_D} \delta(x-y)\delta(x'-y') \right\rangle. \qquad \text{(B.17)}$$

These quantities given in (B.17), are evaluated for a for a particular random medium, in Appendix C: see equations (C.5), (C.6) and (C.7). In order for the computations in Chapter 4 to give the best lower bound the limiting case $\beta_0 = \min \beta_1, \beta_2$ was employed. Relaxation of the restriction $\beta_0 \le \min \beta_1, \beta_2$ generates a stationary approximation but not an upper bound if α>0, in view of the inequality (A.3). The choice $\beta_0 = \max \beta_1, \beta_2$ would generate an upper bound in the absence of the interface potential, α=0 , but in its presence gives what might be termed an "upper approximation".

C. A PARTICULAR TWO-PHASE RANDOM MEDIUM

The purpose of this appendix is to obtain explicit formulae for the two-point functions (B.17). The model chosen here is a simple example of the "Miller cell material". Therefore points are placed along the x-axis according to a Poisson process of intensity λ. Let the points be $\{x_n\}, -x < n < x$, where $x_n < x_{n+1}$ for each n. The basic intervals $\{(x_n, x_{n+1})\}$ into which the line is divided are called "cells" and different properties are assigned to each phase, i.e. the cells with probability p_1 are taken to have properties denoted by 1, and similarly the cells with probability p_2 are characterized with properties denoted with 2. If the same properties (and hence same orientation) are assigned to adjacent cells, their common boundary point is not an interface point and so has no interfacial potential; if adjacent cells have different properties, their boundary point is an interface. The intervals whose end points are interfaces will be called "material intervals". The elementary probability theory that is required can be obtained from any introductory text on stochastic processes, such as that of Karlin and Taylor [3] . It is necessary to know the distribution of lengths of basic intervals (cells). For this purpose, start at x_0 and let $x_1 = x_0+z_1$; $x_n = x_{n-1}+z_n$. Let $P_1(z)$ be the probability that $z_1>z$. Then $P_1(z+\delta z)$ is the probability that $z_1>z$ and there is no Poisson point in the interval $(x_0 + z,\ x_0 + z + \delta z)$. Thus, since points are independently distributed,

$$P_1(z+\delta z) = P_1(z)(1-\lambda\delta z) + o(\delta z)\,. \qquad \text{(C.1}a\text{)}$$

It follows that in the limit $\delta z \to 0$

$$P_1'(z) = -\lambda P_1(z),\ \ P_1(z) = e^{-\lambda z}\,. \qquad \text{(C.1}b\text{)}$$

The corresponding function for the first point $x_1 = x_0+z$ is thus $f_1(z) = (d/dz)(1-e^{-\lambda z}) = \lambda e^{-\lambda z}$.

Now the probability density function $f_k(z) = (d/dz)P_k(z)$ is considered; $P_k(z)$ denotes the probability that $x_k - x_0 < z$. This can be found by noting that f_1 has moment generating function

$$\mathrm{E}(e^{-\theta x}) = \int_0^\infty \lambda e^{-\lambda x} e^{-\theta x} dx = \frac{\lambda}{\lambda + \theta}.$$

Moreover, since the successive interval lengths are independent

$$\int_0^\infty e^{-\theta x} f_k(x) dx = \mathrm{E}(e^{-\theta(z_1 + z_2 + \ldots + z_k)}) = \left(\frac{\lambda}{\lambda + \theta}\right)^k,$$

it follows that inverting the La Place transform provides

$$f_k(z) = \lambda \frac{(\lambda z)^{k-1}}{(k-1)!} e^{-\lambda z}. \tag{C.2}$$

Now the density function for the length of a material interval is considered. First suppose that x_0 has material 2 to its left and material 1 to its right. Then (x_0, x_k) is a material interval if (x_0, x_1) (x_1, x_2)…(x_{k-1}, x_k) are all assigned to material 1 and (x_k, x_{k+1}) is assigned to material 2. The probability density for an interval of material 1, of length z, is

$$\sum_{k=1}^{\infty} p_1^{k-1} p_2 f_k(z) = \sum_{k=1}^{\infty} p_2 \lambda \frac{(\lambda p_1 z)^{k-1}}{(k-1)!} e^{-\lambda z} = \lambda p_2 e^{\lambda p_1 z} e^{-\lambda z} = \lambda p_2 e^{-\lambda p_2 z}. \tag{C.3}$$

Therefore, the expected length of a material interval of material 1 is

$$\int_0^\infty z \lambda p_2 e^{-\lambda p_2 z} dz = \frac{1}{\lambda p_2} = 2L_1.$$

Similarly, the expected length of a material interval of material 2 is

$$\frac{1}{\lambda p_1} = 2L_2.$$

It is thus concluded that

$$p_1 = \frac{L_1}{L_1 + L_2},\ p_2 = \frac{L_2}{L_1 + L_2} \text{ and } \lambda = \frac{L_1 + L_2}{L_1 L_2}. \tag{C.4}$$

Now to calculate the required two-point functions:

First, $p_{11}(x - x')$ is the probability that x is in material 1 and x' is in material 1. If x and x_0 are in the same cell, the contribution to the probability is p_1. If they are in different cells, the contribution to the probability is p_{21}. The probability that x and x_0 are in the same cell is the probability that there is no Poisson point in (x; x'):

$e^{-\lambda|x-x'|}$. It follows that the probability that they are in different cells is 1-$e^{-\lambda|x-x'|}$. Hence

$$p_1(x-x') = p_1 e^{-\lambda|x-x'|} + p_1^2(1-e^{-\lambda|x-x'|}) = p_1^2 + p_1\, p_2 e^{-\lambda|x-x'|}. \qquad \text{(C.5)}$$

The probability that x is in material 1 and there is an interface in $(x', x'+\delta x')$ is $q_{1\Gamma}(x-x')\delta x' + o(\delta x')$. Letting $x' > x$ and allowing the first Poisson point to be in $(x', x'+\delta x')$, then this is an interface point if there is material 2 to the right. Thus, the contribution to the probability is p_2. If there is a Poisson point in (x, x'), then the point in $(x', x'+\delta x')$ is an interface point if there is material 1 on one side and material 2 on the other. The probability for this is $2p_1p_2$. Hence,

$$q_{1\Gamma}(x-x') = \lambda p_1 p_2 \{(1-2p_1)e^{-\lambda|x-x'|} + 2p_1\}. \qquad \text{(C.6)}$$

Finally, the probability that there are interface points in intervals $(x, x+\delta x)$ and $(x', x'+\delta x')$ is $n_{\Gamma\Gamma}(x-x')\delta x\delta x' + o(\delta x\delta x')$. When $x = x'$, the contribution to the density is $2\lambda p_1 p_2 \delta(x-x')$. Now assuming that x and x' are adjacent Poisson points, they are interface points if the pattern of material is either "212" or "121" .The probability for this is $p_1 p_2^2 + p_1^2 p_2 = p_1 p_2$, while the density for points being adjacent is $\lambda^2 e^{-\lambda|x-x'|}$. If the points are not adjacent, the probability that they are both interface points is $(2p_1p_2)^2$, and the density for non-adjacent Poisson points is $\lambda^2(1-e^{-\lambda|x-x'|})$. Hence, altogether,

$$n_{\Gamma\Gamma}(x-x') = 2\lambda p_1 p_2 \delta(x-x') + p_1 p_2 \lambda^2 e^{-\lambda|x-x'|} + 4p_1^2 p_2^2 \lambda^2 (1-e^{-\lambda|x-x'|}). \qquad \text{(C.7)}$$

D. OPTIMIZING V^{eff} WITH RESPECT TO α

In order to simplify the optimization with respect to *a* the expression for V^{eff} is factored so that it takes the generic form:

$$\beta^{eff} = \frac{A + B/\alpha}{C + D/\alpha}, \tag{D.1}$$

where *A*, *B*, *C* and *D* are constants that depend on the material parameters.

The generic form for V^{eff} then is

$$V^{eff}(\bar{\varepsilon}^p) = \inf_{\alpha}\left\{V_c^{eff} + \frac{E}{\alpha}\right\} = \inf_{\alpha}\left\{\frac{1}{2}\left(\frac{A + B/\alpha}{C + D/\alpha}\right)(\bar{\varepsilon}^p)^2 + \frac{E}{\alpha}\right\}, \tag{D.2}$$

where as mentioned in Chapter 5 *E* accounts for the particular interface distribution. For finite positive *a* this function has only one stationary point; to see if it is a minimum or a maximum (D.2) is expanded as $a \to \infty$:

$$\frac{A}{2C}(\bar{\varepsilon}^p)^2 + \left(E - \frac{(AD - BC)}{2C^2}(\bar{\varepsilon}^p)^2\right)\frac{1}{\alpha}. \tag{D.3}$$

It follows that this stationary point is a maximum if

$$\left(E - \frac{(AD - BC)}{2C^2}(\bar{\varepsilon}^p)^2\right) > 0, \tag{D.4}$$

from which the critical strain at which the interface yield is deduced as

$$\bar{\varepsilon}_c^p = \left(\frac{2E}{AD - BC}\right)^{1/2} C. \tag{D.5}$$

From expression (D.3) it can be deduced that prior interfacial yield

$$V^{eff} \le \frac{A}{2C}(\bar{\varepsilon}^p)^2, \text{ if } \quad \bar{\varepsilon}^p < \bar{\varepsilon}_c^p 0. \tag{D.6}$$

To find the effective response after interfacial yield (D.2) has to be minimized for when α is a stationary point. Hence differentiating (D.2), setting the resulting expression equal to zero to solve for α and then substituting this expression for back in (D.2) and performing some mathematical manipulations provides,

$$V_0^{eff}(\bar{\varepsilon}^p) = \frac{B}{2D}(\bar{\varepsilon}^p)^2 + \frac{(2E)^{1/2}(AD - BC)^{1/2}}{D}\bar{\varepsilon}^p - \frac{EC}{D}, \qquad \text{when } \bar{\varepsilon}^p \ge \varepsilon_c^p. \tag{D.7}$$

E. CONSTANTS FOR LINEAR AXIAL PROBLEM

The constants of (7.40) are given by

$$\hat{\alpha} = \frac{I_0(k_1 a)F_1}{k_2 \ell_2^2 \beta_2 I_0(k_1 a)F_2 + k_1 \ell_1^2 \beta_1 I_1(k_1 a)F_3\}},$$

$$A_1 = \frac{2\mu_1 a^2}{b^2} X_1 + \frac{2\mu_2 (b^2 - a^2)}{b^2} X_2,$$

$$B_1 = -\left(\frac{2\mu_1 j_1 K a^2}{b^2 I_0(k_1 a)} + \frac{2\mu_2 K (b^2 - a^2)}{b^2} \frac{I_1(k_2 b)J_2 + K_1(k_2 b)J_2}{I_0(k_2 a)K_1(k_2 b) + I_1(k_2 b)K_0(k_2 a)} \right)$$

where

$$F_1 = I_1(k_2 b)K_0(k_2 a) + I_0(k_2 a)K_1(k_2 b),\ F_2 = I_1(k_2 b)K_1(k_2 a) - I_1(k_2 a)K_1(k_2 b),$$
$$F_3 = I_1(k_2 b)K_0(k_2 a) - I_0(k_2 a)K_1(k_2 b);$$

$$C_1 = \frac{\beta_1}{\beta_1 + 2\mu_1} + \frac{2\mu_1 j_1}{(\beta_1 + 2\mu_1) I_0(k_1 a)},$$

$$C_2 = \frac{\beta_2}{\beta_2 + 2\mu_2} + \frac{2\mu_2}{(\beta_2 + 2\mu_2)} \frac{K_1(k_2 b)\, j_2 + I_1(k_2 b)J_2}{I_0(k_2 a)K_1(k_2 b) + I_1(k_2 b)K_0(k_2 a)};$$

$$j_1 = \frac{2}{a^2} \int_0^a r I_0(k_1 r)\, dr,\ j_2 = \frac{2}{b^2 - a^2} \int_a^b r I_0(k_2 r)\, dr,\ J_2 = \frac{2}{b^2 - a^2} \int_a^b r K_0(k_2 r)\, dr,$$

and

$$K = \frac{2\{k_1 \ell_1^2 \beta_1 \mu_1 (\beta_2 + 2\mu_2) I_1(k_1 a)F_1 + k_2 \ell_2^2 \beta_2 \mu_2 (\beta_1 + 2\mu_1) I_0(k_1 a)F_2\}}{(\beta_1 + 2\mu_1)(\beta_2 + 2\mu_2)\{k_2 \ell_2^2 \beta_2 I_0(k_1 a)F_2 + k_1 \ell_1^2 \beta_1 I_1(k_1 a)F_3\}}.$$

SUMMARY

In the present thesis a continuum gradient plasticity theory is developed which takes into account the effect of internal surfaces such as grain boundaries and interfaces. This is done by introducing an additional "interfacial" energy-like term (interfacial penalty) into the overall potential functional of the domain under consideration and assuming that the plastic strain gradients and their conjugate higher-order stresses are discontinuous across interfaces, while displacements and plastic strains remain continuous. The physical motivation behind this mathematical formulation rests on the interaction of dislocations (the carriers of plastic deformation) and internal boundaries which may oppose dislocation motion, absorb/emit dislocations, or act as stress concentrators. The constitutive assumptions for the higher-order stress and the interfacial energy term should therefore ideally be deduced from microscopic considerations, including the formation and destabilization of dislocation pileups in front of grain boundaries, the reaction mechanisms between lattice and grain boundary dislocations, as well as the effect of grain boundary ledges resulting from these reactions. In addition to such dislocation microplasticity mechanisms, appropriate experiments pertaining to the structure, energy and strength of interfaces should be equally important in the construction and evaluation of the continuum model. In particular, nano-indentation measurements can be made near a grain boundary to obtain estimates for the interfacial energy term and the corresponding "interfacial yield" stress.

In the present work, an attempt is made to address the above three issues i.e., - (i) the physics of grain boundaries and interfaces; (ii) the development of a gradient plasticity model which contains an interfacial potential and its applicability to consider the effective response of polycrystals and composites with emphasis on size effects; (iii) the estimation of the new model parameters from nano-indentation experiments - , within a unifying and interdisciplinary framework, as follows:

After the introductory *Chapter 1*, a physical description of grain boundaries and interfaces is provided in *Chapter 2*. Details on crystallography and types of most common grain boundaries are given, the grain boundary structural model and an expression for the interfacial energy resulting from it is presented, and possible mechanisms of dislocation-grain boundary interactions are discussed. The main purpose of this chapter is to illustrate the significance of introducing the interfacial energy penalty term in the continuum gradient plasticity formulation, to motivate the constitutive form of this term, and justify the assumption of discontinuous plastic strain gradients across internal boundaries.

In *Chapter 3*, the appropriate variational formulation of the aforementioned framework is given and the resulting field equations and boundary conditions are deduced. The effective response of a general nonlinear strain gradient medium with internal boundaries is then obtained through a homogenization procedure based on the introduction of average stress and strain fields for the overall macroscopic behavior (where gradient effects are smeared out) and a minimization of a properly defined effective potential functional is performed. Elementary upper (Voigt-type) and lower (Reuss-type) bounds for the effective response are obtained, as well as a more refined upper bound, which is based on the comparison with a material that has a linear response. The methodology is valid for all types of internal surfaces against which dislocation pileups can form; it can therefore be used to model structurally homogenous materials such as polycrystals (internal boundaries are grain boundaries) or chemically

heterogeneous materials such as composites (internal boundaries are interfaces between different phases, i.e. heterophase interfaces).

In *Chapter 4*, one-dimensional examples, which can be solved exactly, are considered in order to illustrate the robustness and new features of the theory, as well as its ability to describe effects not captured by previous models. First, a two-phase unit cell model is assumed with a simple quadratic gradient plastic potential and two different expressions for the interfacial energy term: a quadratic, continuously differentiable expression, and a bi-linear non-continuously differentiable one. The ordinary differential equations that result by inserting these potentials in the constitutive relations that were previously developed in Chapter 3, are solved exactly and exhibit a Hall-Petch type of dependence. In particular, the non-linear interfacial energy term provides a distinct "interfacial yield" stress. Next, a more realistic nonlinear gradient-dependent plastic potential that accounts for material yielding is considered along with a nonlinear interface term and the exact solutions obtained show again a Hall-Petch type trend. Once, however, conventional nonlinear gradient dependent plastic potentials are used, the resulting differential equations are highly nonlinear, and can be solved only numerically. This is illustrated for a homogeneous periodic medium.

For random media, in particular, an exact solution cannot be obtained even when the material response is fully linear. It is necessary, therefore, to express the nonlinear problem in terms of one for a "linear comparison medium" for which good approximate solutions can be developed. In *Chapter 5*, this method is first applied to the highly non-linear periodic material that was last examined in the previous chapter. It is shown that the "linear comparison" technique provides the same results as the exact treatment for the effective macroscopic stress-plastic strain response and corresponding size effects. Motivated by this very encouraging result, a random homogeneous polycrystal of "Poisson type" is

considered as a last example in this chapter. The linear random problem is solved approximately by use of two- and three- point statistics.

Chapter 6 is concerned with two-phase media, e.g. a composite material with distributed hard phase particles, in which interfaces are distributed periodically or randomly; for simplification purposes the formulation remains one-dimensional. The exact solutions obtained in Chapter 4 for the linear periodic medium are employed to perform the "comparison method" and obtain approximate solutions for the stress-strain curve. In the sequel consideration of two-point statistics provides an approximate solution for a linear two-phase random medium, which is then used to develop the linear comparison formulation and obtain approximate solutions for a highly nonlinear random medium. It is shown that the effective responses of the nonlinear periodic and random two-phase media are strikingly similar to each other for large specimen sizes.

In *Chapter 7*, the difficulties involved with a three-dimensional generalization of the theory are illustrated. Even for the simple case of an axially symmetric composite, i.e. a metal fiber embedded in a metal matrix, which is deformed in tension under generalized plane strain conditions, the solution involves complex Bessel functions and an analytic expression for the "interfacial yield" stress cannot be obtained, even for the simple case in which the gradient dependent plastic potential is quadratic and the interfacial penalty nonlinear.

Finally, in *Chapter 8* nano-indentation experimental results for an Fe-14%Si bi-crystal are presented in support of the model assumptions and results obtained in the previous chapters. The experiments show that as the grain boundary is approached, in addition to the occurrence of a first plateau in the load vs. depth nanoindentation graph, which indicates the grain interior yield, a second plateau (in the load vs. depth nanoindentation graph) is observed, which indicates the existence of an "interfacial yield" stress as the aforementioned formulation proposes. Comparison of the experimental results with the analytic

expression derived in Chapter 4 for the "interfacial yield" stress of a bi-crystal determines the interfacial energy and the internal length parameters of Fe-14%Si as $\ell = 103$ nm and $\gamma = 215$N/m, respectively. Assuming that the length ℓ is a multiplier of the distances between the geometrically stored dislocations, γ is predicted to be about 200 N/m for the present case and it is concluded that γ can be viewed as an effective modulus depending on the number of geometrically stored dislocations in front of the interface distributed over a certain length ℓ. It should be noted that similar size effects were observed for the grain interior yield stress, which remained constant for all indentations performed, regardless of the distance to the grain boundary. The description obtained this way is consistent with related dislocation mechanisms that were explored in Chapter 2.

In conclusion, the thesis has introduced a new theoretical framework based on gradient plasticity considerations with allowance of internal boundaries and corresponding interfacial energy (penalty) terms. The results are employed for the analysis of "size effects" related to "interfacial yield", these effects have been demonstrated experimentally, and initial estimates of the parameters introduced in the theory have been obtained.

SAMENVATTING

In dit proefschrift wordt een gradiënt plasticiteit theorie ontwikkeld waarin de bijdragen van korrelgrenzen en andere grensvlakken onder de loep worden genomen. Centraal in het proefschrift staat de introductie van een grensvlak energie term in de totale potentiaal functie en de aanname dat de plastische rek gradiënten en hun geconjugeerde hogere orde spanningen discontinue zijn over het grensvlak terwijl verplaatsing en plastische rek continue blijven. De fysische beweegredenen achter deze mathematische formulering is gebaseerd op de interactie van dislocaties (de dragers van plastische deformatie) en interne grensvlakken die de beweging van dislocaties belemmeren, dislocaties annihileren of juist creëren.

De constitutieve aannamen voor de hogere orde spanning en de grensvlakenergie term zouden daarom in het ideale geval moeten worden afgeleid op microscopische schaal, zoals de formatie en destabilisatie van dislocatie pile-ups voor korrelgrenzen, reactie mechanismen tussen rooster en korrelgrens dislocaties, als mede het effect van korrelgrens richels die uit deze reacties ontstaan. Naast deze dislocatie microplasticiteitsmechanismen zijn ook experimenten van belang betreffende structuur, energie en sterkte van het grensvlak voor het construeren en evalueren van het continuüm model. In het bijzonder kunnen nanoindentatie metingen nabij het grensvlak dienen ter bepaling van de grensvlakenergie en sterkte.

In dit proefschrift worden de bovengenoemde drie onderwerpen behandeld:

(i) de fysica van korrelgrenzen en grensvlakken

(ii) de ontwikkeling van een gradiënt plasticiteit model gebaseerd op de grensvlakpotentiaal functie en de toepasbaarheid voor wat betreft de effectieve response van polykristallen en composieten gezien hun afmetingen.

(iii) afschatting van de modelparameters door middel van nano-indentatie experimenten.

Na de introductie in Hoofdstuk 1 volgt in Hoofdstuk 2 een fysische beschrijving van korrelgrenzen. Details van de effecten van de kristallografie van korrelgrenzen op de transfer van dislocaties worden onderzocht. Het belangrijkste doel van dit hoofdstuk is om het begrip grensvlakenergie op fysische gronden nader te adstrueren.

In Hoofdstuk 3 worden de veldvergelijkingen en grensvoorwaarden afgeleid. De effectieve respons van een algemeen niet-lineair medium wordt onderzocht, dwz een medium met korrelgrenzen. Voigt-type en Reuss-type begrenzingen worden onderzocht en bepaald. De methode is toepasbaar voor allerlei type korrelgrenzen waar dislocaties zich tegen ophopen en is daarmee ook geschikt voor grensvlakken tussen twee verschillen fasen. In Hoofdstuk 4 worden 1-D voorbeelden bestudeerd die een exacte oplossing leveren . In het bijzonder blijkt dat de niet-lineaire grensvlakenergie een duidelijke vloeispanning oplevert van het grensvlak. In Hoofdstuk 5 wordt aangetoond dat een 'lineaire expansie' methode dezelfde resultaten oplevert als de exacte behandeling. Hierdoor aangespoord wordt vervolgens de response van een random homogeen polykristal onderzocht en bij benadering opgelost met behulp van 2- en 3 puntstatistiek. Hoofdstuk 6 concentreert zich op 2-fase media, bijvoorbeeld een composiet materiaal, waarbij de grensvlakken periodiek worden verdeeld. De exacte oplossing vanuit Hoofdstuk 4 wordt vervolgens gebruikt om een benadering te vinden voor de spanning-rek curve. Aangetoond wordt dat de effectieve respons van een niet-lineaire periodiek en van een random 2-fase materiaal dezelfde resultaten opleveren. In hoofdstuk 7 worden

de moeilijkheden aan de orde gesteld met betrekking tot de 3D generalisatie van de theorie. Zelfs voor het eenvoudige geval van een axiaal symmetrische composiet materiaal, bijvoorbeeld metaal-fibers, leidt dit tot complicaties. Tot slot worden in hoofdstuk 8 de resultaten van de experimenten voor Fe-14% Si bikristallen beschreven ter ondersteuning van het model en de resultaten uit de vorige hoofdstukken. De experimenten laten zien dat bij het naderen van de korrelgrens niet alleen een eerste plateau in de grafiek van de belasting vs indrukking plaatsvindt corresponderend met de interne sterkte, maar ook een tweede die wijst op het bestaan van een grensvlak sterkte zoals voorgesteld . Door de experimentele resultaten te vergelijken met de analytische uitdrukking voor de grensvlaksterkte van een bikristal uit hoofdstuk 4 kunnen we zeggen dat het model een grensvlakenergie en interne lengte parameter voor Fe-14%Si oplevert van respectievelijk $\gamma = 215\text{N/m}$ and en $\ell = 103\text{ nm}$. Aannemend dat de lengte ℓ een veelvoud is van de afstand tussen geometrisch bepaalde dislocaties wordt γ 200N/m . De fysische interpretatie van γ kan dan gezien worden als een effectieve waarde voor de modulus afhankelijk van het aantal geometrisch bepaalde dislocaties voor het grensvlak over een afstand ℓ. Soortgelijke afmetingeffecten werden waargenomen voor de sterkte in de korrels zelf welke een constante waarde gaf bij alle uitgevoerde indentaties onafhankelijk van de afstand tot de korrelgrens.Deze beschrijving is in overeenstemming met overeenkomstige dislocatie mechanismen uit Hoofdstuk 2.

Samenvattend: Dit proefschrift relateert de sterkte van het grensvlak aan de afmetingen die daarbij een rol spelen; deze effecten zijn experimenteel aangetoond en een eerste afschatting voor de modelparameters kon worden gemaakt.

ACKNOWLEDGEMENTS

I am truly indebted to my promoter Professor Jeff De Hosson for making it possible for me to realize the first academic goals and dreams I had set, since I was a child. He did everything in his power to make my stay in Groningen as productive as possible and he taught me to appreciate the beauty of experimental work and the physics behind the mathematics. The field of material physics is so rich of course that I still have a lot to learn and I am looking forward to a continuous collaboration with him, hopefully jointly with my co-promoter Professor John Willis of Cambridge University. It was John who first took me under his scientific supervision at Cambridge University where I completed my Master of Philosophy degree in the Department of Engineering under the direction of Professor Norman Fleck. My deepest gratitude goes to John who introduced me to the beautiful world of homogenization theory and has guided me step by step from the beginning of my graduate studies to the end of it. Through his elegant style, rigor and patience he taught me what mechanics is all about and made it possible for me to start and complete this thesis together with Jeff.

The person responsible for my love for science is my father. His devotion to his work, in particular to his gradient theory, which dates back to the time I was born, is what motivated me to study mechanics. The feeling of being able to write a thesis which is based on ideas he introduced, at the time I was a newborn, cannot be described. I could have never, however, been able to follow this path

and surpass the many difficulties which came along, without the extraordinary emotional support and encouragement from my mother, who never left my side.

It is here appropriate to express my thanks to the first people who believed in me and let me get a head start in my academic studies: my high school vice principal Mr. Ken Kleine, who since he was my sixth grade teacher encouraged me to follow my goals and kept reminding them to me; and my principal Mrs. Kass Simila who encouraged me to enroll to Michigan Technological University long before finishing high school. In this connection, I would like to thank the National Science Foundation of the USA for supporting me through their Graduate Research Fellowship Program and giving me the freedom to perform the research I always wanted, anywhere in the world.

In concluding, I would like to thank my spiritual guide Fr. Simeon, as well as all the monks of the Holy Trinity orthodox monastery of Thessaloniki for appreciating what a God gift science is, and supporting my devotion to it. I also feel very thankful to my brother Elias for sharing with me all anxieties in life while traveling continuously between US and Greece, to Dr. Avraam Konstantinidis and Dr. Evaggelia Karnezi for their continuous support and encouragement, to Wouter Soer who helped me in performing nano-indentation experiments, to Alexandros Nikitas and to the life long colleagues of my father who inspired me to study mechanics such as Ilya Prigogine, Daniel Walgraef, Alexei Romanov, Steve Hackney and Mike Zaiser, as well as Nikita Morozov, Jim Rice and my grandfather in science Bill Gerberich. Finally, I would like to thank the reading committee, Professors De Raedt, Rudolf and Kok, as well the promotion committee for their interest in my thesis.

KEA

"*Every gift that is perfect is from above, coming from You, the Father of lights*."
Divine Liturgy of St. John Chrysostom

REFERENCES

[1] Truesdell and Toupin, , The Classical Field Theories, Handbook der Physik, vol III/II, Springer-Verlag, Berlin (1960).

[2] Aifantis, E.C., Transactions of ASME, J. Engng. Mat. Tech. 106, 326 (1984).

[3] Fleck, N.A., Muller, G.M., Ashby, M.F., Hutchinson, J.W., Acta Metall. Mater., 42, 475 (1994).

[4] Fleck, N.A, Hutchinson, J.W., Strain Gradient Plasticity, Advances in Applied Mechanics 33, 295-361, Academic Press (1997).

[5] Fleck, N.A., Hutchinson, J.W., J. Mech. Phys. Solids, 49, 2245 (2001).

[6] Aifantis, E.C., Int. J. Plasticity 3, 211 (1987).

[7] Fleck, N.A., Willis, J.R., J. Mech. Phys. Solids, 52, 1855 (2004).

[8] Gao, H., Huang, Y., Nix, W.D., Hutchinson, J.W., J. Mech. Phys. Solids 47, (1999).

[9] Huang, Y., Gao, H., Nix, W.D., Hutchinson, J.W., J. Mech. Phys. Solids 47 (2000).

[10] Gurtin, M.E., J. Mech. Phys. Solids 48, 989 (2000).

[11] Gurtin, M.E., J. Mech. Phys. Solids 50, 5 (2002).

[12] Gudmundson, P., J. Mech. Phys. Solids 52, 1379 (2004).

[13] a. De Hosson, J.T.M., Kooi, B.J., In: Handbook of Surfaces and Interfaces in Materials, Volume-1, chapter1, ed. H.S. Nalwa, Academic Press, p.1-114 (1999).

b. De Hosson, J.T.M, G. Van Tendeloo, D. Schrijvers, in: Handbook of Microscopy (editors: S. Amelinckx, D. van Dyck, J. van Landuyt, G. van Tendeloo), volume 3, p.5-111., VCH, N.Y. (1997) .

[14] De Hosson, J.T.M., Groen, H.B., Kooi,B.J., Vitek, V.,Acta Materialia 47, 4077 (1999).

[15] Groen, H.B., Kooi, B.J., Vellinga, W.P., De Hosson, J.T.M., Phil. Mag. 79, 2083, (1999).

[16] Vellinga, W.P., De Hosson, J.T.M., Vitek, V., Acta Materialia 45,1525, (1997).

[17] Vellinga, W.P., De Hosson, J.T.M. , Acta Materialia 45, 933 (1999).

[18] a. Mogck, S., Kooi, B.J., De Hosson, J.T.M., Acta Materialia, 52,4651 (2004).

b. Mogck, S., Kooi, B.J., De Hosson, J.T.M., Finnis, M.W., Phys. Rev. B70, 245427 (2004).
[19] Cleveringa, H.H.M., Van der Giessen, E., Needleman, A., Acta Mater. 45, 3163 (1997).
[20] Shu, J.Y., Fleck, N.A., Van der Giessen, E., Needleman, A., J. Mech. Phys. Solids 49, 1361 (2001).
[21] Bittencourt E., Needleman, A., Gurtin, M.E., Van der Giessen, E., J. Mech. Phys. Solids 51, 281 (2003).
[22] De Hosson, J.T.M., Roos, A., Metselaar, E.D. , Phil. Mag. 81, 1099, (2001).
[23] Roos, A., De Hosson, J.T.M., Van der Giessen, E., Comp. Mat. Science 20, 19 (2001).
[24] Roos, A., De Hosson, J.T.M., Van der Giessen, E., Comp. Mat. Science 20, 1 (2001).
[25] a. Aifantis, E.C., Int. J. Eng. Sci., 33, 2161 (1995).
b. Aifantis, E.C., Handbook of Materials Behavior Models, pp. 291-307, Ed. Lemaitre, Academic Press (2001).
c. Aifantis, E.C., Mechanics of Materials 35, 259 (2003).
[26] a.Willis, J.R., Continuum Models of Discrete Systems, SM Study No.12, edited by J.W. Provan, pp.185-215, University of Waterloo Press (1978).
b.Willis, J.R., Advances in Applied Mechanics, Vol. 21, edited by C. S. Yih, pp.l-78, Academic Press, New York, (1981).
[27] Talbot. D.R.S., Willis, J.R., Proc. of the Royal Soc. (2004).
[28] Ponte Castaneda, P., J. Mech. Phys. Solids, 39, 45 (1991).
[29] Ponte Castaneda, P., , J. Mech. Phys. Solids 40, 1757 (1992).
[30] Smyshlyaev, V.P., Fleck, N.A., Proc. R. Soc. A451, 795, (1995).
[31] Smyshlyaev, V.P., Fleck, N.A., J. Mech. Phys. Solids, 44, 465 (1996).
[32] Hall, E. O., Proc. Phys. Soc. London, B64, 747 (1951).
[33] Petch, N.J., Iron Steel Inst., 174, 25 (1953).
[34] a. Soer, W.A., De Hosson, J.T.M., Materials Letters, 2005, in press.
b. Soer, W.A., Aifantis, K.E., De Hosson, J.T.M., Acta Materialia 2005, submitted.
c. Aifantis, K.E., Soer, W.A., De Hosson, J.T.M., Acta Materialia 2005, submitted.
[35] Courtney, Mechanical Behavior of Materials, Prentice Hall, New York (2000).
[36] Frank, F. C., Symposium on the Plastic Deformation of Crystalline Solids, (ONR Pittsburgh), p. 150 (1950).
[37] Kronberg, M.L., and Wilson, F.H., Trans. Metall. Soc. AIME, 185, 501 (1949).
[38] Balluffi, R.W., Brokman, A., and King, A.H., Acta Metall. et Mat.,

30, 1453 (1982).
[39] Sutton, A.P., Balluffi, R.W., Interfaces in crystalline materials, Oxford, Chapter 2p.70 (1995).
[40] Dhalenne, G., Dechamps, M., Revcolevschi, A., in: Grain-boundaries in semiconductors, eds. H.J. Leamy, G.E. Pike, C.H. Seager, North-Holland, Amsterdam, p.13 (1982).
[41] Bollmann, W., Crystal Defects and Crystalline Interfaces, Springer-Verlag, Berlin (1970).
[42] King, A.H.,, Acta Metall. et Mat., 30, 419 (1982).
[43] King, A.H., and Smith, D.A., Acta Crystallogr. A, 36, 335 (1980).
[44] Bishop, G.H., and Chalmers, B., Scripta Metall. et Mat., 2, 133(1968) .
[45] Bishop, G.H., and Chalmers, B., Philos. Mag., 24, 515(1971).
[46] Schober, T., and Balluffi, R.W., Philos. Mag., 20, 511(1969).
[47] Schober, T., and Balluffi, R.W., Phys. Status Solidi B, 44, 103; 44, 115 (1971).
[48] Sutton, A.P., and Vitek, V., Philos. Trans. R. Soc. London S. A, 309, 1 (1983).
[49] De Hosson, J.T.M., and Vitek, V., Philos. Mag. A, 61, 305 (1990).
[50] Wang, G.J., Sutton, A.P., and Vitek, V., Acta Metall. et Mat., 32, 1093 (1984).
[51] Vitek, V., and De Hosson, J.T.M., Mater. Res. Soc. Symp. Proc., 63,137 (1986).
[52] Kruisman, J.J., Vitek, V., and De Hosson, J.T.M., Acta Metall. et Mat., 36, 2729 (1988).
[53] Vitek, V., Chen,S.P., Voter, A.F., Kruisman, J.J., De Hosson, J.T.M., In: Grain Boundary Chemistry and Intergranular Fracture (Eds: G. S. Wass and S. Bruemmer) (1989). Materials Science Forum 46, 237.
[54] Hirth, J.P., and Lothe, J., Theory of Dislocations, Mcgraw-Hill, New York (1968).
[55] Pestman, B.J., De Hosson, J.T.M., Vitek, V., Schapink, F., Scripta Metall. 23, 1431 (1989).
[56] Read, W.T., Shockley, W, Phys. Rev., 78,275 (1950).
[57] Vitek, V., Scripta metal. 21,711 (1987).
[58] a. Willis, J.R., Jain, S.C., Bullough, R., Philos. Mag. A 62, 115 (1990).
b. Willis, J.R., Jain,S.C., Bullough, R, Philos. Mag. A 64, 629 (1991).
c. Gosling, T.J., Willis, J.R., Bullough, R., Jain, S.C., J. Appl.Phys.73, 8297 (1993).
[59] Kooi, B.J., De Hosson, J.T.M., Acta materialia 48, 3687 (2000).
[60] Barnett, D. and Lothe, J., J.Phys. F4,1618(1974).
[61] Shen, Z., Wagoner, R.H., and Clark, W.A.T., Acta Metall. et Mat., 36, 3231 (1988).
[62] Lee, T.C., Robertson, I.M., and Birnbaum, H.K., Metall. Trans. A, 21, 2437 (1990).

[63] Bamford, T.A., Hardiman, B., Shen, Z., Clark, W.A.T., and Wagoner, R.H., Scripta Metall. et Mat., 20, 253 (1986).

[64] a. Pestman, B.J., De Hosson, J.T.M., Vitek, V., Schapink, F.W., Philos. Mag. A64, 951-969 (1991).

b. De Hosson, J.T.M., Pestman, B.J., Materials Science and Engineering, A 164, 1993, 415-420.

c. Pestman, B.J., De Hosson, J.T.M., Acta Metall. et Materialia 40, 10, 2511-2521 (1992).

d. F. Tichelaar, Thesis,University of Technology, Dellft, 1990.

[65] Conrad, H., Jung, K., Mat. Sci. Engng., A391, 272 (2005).

[66] Carsley, J.E., Ning, J., Milligan, W.W., Hackney, S.A., Aifantis, E.C., Nanostructured Matls, 5, 441 (1995).

[67] Ashby, M.F., Philosoph. Mag., 22, 399 (1970).

[68] Meyers, M.A., Chawla, K.K., Mechanical Metallurgy, Prectice-Hall, New York (1984).

[69] Lax, M., Phys. Rev.,85, 621 (1952).

[70] a. Pethica, J.B., Hutchings, R., Oliver, W.C., Phil. Mag. A 48, 593 (1983).

b.Stone, D., LaFontaine, W.R., Alexopoulos, P., Wu, T.-W., Li, C.Y., J. Mater. Res. 3, 141 (1988).

c. JField, S., Swain, M.V., J. Mater. Res. 8, 297 (1993).

[71] a. Carvalhio, N.J.M., PhD thesis, University of Groningen, 2001.

b. Carvalho N.J.M. and De Hosson, J.T.M., Thin Solid Films 388, 150 - 159 (2001).

c. Carvalho, N.J.M., De Hosson, J.T.M., J. Mat. Res. 16, 2213 - 2222 (2001).

[72] Gerberich,W.W., Kramer, D.E., Tymiak, N.I. Acta Mater. 47, 4115 (1999).

[73] Oliver, W.C., Pharr, G.M., J. Mater. Res. 7, 1564 (1992).

[74] J.-L. Loubet, B.N. Lucas, W.C. Oliver, Mat. Res. Soc. Symp. Proc. 436, 233 (1996).

[75] M.J. Mayo, W.D. Nix, Acta Metall. 35, 2183 (1988).

[76] N.A. Stillwell, D. Tabor, Proc. Phys. Soc. London 78, 169 (1961).

[77] J.-L. Loubet, J.M. Georges, O. Marchesini, G. Meille, J. Tribology 106, 43 (1984).

[78] M.F. Doerner, W.D. Nix, J. Mater. Res. 1, 601 (1986).

[79] G.M. Pharr, W.C. Oliver, F.R. Brotzen, J. Mater. Res. 7, 613 (1992).

[80] J. Boussinesq, Applications des Potentiels a l'étude de équilibre et du mouvement des solides élastiques, Gauthier-Villars, Paris, (1885).

[81] H. Hertz, J. Reine und angewandte Mathematik 92, 156 (1882).

[82] a. A.E.H. Love, Philos. Trans. A 228, 377 (1929).

b. A.E.H. Love, Quart. J. Math. 10, 161 (1939).

[83] J.W. Harding, I.N. Sneddon, Proc. Cambridge Philos. Soc. 41, 16 (1945).

[84] Stillwell, N.A., Tabor, D., Proc. Phys. Soc. London, 78, 169 (1961).
[85] S.I. Bulychev, V.P. Alekhin, M.Kh. Shorshorov, A.P. Ternovskii, G.D. Shnyrev, Zavod. Lab. 41, 1137 (1975).
[86] I.N. Sneddon, Int. J. Engng. Sci. 3, 47 (1965).
[87] R.B. King, Int. J. Solids Structures 23, 1657 (1987).
[88] A. Bolshakov, W.C. Oliver, G.M. Pharr, J. Mater. Res. 11, 760 (1996).
[89] A. Bolshakov, W.C. Oliver, G.M. Pharr, Mat. Res. Soc. Symp. Proc. 436, 141 (1997).
[90] A. Bolshakov, G.M. Pharr, J. Mater. Res. 13, 1049 (1998).
[91] J.C. Hay, A. Bolshakov, G.M. Pharr, J. Mater. Res. 14, 2296 (1999).
[92] Larsson, P.-L., Giannakopoulos, A.E., Soderlund, E., Rowcliffe, D.J., Vestergaard, R. Int. J. Solids Struct. 33, 221(1996).
[93] Eshelby, J.D., Frank, F.C., Nabarro, F.R.N., Philos. Mag. 42, 351 (1951)
[94] F.R.N. Nabarro, Z.S. Basinski, D.B. Holt, Advances in Physics, 13,193(1964).
[95] Gouldstone, A., Koh, H.-J., Zeng, K.J., Giannakopoulos, Suresh, S., Acta Materialia 48,2277(2000).